U.PORTO
FEUP FACULDADE DE ENGENHARIA
UNIVERSIDADE DO PORTO

U.PORTO
ICBAS | INSTITUTO DE CIÊNCIAS BIOMÉDICAS ABEL SALAZAR
SCHOOL OF MEDICINE AND BIOMEDICAL SCIENCES

DISSERTATION DEVELOPED IN THE AMBIT OF THE INTEGRATED MASTER IN BIOENGINEERING
SPECIALIZATION IN MOLECULAR BIOTECHNOLOGY

HYALURONIC ACID-COATED LIPID NANOPARTICLES FOR ENHANCED DELIVERY OF MITOXANTRONE TO CANCER CELLS

Maria Francisca Milheiro Bento

Supervisor: Prof. Dr. Salette Reis
Co-supervisor: MSc Andreia Granja

15 September 2021

- This page was intentionally left in blank -

ABSTRACT

Breast cancer is ranked as the number one most diagnosed cancer for both sexes combined in 2020 by the International Agency for Research on Cancer. Owing to the complexity and heterogeneity of breast cancer pathophysiology, current treatments face the challenge of improving the eradication of malignant breast cells while overcoming their non-specificity that ultimately leads to major side effects.

This study aims to develop novel hyaluronic acid (HA)-functionalized solid lipid nanoparticles (SLN) for efficient site-specific delivery of the antineoplastic agent mitoxantrone (MX). A low molecular weight HA (HA 20-60 kDa) and a high molecular weight HA (HA 1000-1800 kDa) were selected to study the most promising ligand for the CD44 receptor overexpressed in breast cancer cells.

MX-loaded lipid nanoparticles were produced to increase the tumor delivery of MX by a simple, economical and easily to scale method. Furthermore, comparative studies between SLNs functionalized with HA by electrostatic interaction versus covalent binding were carried out. The SLN coated with 1,2-Dipalmitoyl-sn-glycero-3-phosphoethanolamine-HA conjugate (DPPE-HA) were selected on the grounds of their physicochemical properties and non hemolytic effects, making them ideal for intravenous administration.

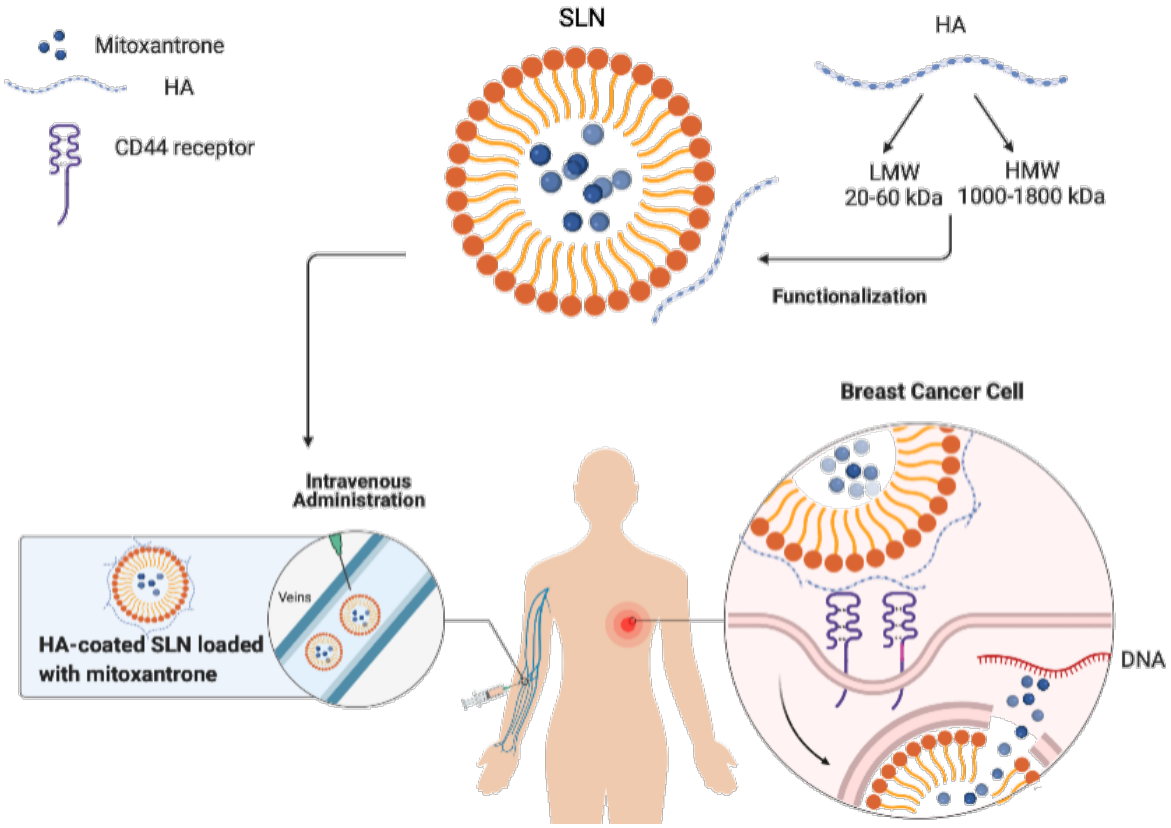
The HA functionalized SLNs loaded with MX presented a size lower than 220 nm, suitable for intravenous (IV) administration route and tumor accumulation and encapsulation efficiency (EE) higher than 88% and, overall, the SLN produced exhibited good colloidal stability, without substantial alterations of either their size, zeta potential and EE properties up to 4 weeks of storage under refrigeration (4 °C). The *in vitro* MX release studies revealed that HA-functionalized NPs had a sustained drug release mechanism in physiological medium and a significant accelerated drug release at endosomal environment, which promises a desired delayed MX release upon its injection into the bloodstream and a greater release at the intratumoral and cancer intracellular level.

Cytotoxicity assays in RBC revealed that SLN did not present hemolytic activity and were cytocompatible for MCF-7 human breast cancer cell line, up to concentrations of 500 µg/mL of lipid. The anti-cancer efficiency of the MX loaded nanoformulations were further tested in MCF-7 CD44+ cell line. A significant decrease in cell viability was observed after treatment with 1 µg/mL of drug for each MX-loaded nanoformulation, with SLN functionalized with the high molecular weight HA showing increased MX-induced cancer cell toxicity, which suggests an increase in the uptake of MX by these cancer cells. Further assessment of nanoparticles uptake by MCF-7 cells using confocal microscopy and flow cytometry techniques showed a successful enhanced internalization by HA functionalization, an effect that was significantly higher for HA 1000-1800 kDa coated SLN.

Conclusively, the resulting data evidenced that HA-functionalized loaded NPs might exhibit promising therapeutic potential for management of breast cancer disease, while further supporting the use of higher molecular weight HA for a more effective tumor accumulation.

- This page was intentionally left in blank -

GRAPHICAL ABSTRACT



Keywords: Mitoxantrone; Breast Cancer; Nanotechnology; Solid Lipid Nanoparticles (SLN); Active Targeting; Hyaluronic Acid Functionalization

- This page was intentionally left in blank -

AGRADECIMENTOS

Escrever esta tese não seria possível sem o apoio de algumas pessoas que à sua maneira contribuíram para a realização desta última etapa do meu percurso académico e que farei o meu melhor para mencionar.

Quero agradecer à minha supervisora Professora Doutora Salette Reis pela oportunidade e orientação neste projeto desafiante e de tanto valor. Acima de tudo, agradeço a motivação e positividade com que encarou o nosso projeto do início até ao fim.

À minha co-orientadora Andreia Granja, que foi o meu braço direito e a minha perna esquerda também. A tua serenidade e excelência na superação dos obstáculos encontrados ao longo do percurso foram essenciais e são um exemplo a seguir. Estou extremamente grata por te ter tido como minha mentora e pela tua entrega a este meu projeto.

Não posso deixar de mencionar as pessoas do grupo MB2, das salas 19 e 20 do E3 (FFUP), que proporcionam um ambiente de partilha, simpatia e encorajamento que tornaram tão aprazível o período de estágio. Um especial agradecimento à Professora Cláudia, à Tânia Moniz, Ana Isabel e Andreia Marinho pelo tempo que dedicaram a orientar-me no laboratório e nas minhas experiências. Acabo este projeto no laboratório a sorrir.

Quero também agradecer o apoio técnico da Unidade de Microscopia de Alta Resolução (CEMUP, UP) e do Laboratório de Espectrometria de Ressonância Magnética Nuclear.

À minha família que me apoiou e torceu por mim, e sobretudo aos meus pais que proporcionaram as ferramentas necessárias para cumprir esta meta. Mãe, por puxares por mim para dar o meu máximo sempre, e pai por me compreenderes tão bem.

Aos meus amigos/as que estiveram presentes nas aventuras e desventuras e que viveram comigo a montanha-russa de emoções que é a realização de uma tese e todo um percurso académico: Às minhas amigas de anos, que me conhecem como a palma da mão e de quem trago comigo uma boa dose de sabedoria e de momentos de puros risos. Às pessoas especiais que conheci na faculdade, que não só me ajudaram a atingir este objetivo, mas também me acarinharam (e tanto me ouviram). Quero agradecer especialmente à Tânia, Palma, Cate, Catarina e Maia, fico contente por termos cruzado caminhos e levo da UTAD, FEUP e ICBAS um pouco de cada um de vocês para a vida. Tânia, sem ti e as tuas (-nossas) casas não era a mesma coisa e eu não pedia melhor. Um especial obrigada à minha amiga-prima Pipa, a minha parceira de Bioengenharia, pelas partilhas bonitas nestes últimos anos e pela tua presença nos momentos de maior apuro.

Zé, pelo apoio desmedidamente grande que recebi ao longo destes 9 meses. São insubstituíveis a força e a beleza que trouxeste a este percurso. Se há coisa que aprendi contigo é que para conseguir basta acreditar (e começar) e que melhores resultados acontecem quando dançamos ao som das adversidades. Também quero agradecer à sua família que ao longo deste período me acolheu de portas e braços abertos.

Assim concluo 5 anos, formada em Bioengenharia e com um enorme orgulho nas múltiplas aprendizagens, ferramentas e lembranças que levo de todos vocês.

- This page was intentionally left in blank -

TABLE OF CONTENTS

ABSTRACT I
GRAPHICAL ABSTRACT III
ACKNOWLEDGMENTS V
CHAPTER 1 INTRODUCTION 1
1.1. Breast Cancer 1
1.2. Mitoxantrone 5
1.3. Nanotechnology and cancer 8
1.4. Lipid Nanoparticles 13
1.5. Targeted delivery of nanoparticles to cancer cells 20
1.6. Aim and objectives 25
CHAPTER 2 MATERIALS AND METHODS 26
2.1. Materials 26
2.2. Production of Solid Lipid Nanoparticles 26
2.3. Synthesis of 1,2-Dipalmitoyl-sn-glycero-3-phosphoethanolamine-hyaluronic acid conjugate 27
2.4. Nuclear magnetic resonance analysis 28
2.5. Synthesis of Functionalized Solid Lipid Nanoparticles 29
2.6. Hyaluronic acid quantification assay 29
2.7. Characterization of Solid lipid nanoparticles 30
2.8. Cellular studies 34
2.9. Statistical analysis 39
CHAPTER 3 RESULTS AND DISCUSSION 39
3.1. 1H NMR characterization 39
3.2. Nanoparticle functionalization with Hyaluronic acid: electrostatic interaction versus conjugate 41
3.3 Production of mitoxantrone-loaded solid lipid nanoparticles 46
3.4 Cellular studies 51
CHAPTER 4 CONCLUSION AND FUTURE PROSPECTS 58
REFERENCES 60

LIST OF FIGURES

FIGURE 1 BREAST TISSUE AND IN SITU, INVASIVE AND METASTATIC CARCINOMA REPRESENTATION 2

FIGURE 2 MITOXANTRONE CHEMICAL STRUCTURE 6

FIGURE 3 SCHEMATIC REPRESENTATION OF THE DIFFERENT TYPES OF SLN AND NLC AND DRUG LOCATION WITHIN THE LIPID MATRIX 15

FIGURE 4 STRUCTURE OF CD44 PROTEIN 22

FIGURE 5 STRUCTURAL FORMULA OF HYALURONAN 23

FIGURE 6 RELEASE ASSAY PROCEDURE SCHEME 34

FIGURE 7 THE UNDERLYING WORKING PRINCIPLE OF A FLOW CYTOMETER 38

FIGURE 8 NMR ANALYSIS OF DPPE-HA CONJUGATE 40

FIGURE 9 EFFECT OF STORAGE TIME ON SIZE AND PDI OF THE SLN FORMULATIONS. 43

FIGURE 10 EFFECT OF TIME OF STORAGE ON ZETA POTENTIAL OF SLN NANOFORMULATIONS FUNCTIONALIZED BY ELECTROSTATIC INTERACTION (CTAB HA) AND WITH DPPE-HA CONJUGATE (DPPE-HA) 43

FIGURE 11 96-WELLS PLATE PICTURE AFTER HEMOLYSIS ASSAY 44

FIGURE 12 IN VITRO HEMOLYSIS ASSAY RESULTS FOR DILUTED HUMAN BLOOD EXPOSED TO DIFFERENT CONCENTRATIONS (3, 6 12, 24 MG/ML) OF FUNCTIONALIZED SLN-CTAB AND SLN DPPE-HA 45

FIGURE 13 CALIBRATION CURVE OF HA 1000-1800 IN PBS PH 8.2. 46

FIGURE 14 NTA ANALYSIS OF SLN DPPE-HA 20-60 48

FIGURE 15 EFFECT OF TIME STORAGE ON SIZE (A), PDI (B), ZETA POTENTIAL (C) AND EE (D) OF SLN DPPE-HA NANOFORMULATIONS UNLOADED (DPPE-HA) AND MX-LOADED (MX DPPE-HA) 50

FIGURE 16 IN VITRO MX RELEASE PROFILE FROM DRUG-LOADED SLN FUNCTIONALIZED EITHER WITH HA 20-60 AND HA 1000-1800 IN SIMULATED PHYSIOLOGIC (PH=7.4) AND ENDOSOMAL (PH=5) FLUIDS 51

Figure 17 In vitro hemolysis assay results for diluted human blood exposed to different concentrations (3, 6 12, 24 mg/mL) of MX-loaded SLN DPPE-HA formulations 52

Figure 18 96-wells plate picture after hemolysis assay 52

Figure 19 MCF-7 cell viability assessed by Resazurin assay after 24 hours of exposure to the different nanoformulations at increasing concentrations of SLN 54

Figure 20 MCF-7 cell viability assessed by Resazurin assay after 24 hours of exposure to the different nanoformulations at increasing concentrations of MX (or the equivalent solid amount of lipid in unloaded SLN) 54

Figure 21 Dose-response curves of MCF-7 cells incubation with free mitoxantrone and the different nanoformulations 55

Figure 22 Confocal microscopy images of MCF-7 exposed to different MX loaded nanoparticles (SLN, SLN HA 20-60, SLN HA 1000-1800) for 4h and 24h 56

Figure 23 Cellular uptake for C6-loaded SLN in MCF-7 cells, after 1h, 4h and 24h of incubation. 57

LIST OF TABLES

TABLE 1 EXAMPLES OF FDA-APPROVED NANOPARTICULATE FORMULATIONS 10

TABLE 2 PHYSICOCHEMICAL CHARACTERIZATION OF THE HA FUNCTIONALIZED SLN FORMULATIONS BY DLS: SIZE, PDI, ZETA POTENTIAL 42

TABLE 3 PHYSICOCHEMICAL CHARACTERIZATION OF THE SLN FORMULATIONS FUNCTIONALIZED WITH THE CONJUGATE, UNLOADED (DPPE-HA 20-60 AND DPPE-HA 1000-1800) AND LOADED WITH MX (MX DPPE-HA 20-60 AND DPPE-HA 1000-1800): SIZE, PDI, ZETA POTENTIAL, EE AND LC. 47

TABLE 4 MEAN SIZE AND SIZE DISTRIBUTION OF HA 20-60 AND HA 1000-1800 FUNCTIONALIZED SLN (DPPE-HA 20-60 AND DPPE-HA 1000-1800, RESPECTIVELY) FROM DLS AND NTS MEASUREMENTS. MEAN SIZE (MEAN); POLYDISPERSITY INDEX (PDI); STANDARD DEVIATION (SD) CALCULATED BY THE NTA SOFTWARE; CONCENTRATION IN HUNDRED MILLION (E8) PARTICLES/ML AS MEASURED BY NTA. 47

TABLE 5 EE AND LC MEASUREMENTS OF THE MX-LOADED NANOFORMULATIONS 49

LIST OF EQUATIONS

EQUATION 1 30
EQUATION 2 31
EQUATION 3 33
EQUATION 4 33
EQUATION 5 35
EQUATION 6 36

- This page was intentionally left in blank -

ABBREVIATIONS

C6	Coumarin 6 dye
CEMUP	Centro de Materiais da Universidade do Porto
CreEL	Cremophor EL
CTAB	Cetyltrimethylammonium bromide
CTM	Cetyltrimethylammonium bromide turbidimetric method
D2O	Deuterium oxide
DCIS	Ductal carcinoma in situ
DLS	Dynamic light scattering
DM	Dialysis membrane
DMEM	Dulbecco's Modified Eagle Medium
DMSO	Dimethyl sulfoxide
DNA	Deoxy-ribonucleic acid
DPPE	1,2-Dipalmitoyl-sn-glycero-3-phosphoethanolamine
DTX	Docetaxel
ECM	Extracellular matrix
EDC	Ethyldimethylaminopropyl-carbodiimide
EE	Encapsulation efficiency
ELS	Electrophoretic light scattering
EPR	Enhanced permeability and retention
ERBB2	Epidermal growth factor 2
ERα	Estrogen receptor alpha
FA	Folic acid
FBS	Fetal Bovine Serum
FDA	Food and Drug Administration
GAG	Glycosaminoglycan
gp60	60-kDa glycoprotein
GRAS	Generally-recognized-as-safe
HA	Hyaluronic acid/Hyaluronan
HA 1000-1800	HA 1000-1800 kDa
HA 20-60	HA 20-60 kDa
HCl	Hydrochloric acid
HMW	High molecular weight
HPH	High-pressure homogenization
LC	Loading capacity
LDC	Lipid drug conjugate
LMW	Low molecular weight

LN	Lipid nanoparticles
MAPK	Mitogen-activated protein kinases
MCF-7	Michigan Cancer Foundation-7
MWCO	Molecular weight cut off
MX	Mitoxantrone
nab	Nanoparticles albumin-bound
NFκB	Nuclear factor-kappa B
NHS	N-hydroxysuccinimide
NLC	Nanostructured lipid carrier
NMR	Nuclear magnetic resonance
NP	Nanoparticle
NTA	Nanoparticle tracking analysis
PDI	Polydispersity Index
PEG	Polyethylene glycol
PI3K	Phosphoinositide 3-kinase
PLN	Polymer-lipid hybrid nanoparticle
PR	Progesterone receptor
PTX	Paclitaxel
RBC	Red blood cell
RES	Reticuloendothelial system
SLN	Solid lipid nanoparticle
US	United States

Chapter 1 Introduction

1.1. Breast Cancer

Breast cancer is the uncontrolled division and growth of abnormal cells from the breast tissue. This occurs when the genes that control cell growth acquire mutations. DNA changes or mutations can be inherited or passed on from parents, however most DNA mutations linked to breast cancer are acquired [1].

According to GLOBOCAN 2020 cancer statistics, in 2020, there were 2.3 million women diagnosed with breast cancer and 685 000 deaths globally. For both sexes combined female breast cancer is the most commonly diagnosed cancer (11.7% of total cases) worldwide and, among females, is the first leading cause of cancer death (15.5% of total cases), followed by lung cancer (13.7%) [2]. Moreover, there are more lost disability-adjusted life years (DALYs) women to breast cancer globally than by any other type of cancer [3].

Breast cancer incidence rates peaked during the 1980s and 1990s in many countries in Northern America, Oceania, and Europe, during the early 2000s, this incidence dropped or stabilized due to improvements in survival. This progress reflects earlier detection combined with increased awareness of symptoms and advances in therapeutics [2]. However, since 2007, there has been a slow rise in incidence rates in the United States (US) of <0.5% per year, and there have also been moderate but significant increases in many other countries in Europe and Oceania. Studies attributed the cause of this rise to the obesity epidemic impact on certain types of cancers and the impact of mammography screening, which preferentially detects slow-growing cancers [2].

Across the Europe, the health-care costs of cancer were equivalent to €102 per citizen in 2009. Breast cancer had the highest economic cost of €15.0 billion, after lung cancer, which accounts for 12% of overall cancer costs. [4] Furthermore, in 2011 medical expenditures in the US were projected to reach $16.5 billion, in 2020, being higher that rectal cancer ($14 billion), lymphoma ($12 billion), lung cancer ($12 billion) and prostate cancer ($12 billion), according to the National Cancer Institute [5].

1.1.1. Breast Cancer Classification

The breast is mainly composed of fat, connective tissue and glandular tissue that, itself, is divided into lobules. A network of ducts (milk ducts) branches from the lobes towards the nipples (Figure 1) [1]. Breast cancer most commonly develops from the glandular tissue of the breast, mainly from the epithelial cells lining the milk ducts [1].

Breast cancer is a highly heterogeneous disease, having fairly complex classifications depending on numerous factors [6]. Breast cancer can be classified based on the stage of the tumor.

Initially, the tumor growth is confined to the duct or lobule, being classified as *in situ* cancer (stage 1), status at which generally causes no symptoms [1, 3]. Over time, the *in situ* cancer may progress and invade the surrounding breast tissue becoming an invasive breast cancer, which may eventually invade the nearby lymph nodes and start a regional metastasis (stage 2–3). When cancer cells migrate from where they were first formed (primary cancer) and spread to other parts of the body (secondary cancer), a distant metastasis is formed (stage 4). Lung, bone, liver and brain are the most frequent sites of breast cancer metastasis [6]. The cause of death from breast cancer in women is primarily due to widespread metastasis [3]. Approximately 62% of breast cancers in the US are confined to the breast at diagnosis, while an additional 31% have spread to regional lymph nodes. Only 6% of breast cancers are metastatic at the time of diagnosis [7].

Nowadays, breast cancer is often classified based on histopathological type. The most common breast cancer histology is invasive ductal carcinoma [7]. The second most common type of breast cancer, comprising almost 15% of breast cancers, is invasive lobular carcinoma, meaning that the cancer started in the lobules and spread into the surrounding breast tissue. There are other less common types of breast cancer such as ductal carcinoma in situ (DCIS), which is noninvasive and is considered the earliest form of breast cancer and inflammatory breast cancer, a rare type that often occurs in younger patients [6-9].

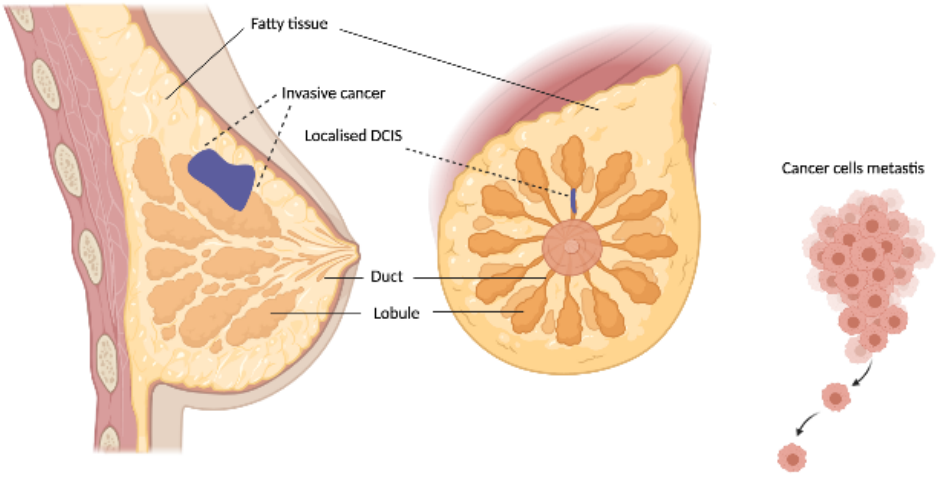


Figure 1 Breast tissue and *in situ*, invasive and metastatic carcinoma representation

In addition, breast cancer is also categorized into 3 major subtypes based on the presence or absence of molecular markers identified in breast cancer pathogenesis [7]. One of the main molecular targets is the estrogen receptor alpha (ERα), a steroid hormone receptor and a transcription factor that is expressed in approximately 70% of invasive breast cancers [7]. When activated by estrogen, ERα activates oncogenic growth pathways in breast cancer cells. Another molecular marker is the closely related steroid hormone progesterone receptor (PR) that is also involved in the ERα signaling. The use of endocrine agents to downregulate ER signaling is the primary systemic therapy for ER-positive or PR-positive breast cancers. The second main molecular target is epidermal growth factor

2 (ERBB2, formerly HER2), a transmembrane receptor tyrosine kinase in the epidermal growth factor receptor family that is amplified or overexpressed in approximately 20% of breast cancers [7]. Tumors with amplification of the gene ERBB2 are ERBB2+ and are associated with poor prognosis in the absence of systemic therapy. Triple negative breast cancer, which accounts for 15% of all types of breast cancer, is featured by cells that do not express hormone receptors (estrogen and progesterone) and ERBB2. Triple-negative breast cancer differs from other types of invasive breast cancer as they grow and spread faster, have limited treatment options, and a worse prognosis [10].

Based on the molecular subtype of the disease, the therapeutic may comprise hormone treatments and/or targeted therapies.

1.1.2. Standard Treatments

Currently, patients diagnosed with breast cancer are often given multimodality treatment that involves standard modalities such as surgery, radiation therapy and drug therapy [7]. Many different factors are considered when deciding which combination of treatments is the most adequate for the patient, including the location of the tumor in the breast, the stage of the tumor, and molecular subtype of the disease, among other factors [11].

For nonmetastatic breast cancer, the main approach is the local intervention by means of surgical resection of the mammary tissue or removal of the axillary lymph nodes, with consideration of post-operative radiation. The first modality is used mainly for eradicating the primary tumor and locoregional cancerous tissues [7]. Radiotherapy uses high energy x-rays to kill cancer cells and is often done after entire breast surgery, to lower the risk of cancer recurrence. Their value tends to decline as the cancer progresses and metastasizes.

Breast cancer drug therapy is used to reduce the tumor burden and prevent, control or treat cancer metastasis and, in the case of advanced metastatic breast cancer, with the goal of prolonging life and palliation of symptoms. Systemic therapy can be given as preoperative (neoadjuvant), postoperative (adjuvant), or both. Neoadjuvant therapy aims to reduce the size of the tumor and adjuvant therapy is usually advised to lower the chances of cancer recurrence [7].

Drug therapy often consists of hormonal therapy, which uses hormones or hormone-like drugs to suppress cancer cell proliferation, and chemotherapy, which mainly relies on the use of cytotoxic compounds. Targeted cancer drugs or bone strengthening drugs (bisphosphonates) are other treatment options [6]. In recent years, the latest breakthroughs in molecular biology and immunotherapy have provided the rise of targeted therapies tailored to the specific pathophysiology of different subtypes of breast cancer. This approach generally involves a small molecule drug or monoclonal antibody targeting a specific molecular pathway. The most commonly used targeted therapy so far is trastuzumab (ie, Herceptin), a humanized anti-ERBB2 monoclonal antibody [6].

Breast cancer molecular subtype guides the standard systemic therapy administered. The use of endocrine agents to downregulate ER signaling is the primary systemic therapy for ER-positive or PR-positive breast cancers [7]. Endocrine therapies include tamoxifen, a selective estrogen-receptor

modulator, aromatase inhibitors or ovarian suppression. These medicines are able to reduce the chance of recurrence of hormone-positive cancers by nearly half [12]. Cancers that do not express ER or PR are hormone receptor negative are treated with chemotherapy. The HER-2 positive cancers are amenable to treatment with biological agents that specifically target the HER-2 protein, such as trastuzumab and the antibody pertuzumab [13]. Other targeted therapeutics currently used are small-molecule tyrosine kinase inhibitors, like lapatinib and neratinib, which are effective second-line anti-HER2 adjuvant treatments for advanced breast cancer or in case of recurrence [14]. To improve the efficacy of the treatment and survival, these targeted biological agents are often combined with chemotherapy.

Chemotherapy is given to all HER-2 positive cancers in combination with endocrine therapy if the tumor is simultaneous ER and PR positive. Chemotherapy is generally administered to all patients with triple-negative breast tumors larger than 5 mm. In fact, chemotherapeutic agents are the only therapeutics approved by the Food and Drug Administration (FDA) for treating nonmetastatic triple-negative disease [7]. Hormone treatment and the targeted cancer drug trastuzumab are not effective for people with triple negative breast cancer.

Currently, chemotherapy is the main treatment for most cancers in advanced stage [7] . The chemotherapeutic drugs circulate throughout the body in the bloodstream and act by disrupting the growth of cancer cells. Anthracyclines and taxanes, such as the adriamycin (Doxorubicin) and taxol (Paclitaxel), respectively, are two of the most common class of drugs used in breast cancer chemotherapy regimens [15, 16]. Meta-analysis of approximately 100 000 women enrolled in randomized trials of chemotherapy for early breast cancer demonstrated that a high-dose anthracycline-containing chemotherapy regimen, compared with no chemotherapy, significantly reduced 10-year breast cancer mortality by approximately one-third [17]. Although most of the anthracyclines possess significant anticancer activities as single agents, they are now used in combination chemotherapy to improve therapeutics efficacy and to reduce toxicities. Paclitaxel (PTX) is a chemotherapeutic agent from the group of taxanes used as first-line treatment, effective for the treatment of several cancers including breast cancer [18]. Chemotherapy regimens containing both anthracycline and taxane achieve the greatest risk reduction and remain the appropriate choice in high-risk patients [7, 16].

Despite being widely used, adjuvant therapies like chemotherapy have major limitations due to nonspecific drug distribution, multidrug resistance and the heterogeneity of cancer [16, 19]. The lack of cancer cell-specificity strongly compromises the therapeutic efficacy of the drugs because only a small part of the drug can reach the tumor region, which reduces its efficacy and causes several adverse side-effects due to systemic toxicity. Furthermore, drugs are also toxic to healthy cells. General side-effects attributed to adjuvant chemotherapy include asthenia, nausea and vomiting, mucositis, myelosuppression and increased risk of getting an infection, weight modifications, alopecia, ovarian failure, muscle pain and overall decrease in the quality of life of the patient [7, 20].

In addition, other complications potentially lethal associated with both chemo and hormonal therapy have also been reported. Tamoxifen can increase the risk of endometrial cancer and promote ischemic cerebrovascular events and venous thromboembolic events [10]. Doxorubicin can damage of the myocardium inducing cardiotoxicity which can led to cardiomyopathy [21]. In turn, PTX formulations have resulted in neuropathic pain, nephrotoxicity and neurotoxicity which was caused both by the drug and the excipient materials [16, 21]. Although most chemotherapy side effects are usually temporary and disappear once the treatment is over, for some patients, chemotherapy can cause long term effects. Late side effects can include early menopause, infertility, peripheral neuropathy and heart complications [22].

Despite the associated short- and long-term risks, chemotherapy remains to be an essential treatment for triple-negative breast cancer and an important adjuvant to endocrine therapy or ERBB2-directed therapy treatment and for preventing recurrence in many patients with stage I-III breast cancer [7]. Therefore, it is essential to explore and develop novel strategies to minimize the undesirable effects of chemotherapy and increase its anti-cancer efficacy.

1.2. Mitoxantrone

1.2.1. Source and chemical properties

Mitoxantrone (Novantrone®; dihydroxyanthracenedione) is a synthetic anthraquinone derivative widely used as an intravenously administered chemotherapeutic drug. It belongs to the class of DNA intercalating antineoplastic agents anthracenediones, a family of drugs called anticancer antibiotics [23, 24].

Mitoxantrone (MX) was the outcome of a program in synthetic chemistry, at the Medical Research Division of the American Cyanamid Company. It was originally conceived as a simplified analog of the anthraquinone compound, a molecule with structural features predicted to favor intercalation with double stranded DNA, thus interfering with its synthesis. It proved to be the most effective and potent antitumoral derivative synthesized [23, 25].

The structure of MX (Figure 2) is viewed as an anthracycline analog, a class of potent and widely used DNA intercalating cytotoxic drugs. As such, the symmetrical structure of MX comprises a tricyclic planar chromophore and two basic side chains. Molecules with such structure had been

shown to possess a wide range of pharmacological effects encompassing antiviral, antibacterial, antiprotozoal, anticancer, and immunomodulating activities [26, 27].

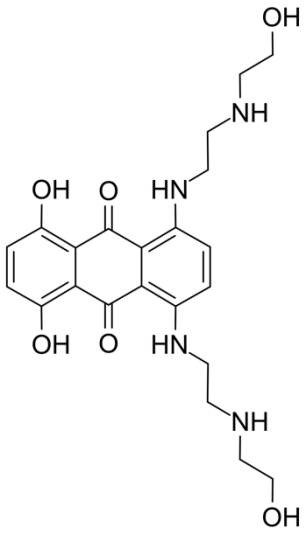


Figure 2 Mitoxantrone chemical structure

Studies have found that MX accumulates in cells and concentrates in the nucleus, where it interacts with nucleic acids. Still, the mechanism of antitumor activity of MX is not completely defined [26]. Several mechanisms are thought to be responsible for the antitumor activity of MX. These include aggregation and compaction of DNA via electrostatic cross-linking, stabilization of the nuclear topoisomerase II-DNA intermediate complex, free radical generation, inhibition of microtubule assembly and inhibition of protein kinase C activity [28]. Although not entirely clear, the mechanism by which MX binds to DNA is thought to be related to the positively charged N-containing side chains that project outwardly from the molecule and possibly stabilize the ring between base pairs, by intercalating with the negatively charged phosphate backbone DNA. The binding of MX to DNA consequently causes DNA condensation and inhibition of DNA replication and RNA transcription [26]. Cells in culture treated with MX have shown nuclear morphologic changes of chromosomal scattering and micronuclei formation [29]. *In vitro* studies with mouse L1210 leukemia cells shown increased DNA-protein crosslinks and protein-concealed DNA breaks, similar to the effects seen with doxorubicin [23].

It is also known that MX recognizes the chromatin structure with greater affinity than free deoxy-ribonucleic acid (DNA) [26]. Moreover, compared with the doxorubicin, MX is six to seven times more potent in inhibiting 3H-thymidine incorporation into DNA and 3H-uridine incorporation into RNA.

As an anthracycline agent, MX displays a natural fluorescence which enables *in vitro* and *in vivo* studies with MX, by fluorescence-based techniques such as confocal microscopy and flow cytometry [30, 31]. Studies of MX mechanism of action or cellular distribution have been conducted by taking advantage of MX fluorescence. MX has been found to fluoresce with excitation maxima at 610 and 660 nm and emission maximum at 685 nm. The fluorescence intensity of MX is affected by the pH and the emission spectrum is red-shifted by DNA [31, 32].

As a chemotherapeutic drug, MX has shown significant clinical effectiveness in the treatment of advanced breast and prostate solid cancers, as well as lymphoma and acute leukemia [33-37]. MX also acts as an immunosuppressant for the treatment of multiple sclerosis [28].

Upon the discovery of MX, at phase I and subsequent phase II clinical trials, MX has shown to be effective, alone and in combination with other drugs, in the treatment of breast carcinoma, acute nonlymphocytic leukemia, and lymphoma, with reduced toxicity compared to doxorubicin [23]. MX has shown excellent activity against a broad spectrum of animal tumors, in addition it induces a significant number of putative cures, or long-term survivors [38, 39]. The results of many laboratory studies indicate that the drug is effective against non-proliferating as well as proliferating cells. A comparison of the activity of MX and doxorubicin on cycling and noncycling human colon carcinoma cells was made and MX showed to be about ten times as potent in this system [23]. Preclinical studies in several animal models indicate that MX does not have the cumulative cardiotoxic liability associated with the much-used anthracycline [23]. Furthermore, studies in mice tumors have shown synergism between MX and other marketed chemotherapeutic drugs such as cytarabine, fluorouracil, vincristine, cisplatin, methotrexate and cyclophosphamide. Studies conducted in rats bearing prostate cancer tumors that were treated with MX showed a significant reduction in tumor growth compared to the control [28]. Furthermore, MX has been shown to enhance cytotoxicity induced by both radiation and hyperthermia in experimental tumor systems, suggesting the potential for a combined-modality approach in clinical trials [29]. Resistance to the antitumor activity of MX has been seen both *in vitro* and *in vivo* by many different mechanisms [28].

On the basis of this potency and activity, MX was rapidly progressed to clinical evaluation. Furthermore, the lower doses of MX required in comparison with other members of that series should lessen the potential for undesirable side-effect in the clinic [23]. At the moment, a number of clinical trials are in progress investigating MX as a candidate for the treatment of different cancers [28]. MX has undergone development for the treatment of liver cancer, early-stage prostate cancer, breast, lung and ovarian cancers and non-Hodgkin's lymphoma in the US [28].

In clinic, a combination regime therapy of cyclophosphamide, etoposide and MX was compared to standard cyclophosphamide, doxorubicin and fluorouracil therapy in 154 patients with primary breast cancer. The former treatment resulted in significant reductions in the number of patients who had died (17% vs 35%) or relapsed at 5 years (25% vs 66%), and significantly longer elapse-free (≥ 400 vs 190 weeks) and overall survival durations (≥ 400 vs 320 weeks) [28].

1.2.3. Mitoxantrone in the market

MX has been developed as an infusion or an injection formulation for intravenous administration. It has been launched as Novantrone® for the treatment of advanced breast cancer in Australia, Brazil, Canada, Europe, Israel, New Zealand, Norway, South Africa, and Switzerland. It is also marketed for the treatment of acute myeloid leukaemia, acute non-lymphocytic leukaemia,

ovarian and liver cancer, multiple sclerosis, and non-Hodgkin's lymphoma [28]. It is also marketed as Onkotrone® by Baxter Oncology for the treatment of various cancers.

In the US, MX has been launched for the treatment of acute myelogenous, monocytic, promyelocytic and erythroid leukaemias and as an initial, palliative treatment for pain associated with advanced, hormone-refractory prostate cancer [28].

1.2.4. Second effects and hurdles

Despite preventing the proliferation of malignant tumor cells, MX irreversibly binds to nuclear DNA in a nonspecific manner, killing both proliferating and non-proliferating cells [23]. Therefore, the clinical value of MX is limited due to significant adverse effects such as myelosuppression and cardiotoxicity and by the occurrence of multidrug resistance associated with the overexpression of certain membrane transporters including P-glycoprotein, MRP1, BCRP/MXR1 [33]. Nevertheless, compared to the better known anthraquinone derivatives of the anthracycline family, such as daunomycin and doxorubicin, MX proved to be comparatively more reactive, while being less cardiotoxic [26, 29].

Tolerability of MX has been evaluated in several clinical trials. Haematological toxicity, in particular neutropenia, is the most common dose-limiting adverse event observed during MX therapy [28]. In a trial in which MX was administered in combination with hydrocortisone to 112 patients with hormone-refractory prostate cancer, 70% experienced grade 3/4 haematological toxicity. Thrombocytopenia and anaemia are less common effects and rarely severe. The incidence of cardiac toxicity was estimated to be about 3% and was generally dose-dependent. A phase II clinical trial showed a limited antitumor activity in patients with breast cancer at the cost of adverse myelosuppression and cardiotoxicity [28].

Other adverse events reported during MX therapy include leucopenia nausea and vomiting, anorexia, constipation, alopecia, malaise and oedema [28].

The lack of tissue specificity causing the occurrence of the reported adverse effects of this important chemotherapeutic drug can be overcome by resorting to the nanotechnology.

1.3. Nanotechnology and cancer

Nanotechnology is an emerging multidisciplinary field of sciences that works in the investigation and manipulation of atomic or molecular structures of nanometric dimensions. The concept of nanotechnology was suggested by Richard Feynman in 1959, the term “nanotechnology” was introduced by Taniguchi in 1974 and the strategies of nanotechnology were later described by E. Drexler in 1986 [40]. Today, nanotechnology is applied to several areas of science including pharmacy, physics, biology, and materials science. The application of nanotechnology for healthcare purposes is known as nanomedicine [40].

Nanoparticle systems can play a vital role in drug delivery to improve the treatment of cancer disease by counteracting several limitations of the standard drug therapies. Those include limited biodistribution and accumulation if the region of interest, resulting in suboptimal efficacy, accumulation in healthy tissues leading to high toxicity, undesirable pharmacokinetics such as quick clearance and short half-life and tumor drug resistance [6].

This ability to improve conventional drug therapies can be attributed to different characteristics of the nanoparticles. First, they are relatively small in size compared to cells, but bigger than most small molecules and drugs. This distinctive feature can improve their retention time in circulation and improve the bioavailability and pharmacokinetic profile of various drugs. Secondly, their particular size promotes enhanced permeability and retention (EPR) effect seen in many rapidly growing solid tumor, in which leaky tumor vasculature and poor lymphatic drainage lead to particles selective retention and accumulation in in solid tumor tissues [41].

Furthermore, nanoparticles can utilize a natural process called endocytosis to enter the cells, which presents a particular advantage in situations where normal entry into cells would be challenging for a given molecule. On the other hand, this feature enables targeting specific organelles inside the cells such as nuclei [40]. The high surface area-to-volume ratio of nanocarriers provides an opportunity to manipulate their surface properties to improve treatment, such as extended circulation and increased endocytosis and transcytosis. In fact, protective hydrophilic polymers such as polyethylene glycol (PEG) have been used to prolong the circulation of nanocarriers in the blood by shielding their surface and thereby reducing opsonization and subsequent uptake by macrophages of the reticuloendothelial system (RES). Furthermore, nanoparticles can be surface modified with specific ligands, antibodies or peptides to achieve tissue targeting, which reduces the likelihood of nonspecific off-target toxicity. Moreover, by entrapping in or binding onto nanocarriers, the therapeutic agents can also gain better stability, increased solubility and controlled release kinetics [6].

Apart from the valuable role that nanotechnology plays in cancer prevention and treatment, the fusion of nanotechnology with biological materials also allowed for improvements in different areas of cancer such as drug discovery, diagnostic and therapy monitoring, including early detection and treatment of various cancers and preparation of fluorescent biological labels for both imaging and therapeutics [40, 42].

1.3.1 Nanotherapeutics for breast cancer treatment

Breast cancer is the most common malignant disease in women worldwide, but the current drug therapy is far from optimal. The need to improve the health benefits of chemotherapeutic drugs has prompted the development of nanoparticles (NPs) for drug delivery, which represent a promising alternative for standard breast cancer treatment [42]. Actually, nanomedicines in the field of cancer management have been shown to enhance drug permeability and retention in tumor tissues, thereby decreasing their accumulation off-target. These achievements allow for increased efficacy and lower drug dosages, which means reduced adverse effects [40]. Moreover, nanoparticles enable an improved stability, reproducibility and delivery of medicines, in a controlled and targeted manner.

Some nanoparticulate formulations for cancer treatment have received FDA approval and numerous are under development in various clinical stages, for instance, polymeric conjugates of asparaginase and polymeric micelles of PTX have been recommended for various types of cancer treatment. Commonly used types of NPs range from liposomes, NPs, micelles, dendrimers, nanotubes, among others. Table 1 summarizes some of these NP formulations [40].

Table 1 Examples of FDA-approved nanoparticulate formulations

Drug product	Active compound nanoplatform	Manufacturer	Indications	FDA approval year
Abraxane	Albumin-bound paclitaxel	Abraxis Bioscience, Astra Zeneca, Celgene	Metastatic adenocarcinoma Non-small cell long Brear cancer	2013 2012 2005
Ferumoxytol	Iron oxide nanoparticles	AMAG Pharmaceutic	Iron deficiency	2009
Marqibo	Vincristine	Talon Therapeutics	Philadelphia Chromosome-negative lymphoblastic leukemia	2012
Oncaspar	PEGasparaginase injectable solution (polymeric nanoparticle)	Enzon	Acute lymphoblastic leukemia	2006
Rapamune	Nanocrystals Sirolimus	Pfizer Inc.	Immunosuppressant	2000
Myocet	Liposome-encapsulated doxorubicin	Elan/Sopherion therapeutics	Breast cancer	2000, approved in Europe
DepoCyt	Liposomal cytarabine	Skye Pharma, Enzon	Lymphomatous meningitis	19991
AmBisome	Liposomal amphotericin B	Astellas	Fungal infections	1997
Feridex	Iron oxide nanoparticles, injectable solution	AMAG Pharma	Constrast agent for MRI	1996
DaunoXome	Daunorubicin citrate liposomes	Gilead Sciences	HIV-related Kaposi sarcoma	1996
Doxil	PEGylated liposome of doxorubicin	Ortho Biotech	Ovarian cancer	1995
ThermoDox	Heat-activated liposomal doxorubicin	Celsion	Breast cancer, primary liver cancer	2013
Resovist	Iron oxide nanoparticles coated with carboxydextran	Bayer Schering Pharma AG	Liver/spleen lesion imaging	2001, approved in Europe
Endorem	Iron oxide nanoparticles coated with dextran	Guerbet	Liver/spleen lesion imaging	2001, approved in Europe
Genexal-PM	Paclitaxel-loaded polymeric micelle	Samyang	Breast cancer/small cell lung cancer	Marketed in Europe, Korea

HIV human immunodeficiency virus; *MRI* magnetic resonance imaging

The majority of nanotherapeutics products already in the market are for parenteral or oral administration [42].

Nanomedicine products such as Doxil® and Abraxane® have already been extensively used for breast cancer adjuvant therapy with favorable clinical outcomes [6]. Besides these two products, there are other promising anticancer nanoformulations that have entered clinical phase.

Some examples of the present state of NP drug delivery in breast cancer are described below in more detail and are grouped according to the type of NP used.

1.3.2 Nanoparticle platforms currently investigated for clinical in breast cancer

1.3.2.1 Liposomes

Liposomes were initially described by Bangham and coworkers in 1964, and their potential for drug delivery reported a decade later [16].

Liposomes are of great interest as they are able to effectively deliver water-soluble (hydrophilic) drugs, hydrophobic drugs, peptides, and nucleic acids. In fact, liposomes are simplified models of biological membranes and thus present an aqueous core surrounded by a phospholipid bilayer membrane that allow the incorporation of water-soluble drugs and genetic material such as genes and siRNA within the core and hydrophobic drugs within the double layered lipidic membrane [40]. Additionally, liposomes are considered to be biologically inert and biocompatible due to their biological nature [40]. Their spherical small size, typically on the order of 100 nm, proves to be ideal for long systemic circulation and enhanced accumulation in tumors through the EPR effect [16].

Doxil, is the first FDA-approved nanodrug in 1995. It is a PEGylated liposomal formulation of doxorubicin with size of about 85 nm in diameter. Doxil was designed to reduce the systemic toxicity of doxorubicin, such as cardiotoxicity [6]. Encapsulating doxorubicin within PEGylated liposomes significantly increased the blood circulation time of the drug from a scale of minutes to days [16]. This nanoformulation could avoid premature elimination by the RES and extend circulation time. This nanocarrier system also confirmed the capability of nanoformulations to achieve good intratumoral drug level by EPR passive targeting effect [6]. In the clinic, Doxil have shown to markedly suppress tumor growth rates and improve survival, with diminished cardiotoxicity and clinical heart failure, as reported by Harris et al. [6].

Different clinical trials using a combination of Doxil with other chemotherapeutics including docetaxel (DTX) and PTX and targeted therapy, such as trastuzumab, for breast cancer treatment in different stages, showed improved response rates and disease progression in addition to low toxicity [16]. It is worth noting that recent meta-analysis showed that despite Doxil reduced cardiotoxicity, it leads to new side effects such as skin toxicity and mucositis, nevertheless, these side effects are clinically much less serious than cardiotoxicity [6].

Another promising anticancer nanoformulation that have already entered clinical phase is the Lipoplatin®, a liposomal nanocarrier of 110 nm diameter that incorporates the alkylating agent cisplatin. In numeral clinical trials, Lipoplatin enhanced cisplatin retention in tumor tissue and substantially reduced renal toxicity, peripheral neuropathy, ototoxicity and myelotoxicity [6]. Although its official indication is for non-small cell lung cancer, this product also has potential to be included in the treatment of breast cancer. In a Phase II study of Lipoplatin/vinorelbine combination in ERBB2 negative metastatic breast cancer, complete and partial responses were achieved in the majority of patients with fewer disease progression. Besides, no grade 3/4 nephrotoxicity or neuropathy secondary effects were noted [43].

Furthermore, in 2015, Onivyde®, a nanoliposomal formulation of irinotecan, is FDA-approved for metastatic pancreatic cancer [6]. Irinotecan is not a commonly used drug for breast cancer, however, in a Phase I study with advanced refractory solid tumors that include breast cancer, the disease control rate with Onivyde was 45.5% [6]. In the overall, Onivyde showed to be well tolerated.

1.3.2.2 Nanoparticle albumin-bound paclitaxel

Taxanes such as PTX and DTX have recently become mainstay drugs in several adjuvant combination chemotherapy regimens, oftentimes supplanting the well-known anthracyclines and platinum-based agents [16]. Despite the positive outcome in both disease free and overall survival of breast cancer patients following PTX administration, the hypersensitivity reactions and neuropathy resulting from the drug and excipient materials in the formulation, prove dose limiting.

A NPs albumin-bound (nab) paclitaxel, referred by its trade name Abraxane, was initially developed as a solvent-free PTX formulation, once the surfactant Cremophor EL and the co-solvent ethanol used to solubilize PTX (PTX CrEL) are responsible for high incidence of hypersensitivity reactions, which call for premedication with corticosteroids and antihistamines to counter the effects [6].

Protein nanocarriers, such as albumin, can be obtained from several sources and offer as advantages a high capacity to bind to various drugs due to the amine and carboxylic group on its surface, a non-immunogenic character and long life in the circulating plasma [44].

Nab-PTX consists of PTX stabilized with serum albumin, ultimately resulting in a colloidal suspension of NPs averaging 130 nm in size. Upon injection into the bloodstream, the NPs dissociate into albumin-bound PTX components. At the tumor site, the albumin-drug complex binds to the 60-kDa glycoprotein (gp60) receptor expressed on the surface of continuous endothelium, and after subsequent binding to caveolin-1, PTX is transcytosed to the extravascular space through caveolae [6]. Caveolin-1 is an integral membrane protein found in elevated quantities in breast cancer and is indicative of an aggressive tumor phenotype and poor prognosis [6, 45].

A Phase I pharmacokinetic study of nab-PTX performed by Ibrahim and coworkers demonstrated a marked increase in the maximum tolerated dose (MTD) of the NP formulation compared to PTX CrE, and the overcome of the severe hypersensitivity reactions observed in PTX

CrEL therapy [46]. Further comparative pharmacokinetic studies between nab-PTX and PTX CrE , showed greater volume of distribution and clearance of PTX using nab-PTX, for equal blood half-times [47]. The enhanced bioavailability and elevated intratumoral concentrations of PTX, combined with higher administered doses, resulted in enhanced patient responses. This outcome was also observed in a Phase III trial in metastatic breast cancer patients [48, 49]. These results strongly supported the replacement of the current PTX formulation by nab-PTX for primary breast cancer treatment.

1.3.2.2 Polymeric micelles

Polymeric micelles are an emerging class of NP platforms with apparent chemotherapeutic potential in breast cancer [16].

Polymer micelles are supramolecular NPs composed of amphiphilic block copolymers that self-assemble into core shell constructs in aqueous environments, forming spherical or globular colloidal complexes [44]. This NPs are promising carriers for several water insoluble chemotherapeutics due to their semi-solid hydrophobic core. Polymeric micelles typically possess an inherent hydrophilic PEG corona meant to protect the NP from aggregation and opsonization upon intravenous injection. Their small size (10 to 100 nm in diameter) allows the NP to avoid sequestration by the RES, increase their long blood circulation half-lives and the likelihood of extravasation and accumulation in tumors through the EPR effect. Moreover, the versatility of the block copolymer constituents of polymer micelles enables broad customization and functionalization of this particles.

Several polymeric micelle platforms of drugs such as cisplatin, doxorubicin and camptothecin analog SN-38 have been evaluated in different cancer types, in various stages of clinical trials [16].

Genexol-PM is a PTX micellar formulation that has already advanced considerably in clinical trials in metastatic breast cancer. Clinical studies consisting of intravenous administration of Genexol-PM in patients with metastatic breast cancer resulted in positive rate responses and enhanced median time to progression and absence of the hypersensitivity characteristic reactions of PTX CrEL for some patients. In a Phase II trial there were 19 partial responses to the micellar formulation and 5 patients underwent complete responses among 41 women receiving this therapeutic [16].

1.4. Lipid Nanoparticles

Lipid nanoparticles (LNs) are colloidal carriers characterized by a lipid matrix, solid at both room and body temperature which have emerged in the nineties as an alternative to liposomes, emulsions, and polymeric NPs.

The use of lipid solid matrix as drug vehicles shows great potential for pharmaceutics and cosmetics applications as they provide the possibility for controlled release and site-specific targeting of active compounds. Moreover, they show good stability *in vivo*, provide enhanced drug solubility

and efficient incorporation and delivery of both hydrophilic and lipophilic drug molecules by parenteral and non-parenteral routes of administration [50, 51]

LNs stand out from other types of nanosystems not only for exhibiting high tolerability, owing to the biocompatible and biodegradable nature of the constituents used, but also because of their constitution based on commercially available lipids and surfactants, approved by the FDA, which eases their approval and admission to the clinic. Furthermore, their production process can be free of organic solvents, of low cost and ease of large-scale production [50, 52].

The composition and structure of LNs are the two most critical factors that may influence their pharmaceutical performance. LNs are composed of lipids, surfactants to stabilize the colloidal system and co-surfactants, if necessary. Lipids used in the production are broadly categorized into fatty acids, fatty esters, fatty alcohols, triglycerides or partial glycerides and waxes, and most of them are approved as generally-recognized-as-safe (GRAS) [52]. Surfactants stabilize LNs by decreasing the surface tension between water and lipids [51].

1.4.1. Types of Lipid Nanoparticles

The two main types of LNs are the solid lipid nanoparticles (SLN) and nanostructured lipid carriers (NLC), with a mean particle size ranging from about 40 to 1000 nm, that differ from each other in their content of solid lipids and the lipid matrix arrangement. Other examples of LNs include lipid drug conjugates and polymer-lipid hybrid nanoparticles (PLNs) [53].

SLNs are the first generation of lipid-based nanocarriers. This NPs are prepared using 0.1 to 30% (w/w) of solid lipids dispersed in an aqueous medium and stabilized with a surfactant [54]. This results in the assembly of a well-structured matrix with only a few cavities for drug encapsulation. In fact, SLNs can be classified into three drug incorporation models according to the localization of the drug within their structure (Figure 3, (1)). In the solid solution model ((1), A) the drug is dispersed in the lipid matrix and has strong interactions within the lipid core, the drug-enriched shell model ((1), B) occurs when a drug-free lipid core is formed with drug molecules concentrating on an exterior shell with both lipid and drug at the surface of SLNs and, finally, the drug-enriched core model ((1), C) is obtain when the drug concentration is close to its saturation solubility in lipid, which will yield to its precipitation in the core and to the formation of a lipid coverage [53, 55].

In turn, NLC are produced using blends of solid lipids and liquid lipids (oils) in a ratio of 70:30 up to a ratio of 99.9:0.1 [54]. This binary composition promotes the formation of a less organized lipid matrix with a larger number of cavities. Depending on lipids arranging in the particle (Figure 3, (2)), NLCs can exhibit a imperfectly structured solid matrix ((2), A), with a great number of voids and imperfections where the drug can place itself, a structureless solid amorphous matrix that minimizes drug expulsion ((2), B) or can present a multiple model characterized by small oil NPs that are inside the solid lipid matrix due to a phase separation ((2), C) [53, 55].

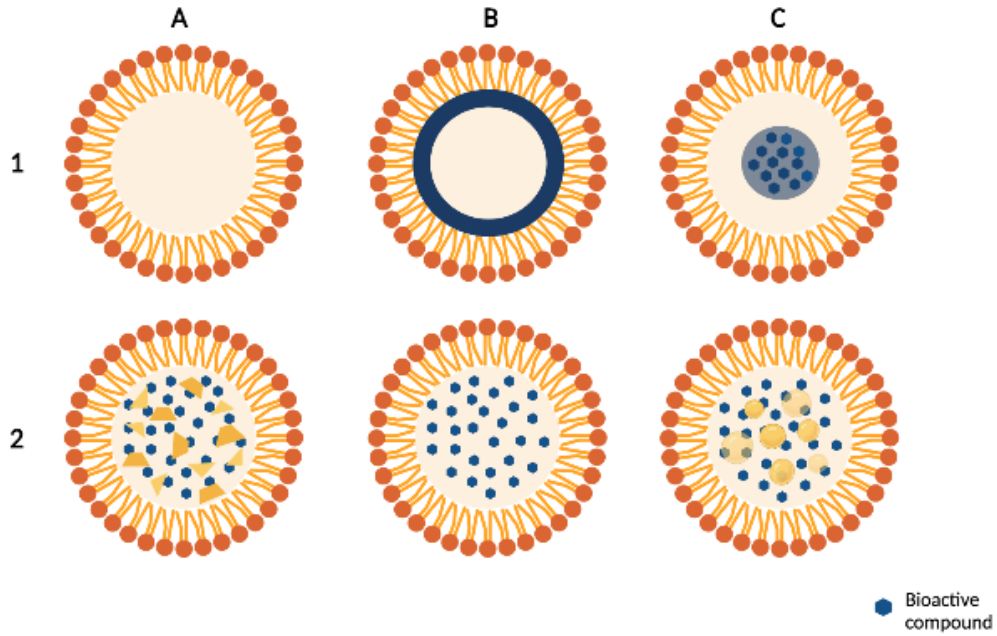


Figure 3 Schematic representation of the different types of SLN and NLC and drug location within the lipid matrix. (1) SLN drug incorporation models: (A) Solid solution model, (B) Drug-enriched shell model, (C) Drug-enriched core model. SLN (A) does not present any "drug" icon due to the homogeneity of the matrix. (2) Different types of NLC: (A) Imperfect crystal model, (B) Amorphous model, (C) Multiple model.

The incorporation of cosmetic and pharmaceutical actives is feasible for both particles, however, because the drug molecules incorporate between the fatty acid chains, lipid layers and in the crystal imperfections, the highly organized crystalline structure of the SLNs may become unfavorable for high drug-loading and can result in drug expulsion during storage [53, 54, 56]. In turn, the second generation of LPs, overcome these limitations due to NLCs bigger amount of imperfections that allows higher incorporation/loading capacity of drugs in the NP with less potential expulsion of the active compound. Additionally, the NLCs multiple models are adequate to obtain a controlled drug release and enhance the loading capacity of drugs that are usually more soluble in liquid lipids [52, 54, 55].

An alternative for the delivery of hydrophilic drugs is the use of lipid drug conjugates (LDCs). The formation of LDCs consists of hydrophilic drugs conjugation with a lipid molecule either by salt formation or by covalent linkage in order to become more lipophilic and insoluble. The LDCs are expected to act as prodrugs and be subject to cleavage (deconjugation) *in vivo* to produce the active form of the drug.

Another nanodelivery system developed as a variation of SLNs are the polymer-lipid hybrid nanoparticles (PLNs), a suitable drug carrier for hydrophilic drugs. The formation of a drug-polymer complex increases drugs partitioning into the lipid matrix [52]. The PLNs offer a retarded and more complete release of some drugs and show the capability to encapsulate and deliver multiple drugs, e.g., for anticancer therapy purposes [57].

1.4.2. Methods of preparation

Method approaches for LNs production include physical techniques and approaches using organic solvents and are described above.

Numerous different methods for the production of LNs have been reported in the literature. The choice of the appropriate method is done according to the composition and desired characteristics of the lipid NP, as well as the properties of the drug [51].

SLN assembly involves dispersion of drugs into a melted-lipid phase by using the appropriate solvent or application of mechanical forces. Upon NPs production, fast cooling creates an unstable and disordered α-crystalline structure, which allows the desired drug to be stored in the NP's amorphous areas [56].

The preparation of lipid NPs and final products containing lipid NPs is feasible by well-established, cost-effective and simple production methods of easy scale-up [52, 53, 58].

Method approaches for lipid NPs production include physical techniques and approaches using organic solvents and are described above.

1.4.2.1. High-pressure homogenization

High-pressure homogenization (HPH) technique represents one of the most common methods established for the production of lipid NPs. This process is based on the formation of submicron size particles by pushing a liquid containing the lipid and drug active compound with high pressure through a micron size gap, either at elevated temperature (hot homogenization) or below room temperature (cold homogenization*)*. In both cases the initial step of production is the dissolution or dispersion of the drug in the lipid, which is previously melted at a temperature of 5-10ºC above its melting point [53].

In the hot homogenization the lipid-drug melt is dispersed in a hot surfactant solution and then passed through an HPH to form the emulsion that will recrystallize forming the NPs, after cooling down. In contrast, the cold homogenization is performed after the solidification and break down of the melted lipid containing the drug into microparticles which are then suspended in a cold surfactant and finally submitted to the HPH at room temperature, for the formation of solid LNs [59]. The cold HPH overcomes some limitations regarding the process at high temperatures such as the use of temperature-sensitive drugs, the unintended distribution of drugs into the aqueous phase during homogenization and the complexity of the crystallization step of the nanoemulsion, which can lead to significant modifications of the final product [53].

The HPH technique used for the production of lipid NP is already used in many industries, including the pharmaceutics [54].

1.4.2.2. Microemulsion technique

The microemulsion technique, also feasible for large scale production of SLN, allows the preparation of SLN dispersions by precipitation from a hot microemulsion, a thermodynamically stable system of water and a lipophilic phase, stabilized by surfactants and possibly co-surfactants [58]. The lipids are melted and then stirred gently with a mixture of water and surfactant heated to the same temperature. The microemulsion formed is then dispersed in a cold aqueous medium under mild mechanical mixing causing the lipid droplets to solidify.

1.4.2.3. High shear homogenization and/or ultrasonication technique

High shear homogenization and ultrasonication are dispersing techniques. The lipid NP dispersions are obtained by dispersing the melted lipid in the warm aqueous phase containing surfactants by high sheer homogenization followed by ultrasonication. Sonication reduces the droplet size of the emulsion and gradual cooling of the warm emulsion yields a lipid NP dispersion. Concentrated lipid NP dispersions can be obtained by ultracentrifugation [53].

1.4.2.4. Emulsification-solvent evaporation, emulsification solvent diffusion and solvent injection techniques

In solvent evaporation technique, the solid lipid is initially dissolved in an organic solvent and after the organic phase is emulsified in an aqueous solution of surfactant to yield an organic solvent-in-water emulsion. The lipid NP dispersion is formed by lipid precipitation in the aqueous medium due to solvent evaporation, whereas the lipid crystallization in the solvent diffusion technique results from the diffusion of the solvent from the internal organic phase to the external aqueous phase [53]. In this second approach, the solid lipids are solubilized in partially water-miscible solvents and the transient oil-in-water emulsion is passed into water under continuous stirring, which leads to the solidification of the dispersed phase. Lipid NPs are then formed due to diffusion of the organic solvent.

For the solvent injection technique lipids are dissolved in a water-miscible solvent or water-miscible solvent mixture and quickly injected into an aqueous solution of surfactants through an injection needle. As the solvent diffusion method, lipid crystallization occurs due to rapid diffusion of solvent from internal organic phase to external aqueous phase. The particle size of SLNs and NLCs are influenced and controlled by variation of process parameters such as the solvent injected and its volume, lipid concentration and viscosity of the aqueous phase [53].

Other methods used for LNs synthesis are double emulsion, phase inversion, membrane contractor, multiple emulsion techniques and coacervation technique, among others. The choice of preparation technique for lipid NP dispersions should have into account the physicochemical

properties of the drug to be incorporated, drug stability and desired characteristics of the lipid NP system [58].

1.4.3. Application of Solid Lipid Nanoparticles for Drug Delivery

Application of SLNs as a carrier system could be attributed to their unique features such as enhanced permeation through biological membranes, surface modification, increased resistance to chemical degradation, and ability to deliver two or more therapeutic agents. Various drugs have been investigated as potential agents for incorporation into SLNs, such as timolol, deoxycorticosterone, doxorubicin, diazepam and PTX [51].

There are quite a few anticancer drugs that are hydrophilic and ionic in nature and some lipophilic anticancer agents are better utilized in their salt form as they allow diluting and administering with the aqueous vehicles [51]. Although an efficient incorporation of hydrophilic anticancer actives can be a challenge using SLNs, studies using different lipids and lipid combinations have been proved to successfully enhance the entrapment efficiency of hydrophilic drugs [60-62]. For instance, Bhandari et al. studies demonstrate that the use of appropriate lipid combination in an appropriate ratio, the entrapment efficiency of a hydrophilic drug such as isoniazid could be significantly increased [60]. They achieved an entrapment efficiency of approximately 84%, which is considerably higher than other reported data.

The drug-loading capacity of SLNs is an important factor to consider upon loaded-SLN synthesis. Drug-loading capacities ranging from 1% to 50% have been reported [51].

The drug incorporation models of SLNs described above (Figure 3) define the drug release pattern and can be helpful for modulating drug release by controlling the SLN structure during formulation. In fact, changes in some relevant variables influence SLN and NLC structure and therefore their applicability. For instance, SLN type A can show controlled release properties, whereas SLN type C is adequate in achieving a prolonged drug release. On the contrary, SLN type B will lead to a more immediate release [55].

The encapsulation of hydrophilic and lipophilic drugs by formulating them in SLNs results in their protection from degradation in the body and facilitates their prolonged release.

It is important to highlight that the use of a single lipid for the production of SLNs, unlike NLCs, makes the production cost even more economically viable.

1.4.3.1. Routes of administration

Various researchers have investigated SLNs for oral delivery of a variety of active compounds. In a study performed by Cho et al., SLNs were incorporated with DTX, a drug with poor oral bioavailability and the results indicated an increase in the oral bioavailability of DTX.[63] In another study made by Sarmento et al., SLNs of insulin were prepared using cetyl palmitate and evaluated for oral delivery [64]. Oral administration of the formulated insulin-loaded SLNs to diabetic rats

provided a considerable hypoglycemic effect during 24 h showing SLNs potential as a carrier for oral delivery of insulin. SLNs may be administered orally after transformation into a traditional oral dosage form such as tablets, pellets, capsules, or powders [51].

The application of SLNs in parenteral delivery ranges from intraarticular delivery route to intravenous administration. Various researchers have performed investigations on intravenous performance of SLNs. In a study performed by Zara et al., the pharmacokinetics and tissue distribution of doxorubicin incorporated in SLNs were compared with commercial doxorubicin solution after intravenously administration to conscious rabbits. Brain distribution of doxorubicin was obtained only with SLNs and SLNs were found to significantly reduce the heart and liver distributions of doxorubicin [65]. Meanwhile, Manjunath et al. assessed the bioavailability of nitrendipine-loaded SLNs following intravenous and intraduodenal administration to rats [66]. An increase in area under the curve and decrease in clearance was observed with nitrendipine-loaded SLNs when compared with the nitrendipine suspension. The effective bioavailability of the nitrendipine SLN was found to be higher after intraduodenal administration when compared with nitrendipine suspension, thus proving the suitability of SLNs as carrier system for improvement of bioavailability of nitrendipine.

Many other routes of administration of SLNs have been investigated such as topical, pulmonary, rectal and ocular routes, demonstrating the versatility of this type of lipid nanocarriers [51].

1.4.3.2. SLN as Potential Carriers of Anticancer Agents

SLN have been demonstrated, *in vitro* and *in vivo*, to have lesser side effects with an increase in the efficacy and residence time of cytotoxic drugs for cancer treatment [51].

Firstly, SLNs are found to have enhanced EPR effect. On the other hand, because of SLN versatility and capability of incorporate both hydrophobic and hydrophilic drugs, this NPs have the ability to load cytotoxic agents that could not bind to polymeric NPs [51].

Yang et al. performed a study to investigate the specific targeting of the anticancer drug camptothecin after incorporation into SLN and compared it with camptothecin solution, after intravenous administration [67]. The HPH technique was used to formulate the SLN with a mean diameter of 196.8 nm and a zeta potential of 69.3 mV, which presented prolonged *in vitro* drug release of up to 1 week. The area under the curve and mean residence time of the camptothecin SLN in the tested organs were found to be much higher than the camptothecin solution. These data demonstrate SLN's potential as a sustained drug release and targeting drug delivery system.

Another relevant study was made by Lee et al. to evaluate NPs cytotoxic to cancer cells [68]. This group developed a formulation of PTX-loaded SLN intended for parenteral administration. Hot homogenization technique was performed and resulted in particles with around 200 nm in size and zeta potential of 38 mV, suggesting its applicability for parenteral use. Cytotoxicity was tested on the MCF-7 breast cancer cell line and the OVCAR-3 human ovarian cancer cell line and were found to be comparable with those of the commercially available Cremophor EL-based PTX formulation In

another study, tamoxifen-loaded SLNs were investigated by Fontana et al. against breast cancer [69]. The SLN in the intact form demonstrated a prolonged release of drug following *in vitro* plasmatic drug release studies. Also, the *in vitro* cell viability studies carried out on MCF-7 human breast cancer cell line, indicated an antitumoral activity comparable with the free drug.

Therefore, SLN have been shown to be good candidates as carrier system for the prolonged delivery of anti-cancer drugs via intravenous administration.

1.5. Targeted delivery of nanoparticles to cancer cells

When designing NPs for the delivery of anticancer agents, the goal is to simultaneously achieve high tumor accumulation and enhanced cellular internalization [70].

The adverse effects and relatively low drug efficacy of chemotherapeutics caused by the non-specific distribution in tissues and failure to reach tumor tissues can be overcome by increasing blood circulation time of drugs and resorting to both passive and active targeting strategies.

Passive targeting is a consequence of the EPR effect that occurs in many solid tumors and that enables the accumulation of the anticancer drugs at tumor sites [41]. However, passive targeting alone cannot provide the required drug efficiency owing to the lack of cell specificity of the nanocarriers and the clearance mechanisms from the blood circulation. The particle size, surface charge, and surface modification of nanocarriers are particularly important factors to consider for efficient extravasation in passive targeting as well as for longer drug systemic circulation. Nanocarriers sized between 10 and 100 nm realize efficient extravasation as well as reduce liver capture and renal filtration [41]. Neutral or negative surface charge and PEG coating are also able to prolong nanocarriers circulation time by protecting them against the attack of plasma proteins and opsonization by the RES [44].

After reaching tumor tissues, NPs should be able to either release the drug extracellularly or enter tumor cells to achieve intracellular drug delivery since many of the commonly used antitumor drugs, such as MX, doxorubicin and PTX, , act on intracellular targets (DNA and microtubules) [44]. Several strategies have been recognized to actively achieve enhanced drug accumulation within the target cells. The use of positively charged surfaces may enhance cellular NPs internalization by effective binding to cell membranes by strong electrostatic interactions. Moreover, conjugating tumor-specific receptors into nanocarriers allow their accumulation within the target tissue [41].

Overexpressed tumor-specific receptors include EGF and ErbB2 receptors, the leptin and transferrin receptor, respectively. The ligands hyaluronic acid or hyaluronan (HA) and folic acid (FA) of the cluster of differentiation (CD44) and folate receptors, respectively, along with certain antibodies, peptides, small molecules and many other ligands that specifically bind to tumor receptors can be added to drug-delivery systems, contributing to an improved tumor-targeting effect [41]. However, because most of these receptors are not exclusively expressed in tumor cells, this approach may result in low drug-delivery efficiency and severe toxicity [37, 71, 72].

Recently, the ability to respond to the local stimuli of the tumor microenvironment, including low pH, redox-potential, and specific enzymes, has been introduced as a targeting strategy [41]. Tumor hypoxia and pathological pH change in tumors are stimuli that have been well investigated. Metal-based prodrugs with redox activation, nanomaterials with enzyme-response and light-triggered nanocarriers have been reviewed elsewhere [71]. Stimuli-responsive NPs are able to change their structure in different environments and act in the desired place [41]. Drug-delivery systems sensitive to the characteristic extracellular acidic pH of solid tumors and also to acidic lysosome pH have been constructed for efficient drug release in tumor cells [71].

1.5.1. CD44-Hyaluronan interaction and cancer treatment

One of the most investigated ligands for targeted delivery of chemotherapeutics is the polysaccharide HA, previously mentioned to specifically bind to CD44 receptor, found in many cancer types. Although being expressed on a variety of human cell types, CD44 is abundantly overexpressed in certain tumor types such as melanoma, lymphoma, colorectal, breast, and lung tumor cells [41, 72].

CD44 is a cell transmembrane adhesion glycoprotein with a molecular weight of 85–250 kDa [37]. Two CD44 isoforms are produced when distinct alternative splicing occurs during the transcription process and include the standard isoform (CD44s) and CD44 variant isoforms (CD44v) (Figure 4) [72]. CD44 gene is composed of 19 exons in human, among which the first five exons and the last five exons encode CD44s which is the most common CD44 protein with a molecule weight of 85–95 kDa. The exons 1–5 and exons 16–20, encode N-terminal containing HA-binding region and C-terminal domain of CD44 protein, respectively. The middle nine exons can be alternatively spliced subsequently encoding the many CD44 variants.

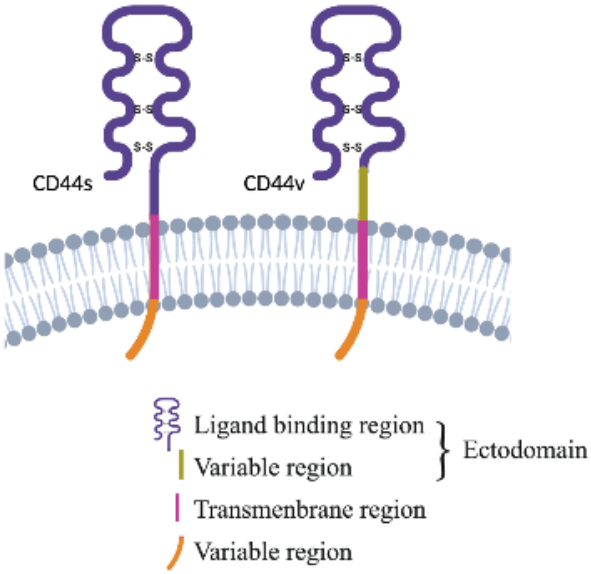


Figure 4 Structure of CD44 protein. CD44 mainly consists of three regions: the extracellular, transmembrane and intracellular domains. Compared to CD44s, the extracellular region of CD44v protein additionally contains a variable domain

Numerous studies have reported that CD44 not only participates in normal cellular functions during physiological processes, but also mediates pivotal roles in pathological processes, especially tumors [37, 72]. Some cancer signaling pathways related to tumor growth, angiogenesis, progression and metastasis are associated to CD44 activation by HA [37]. This diversity in biological activity is conferred by both a variety of distinct CD44 isoforms, posttranslational modifications, interactions

with a number of different ligands, and the abundance and spatial distribution of CD44 on the cell surface [73].

There are several common ligands to which CD44 binds, including HA, bronectin, serglycin/sulfated proteoglycan, osteopontin and chondroitin, however, HA ubiquitous ECM component represents the most common ligand of CD44 [72]. The combination of HA and CD44 activates multiple pathways involved in cell adhesion, migration and proliferation including Ras, mitogen-activated protein kinases (MAPK) and phosphoinositide 3-kinase (PI3K) [72]. It has been reported that HA binding to CD44 enhances proliferation and survival of breast cancer cells through modulating ß-catenin signaling and nuclear factor-kappa B (NFκB)-specific transcription activity in breast cancer MCF-7 cells [72].

Since the discovery of CD44 overexpression in cancer cells, targeting of CD44 for anti-cancer therapy has been attempted using DNA vaccines, anti-CD44 monoclonal antibodies, NP-mediated delivery of CD44siRNAs [73].

Further studies of the interaction between HA and CD44 receptor, showed HA inherent ability to target the CD44 receptors and internalize into tumor cells via receptor-mediated endocytosis [37, 73]. Therefore, HA-coated NPs have been used to target CD44+ cells for the delivery of anticancer agents [73].

HA is a high-molecular-mass glycosaminoglycan (GAG) found predominantly in the extracellular matrix (ECM), between cells. It is widely distributed throughout connective, epithelial and neural tissue, but is especially present in soft connective tissues. Over 50% of total body HA occurs in the skin [74, 75].

This linear polysaccharide can reach a size of 6 to 8 MDa with the repeating disaccharide structure of (-b1,3-N-acetyl-D-glucosamine-b1,4-D-glucuronic acid-)n. It has one carboxyl group per disaccharide unit and is therefore a polyelectrolyte with a negative charge at neutral pH (Figure 5) [76]. Hyaluronan, at low concentrations, is ubiquitous in the organism. On the other hand, it is found in high concentrations during embryogenesis, and whenever rapid tissue turnover and repair are occurring, as in the case of malignancy [75].

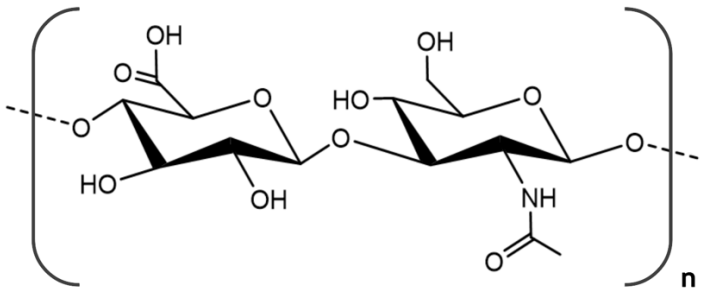


Figure 5 Structural formula of hyaluronan

Hyaluronan is a glycosaminoglycan critical for maintaining the integrity of the ECM and has been assigned with various physiological functions in the intercellular matrix, including water and

plasma protein homeostasis [74]. In extracellular medium, in a protein-bound state, it expands the ECM and modulates cell-cell interactions [74, 77].

Elevated extracellular levels of HA are found in certain malignancies, potentially due to mismatched synthesis and degradation [77]. At the cellular level, a burst of HA synthesis occurs prior to mitosis. The deposition of HA preceding mitosis promotes detachment and motility upon cells, so they lose the adhesion from their surrounding ECM and preparation for division. This phenomenon is possibly correlated with the movement of metastatic tumor cells [75].

HA, like other GAGs, influence the behavior of malignant cells due to their expansive configuration and by regulation of basic processes such as proliferation, recognition, adhesion modulation, and cell-cell communication [75]. In addition to its supportive role, it creates intracellular and extracellular connections and is involved in the transduction of key intracellular biological signals.

HA is either anchored firmly in the plasma membrane or bound via hyaluronan-specific binding proteins, such as the receptor CD44 [74]. The molecular weight of HA is a relevant variable that can influence its affinity with the receptor. As a rule, high molecular weight HA (≥ 30 kDa) free in solution, grafted to liposomes or coated in NPs seems to create stronger binding to CD44 compared to a low molecular weight HA (< 30 kDa) [78]. Spadea et al. believe that this occurs since the longer HA chains can have multiple interactions with CD44 molecules, leading to an increased affinity, and also by favoring receptor clustering and enhancing HA internalization into cells [78]. Moreover, several studies showed that, depending on their molecular size, HA fragments are able to compete with the endogenous HA for binding to the HA receptor and inhibit the signaling pathways that are initiated by the HA binding to CD44. This binding has been proven to reduce the aggressiveness of various types of cancer cells [79]. In a study performed by Tavianatou et al., HA fragments of 10, 30 and 200 kDa were evaluated in terms of their effects on breast cancer cells' functional properties, morphology and gene expression [79]. Among the HA fragments tested, the 200 kDa HA fraction exhibited the highest effects on breast cancer cells. Although all synthesized fractions were able to inhibit breast cancer cell migration, only this fraction was able to inhibit cellular invasion and manage to achieve a less aggressive phenotype. In another study conducted by Jiang et al., the physical forces between HA ligand and its specific receptor CD44 were measured, at different HA molecular weights [80]. It was observed that HA-CD44 specific interaction enhances with HA molecular weight and the maximum binding occurs with ~1000 kD HA. With decreasing MW, the adsorbed amounts decreased strongly, and binding became progressively weaker or reversible. For MW above 262 kD, binding was irreversible and independent of MW or concentration. Stable half-maximal binding occurred at ~30 kD. In contrast, other studies investigating the influence of HA of different molecular weights on cell targeting therapies prove the opposite. A study carried out by Lu et al. demonstrated showed that a 63 kDa HA exerted improved targeting effect highest cytotoxicity compared with NPs functionalized with a higher MW HA of 103 kDa [81]. In fact, the influence of HA MW on promoting HA-based NPs targeting ability is still controversial and a matter of debate [81-83].

1.5.2. Hyaluronic-acid modified nanoparticles

A variety of HA-modified NPs have been developed, such as LNs, polymeric and inorganic NPs [41, 84, 85].

Lipid-based nanocarriers have been playing a prominent role in the investigation of cancer therapies using HA-labeled NPs. Szoka and colleagues prepared HA-modified LNP loaded that showed an enhanced therapeutic effect compared with a bare LNP, which represents the first report of HA-modified LNP [84]. Wang X et al. modified cationic LNPs with ribonuclease (RNase A)-conjugated HA and showed that RNase A-loaded LNPs demonstrated a significant cell-killing effect in CD44-positive A549 [85].

Fundamentally, there are two methods for modifying HA, namely, electrostatic interactions and covalent conjugation. Since HA is a negatively charged polysaccharide, cationic NPs can be electrostatically associated with the molecule. Yu Sakurai and Hideyoshi Harashima pointed out that approximately 30% of HA-NPs were formulated by electrostatic interactions and the remaining by chemical modification. For chemical modification, the most frequently reported method is the formation of amide linkage between the carboxylic group in HA and amine in the compounds. In some reports, a primary amine is used for conjugation to the end of HA. Through these modifications, moieties such as polymers and lipids can be conjugated to form NPs [84].

Besides good binding affinity for CD44, HA offers advantages such as biocompatibility, non-toxic and non-immunogenic properties, making it a very attractive applicant as a target ligand for nanocarriers [41, 86-88].

1.6. Aim and objectives

The goal of this work is to develop an innovative and economically viable MX drug delivery system based on SLN for the treatment of breast cancer, aiming to reduce the systemic side-effects of the drug and improve its tumor targeting ability. In order to do so, SLN were functionalized with HA to target the CD44 receptor. The influence of the MW of HA was investigated by using two distinct HA molecular weights: 20-60 kDa and 1000-1800 kDa The study comprised the fabrication of HA-functionalized SLN loaded with MX, the evaluation of their physicochemical properties (hydrodynamic particle size, zeta potential, drug loading and EE), the study of the release profile of MX at different pH, evaluation of its hemolytic activity and the determination of their cytotoxicity and targeting capability in a human breast cancer cell line CD44+.

Chapter 2 Materials and Methods

2.1. Materials

Lipid Cetyl Palmitate was provided by Gatefossé (Gatefossé, France). Hyaluronan (HA) was purchased from Freshine Chemicals Company (Las Vegas, USA) and phospholipid dipalmitoyl phosphatidylethanolamine (DPPE) from Avanti Polar lipids (Merck, Darmstadt, Germany). Cetyltrimethylammonium bromide (CTAB) and sodium hydroxide were acquired from VWR International (Radnor, PA, USA). Tween® 80, TritonTM X-100, Trypan Blue powder, 1-Hydroxy-2,5-pyrrolidinedione (NHS), 5-Ethynyl-2′-deoxycytidine, (EdC), Hydrochloric acid (HCl), Sodium chloride, Sodium acetate solution, N-hydroxysuccinimide, Dichloromethane, Dimethyl sulfoxide (DMSO), Resazurin sodium salt, Dulbecco's Phosphate Buffered Saline 10X (PBS), Formalin solution neutral buffered 10%, Mitoxantrone hydrochloride and Deuterium oxide (D2O) were obtained from Sigma-Aldrich® (St Louis, MO, USA). Dulbecco's Modified Eagle's Medium (DMEM), GlutaMAXTM-I, 0.25% Trypsin-EDTA (1X), Penicillin-Streptomycin (Pen Strep), Fungizone (amphotericin B, 250 µg mL−1) and Heat Inactivated Fetal Bovine Serum (FBS) were purchased from Gibco® by Life TechnologiesTM (UK). Hoechst 33342®, Trihydrochloride, Trihydrate and LysoTracker™ Green DND-26 were obtained from (Invitrogen, Thermo Fisher Scientific, MA, USA). MCF-7 (passages 61 to 69) was purchased from from ATCC (Middlesex, UK).

All the weighting measurements were performed using a Kern ABT 120-5DM digital analytical balance (Kern & Sohn; Balingen, Germany). pH measurements were obtained using a Crison pH meter GLP22 with a Crison 52-02 tip (Crison; Barcelona, Spain). Ultrapure water was purified by an Ultra-pure water system (18.2 MΩ cm, Healforce, Shanghai, China) by a reverse osmosis process.

2.2. Production of Solid Lipid Nanoparticles

SLNs were produced using the hot ultra-sonication technique as previously described [89]. Hot ultra-sonication is a dispersing technique where lipid NP dispersions can be obtained by ultrasonication of the melted lipid-surfactant solution in the warm aqueous phase. Sonication reduces the droplet size of an emulsion and gradual cooling of the warm emulsion yields a lipid NP colloidal dispersion [53].

The formulation chosen for the production of SLN was first established in previous studies made by Granja *et. al* and consists of solid lipid Cetyl Palmitate® (210 mg), surfactant Tween® 80 (70 mg) and PBS 1x pH 8.2 (4.4 mL) [89]. Cetyl palmitate (Hexadecyl hexadecanoate) is a FDA-approved palmitate ester resulting from the formal condensation of palmitic acid with palmityl alcohol. This white solid wax substance is employed in the industry as a thickener and emollient in cosmetic formulations [90]. The chosen surfactant Tween® 80 (Polysorbate 80), also known as polyethylene glycol sorbitan monooleate, is a non-ionic detergent commonly used as an emulsifier

and is approved by FDA for injectable, oral and topical medication administration [91, 92]. Also, it has been applied in drug formulations used in chemotherapy, such as DTX [51, 93, 94].

For SLN synthesis by hot ultra-sonication, the lipid is melted at a temperature of 5-10 °C above their melting point and mixed with a pre-heated aqueous solution. The mixture is then subjected to ultrasonication to reduce the pre-emulsion droplets size. The droplets of the hot colloidal emulsion are recrystallized by cooling the emulsion to room temperature in order to generate SLN/NLC.

In this work, the solid lipid together with the surfactant were melted at 70 °C in a water bath (Variomag Electronicrührer, Labortechnik, Munich, Germany). After complete melting, 4.4 mL of pre-heated PBS was added to the lipid phase and quickly stirred for partial homogenization before ultrasonication using a probe sonicator (VCX130, Sonics and Material Vibra-CellTM with a CV-18 probe; 115 Newtown CT, USA) at 70% for 5 min. The produced nanoemulsion was cooled at room temperature and stored at 4 °C until further use.

For the production of MX-loaded SLN, 4.5 mg of MX were dissolved in the aqueous phase and added to the lipid phase obtaining a drug concentration corresponding to approximately 0.02% per mass of lipid. The drug-loaded nanoformulation was obtained by ultrasonication as previously mentioned.

2.3. Synthesis of 1,2-Dipalmitoyl-sn-glycero-3-phosphoethanolamine-hyaluronic acid conjugate

Hyaluronan (HA) was linked to the phospholipid dipalmitoyl phosphatidylethanolamine (DPPE) to obtain a HA-conjugate able to coat the surface of the solid LNs. Two distinct HA molecular weights were investigated, HA 20-60 kDa and HA 1000-1800 kDa.

The synthesis of 1,2-Dipalmitoyl-sn-glycero-3-phosphoethanolamine-HAconjugate (DPPE-HA) was performed, as previously described, in four main steps: activation of the hyaluronic acid, coupling to DPPE, purification (removal of excess reagents) and lyophilization [95, 96].

At first, 0.1 g of HA in the salt form were dissolved in 50 mL of ultrapure water to a final concentration of 2 mg/mL by sonicating the two components in an ice bath for 15 minutes. After that, the HA suspension was mixed with 0.5 g of ethyldimethylaminopropyl-carbodiimide (EDC) and 0.52 g of N-hydroxysuccinimide (NHS) and the pH was adjusted to 4 using a 1M HCl solution. The obtained solution was then incubated for 2 hours at 37°C in an incubator (ES-60, Lan Technics, USA) for preactivation of the carboxyl group of the HA. The next step consisted of adding 0.1 g of DPPE to the HA solution at pH to 8.6 adjusted using borate buffer (pH = 10), followed by incubation for 24 hours at 37°C, for the coupling of DPPE to the previously activated HA. To remove the excess of reagents and by-products at the end of incubation the conjugate solution was centrifuged at 4500 RPM at 4°C for 50 minutes (Allegra X-15R Centrifuge, Beckman Coulter, Fullerton, California) and washed three times with PBS buffer, reducing the pH back to 7.4. In the protocol that we based this procedure on used 5500 RPM for 40 minutes, however, since this would exceed the maximum limit of

the centrifuge used, the protocol was adapted to 4500 RPM for another 10 min. In order to remove unconjugated HA, the DPPE-HA solution was dialyzed against 500 mL of ultrapure water (double deionized) using a dialysis membrane, molecular weight cut off (MWCO) of 6-8 kDa (Spectrum Labs, CA, USA) for 48h. At last, the solution of HA-DPPE conjugate was frozen at -80°C and lyophilized for 72h using a freeze dryer (LyoQuest −85 plus v.407, Telstar) and the obtained white dry powder was stored at -25°C until further use.

Aliquots of the HA-DPPE solution were collected before and after the first centrifugation in order to evaluate the amount of HA lost in the first washing step using the hexadecyltrimethylammonium bromide turbidimetric method (CTM), as reported previously (described in detail in the section 2.7.).

The final DPPE-HA compound was analyzed by FTIR and NMR spectroscopy techniques to assess the chemical bonding that was sought to be established between the lipid and the HA polymer.

2.4. Nuclear magnetic resonance analysis

Nuclear magnetic resonance (NMR) was used to verify whether the covalent bond between the lipid DPPE and the HA polymer had been established upon synthesis of the conjugate.

The principle behind the NMR technique lies on the measurement of the interaction of nuclear spins of a molecular sample when placed in a powerful magnetic field. A nucleus that possesses a magnetic moment, such as a hydrogen nucleus 1H or carbon nucleus 13C, that is placed in a strong magnetic field will begin to spin. An NMR spectrum characteristic of each molecule atomic group can be obtained by irradiating radio waves at the same frequency as the precession frequency of the sample [97]. From an NMR spectra it is possible to gather information about the composition of atomic groups within a molecule or even interaction between molecules [98].

To evaluate the conjugation of HA and DPPE, the samples (DPPE, HA 20-60 kDa, HA 1000-1800 kDa and the conjugates DPPE-HA 20-60 kDa and DPPE-HA 1000-1800 kDa in the salt form) were dissolved in deuterium oxide (D2O) in a microtube, vortexed and placed in an ultrasound bath for 10 minutes until proper dissolution. Then the samples were transferred to the NMR tubes. The 1H spectrum of each sample was analyzed, regarding the presence of resonance signals characteristic of each component (HA20, HA1000 and DPPE).

NMR spectra of HA polymers were recorded on a Bruker Avance III 400, operating at 400.15 MHz for 1H atoms, equipped with pulse gradient units, capable of producing magnetic field pulsed gradients in the z-direction of 50.0 G/cm. NMR spectra of DPPE and conjugates were recorded on a Bruker Avance III 600 HD spectrometer, operating at 600.13 MHz for 1H, equipped with 5 mm CryoProbe Prodigy and pulse gradient units, capable of producing magnetic field pulsed gradients in the z-direction of 50 G/cm. The NMR measurements of DPPE and conjugates were carried out in D2O at 30 °C and with water suppression using excitation sculpting with gradients [99]. Spectra were acquired and analyzed by using the standard Bruker software (version 4.01). NMR

analyses were performed at Laboratory of Structural Analysis, "Centro de Materiais da Universidade do Porto" (CEMUP) (Portugal).

2.5. Synthesis of Functionalized Solid Lipid Nanoparticles

2.5.1. Covalent binding method

The synthesis of SLN functionalized with DPPE-HA was performed by adding the conjugate to the lipid phase in a ratio of 1% w/w of the total formulation mass during the synthesis process.

2.5.2. Electrostatic interaction

HA-SLN were prepared using electrostatic attraction between the negatively charged HA and a cationic surfactant.

The nature of electrostatics interactions for surface modification of NPs presents a number of advantages over other methods such as covalent and hydrogen bonding. These interactions are reasonably strong and allow long-range binding, are isotropic and enable extension of the methodologies to biological templates [100]. Electrostatic interaction is a common approach for coating the NPs with HA due to the negative nature of HA polysaccharide [101-103].

The lipid NPs were synthesized by hot ultrasonication method as previously described (section 2.2.) with the same amount of each component, however using the positively charged hexadecyltrimethylammonium bromide (CTAB) molecule as a surfactant. Next, the NPs were coated with both HA 20-60 kDa and HA 1000-1800 kDa by adding equal volumes of a freshly prepared solution of each MW HA (at 2 mg/mL) to the nanoformulation with stirring for 4h. Aliquots were collected from the nanoformulations for the quantification of HA-coated NPs before and after incubation with the HA solution at room temperature.

2.6. Hyaluronic acid quantification assay

Cetyltrimethylammonium bromide turbidimetric method (CTM) was used for HA samples quantification.

Polyanionic polymers, like HA, are precipitated by organic ammonium cations such as CTAB. Quantification of the HA present in a given sample can be accomplished after reacting the sample with CTAB and subsequently reading the absorbance of the precipitate formed [104-107].

The amount of HA on the surface of HA-SLNs was quantified using the CTM as reported previously [108, 109]. Briefly, NPs were dissolved in dichloromethane at room temperature for 15 min. The free HA or HA conjugates were extracted from the organic phase using 0.8 mL sodium acetate solution (0.2 M). Sodium acetate solution was added to the organic solution, and the resultant

mixture was vortexed vigorously for 5 min and then centrifuged at 12,000 RPM for 5 min at 4 C. The HA content in the supernatant was further analyzed. A volume of 50 µL of HA standard solution (0.05-2 mg/mL) or HA sample was added to a 96-well plate. The solutions were incubated with the same volume of sodium acetate solution (0.2 M) for 10 min at 37˚C. Then, 100 µL of 10 mM cetyltrimethylammonium bromide solution was added to the mixture, and the absorbance of the precipitated complex was read after 10 min of co-incubation against the blank (100 µL sodium acetate solution with 100 µL cetyltrimethylammonium bromide solution) at 570 nm, using a microplate reader. The amount of HA to HA-SLN was then calculated by previously drawn standard curve of native HA . The slope of the standard curve was obtained by the linear regression for HA concentration range between 0.03 and 0.5 mg/mL, concentration over which the curve was no longer linear [110].

2.7. Characterization of Solid lipid nanoparticles

2.7.1. Dynamic Light Scattering

Dynamic light scattering (DLS), also known as photon correlation spectroscopy or quasi-elastic light scattering, is a precise technique for the measurement of particles size and Polydispersity Index (PDI). In this technique a laser beam goes through a suspension of particles and scattered light is collected in a detector. The Brownian random motion of the particles in a liquid causes time-dependent fluctuations in the intensity of the scattered light and information regarding particles diffusion coefficient can be obtained. The average hydrodynamic radius (dp), inversely proportional to the particles diffusion coefficients (D), is then estimated by the Stoke-Einstein relation (Equation 1) [111, 112].

(Equation 1)

$$D = \frac{kT}{3\pi\eta dp}$$

(**k**=Boltzmann constant, **T**=temperature, **η**=viscosity)

To determine the particle size accurately, the precise value of the liquid parameters temperature (T) and viscosity (η) must be known.

The mean effective diameter size and PDI of the synthesized formulations were determined using a Particle Size Analyzer (Brookhaven Instruments Corporation; Software: Particle Sizing v.5 Brookhaven Instruments; Holtsville, NY, USA) operating at a scattering angle of 90˚and at room temperature, with dust cut-off set to 30 and refractive index of 1.33. For each sample, 3 runs of 2 min each were performed. Before the measurements, non-lyophilized formulations were diluted in a ratio of 1:400.

2.7.2. Zeta Potential

Particles in a colloidal solution usually present an electrical double layer consisting of ions in solution that are attracted to particles by their surface charge. The formed bilayer is composed by an inner zone (stern layer) where the ions are tightly bonded to the particle surface and an outer region (diffuse layer) where ions are less strongly attached. The potential measured within the diffuse layer in a boundary in which the particle act as a single entity is called the zeta potential [113, 114]. Zeta potential defines the electrokinetic potential of particles in colloidal systems and is a measure of surface charge. It can influence particle stability as well as cellular uptake and intracellular trafficking [115]. Zeta potential is dependent on the composition of the NPs and is a function of the particle's environment, being affected not only by the properties of NPs, but also the nature of the solution, such as pH and ionic strength.

The zeta potential parameter allows to predict NPs stability and potential agglomeration within a dispersion. A high zeta potential (> ±40 mV) implies highly charged particles, which prevents aggregation due to electric repulsion, indicating that the system is highly stable. When zeta potential is low (< ±5 mV), attraction between particles will exceed repulsion and leads to aggregation due to van der Waals interactions A value of ±25 mV can be taken as the value that separates low-charged from high-charged surfaces [113, 116].

Electrophoretic light scattering (ELS) is an analytical method used for the measurement of the electrophoretic mobility of a suspension of particles and the working principle is similar to that of DLS. The sample is irradiated by a laser and scattered light is collected in a photodetector. In ELS, however, 2 electrodes are placed into the dispersion and an electric field of sufficient strength is applied so that electrokinetic behavior prevail random Brownian motion. According to the particles charge, migration occurs towards the oppositely charged electrode with a given velocity (mobility), which will promote fluctuations in the scattered light frequency. Frequencies are then converted to electrophoretic mobility, which is related with particles zeta potential by Henry equation [113, 117]. Henry's equation for the electrophoretic mobility μ of a spherical colloidal particle of radius a with a zeta potential ζ is expressed as the equation presented below.

(Equation 2)

$$\mu = \frac{\epsilon r \epsilon o}{\eta} \zeta f(\kappa a)$$

(**μ**=Electrophoretic mobility, **ϵ**=dielectric constant, **ζ**=zeta potential, **f(κa)**=Henry's function)

Zeta potential of each nanoformulation was determined using an electrode and Zeta Potential Analyzer (ZetaPALS, Brookhaven Instruments Corporation, Software: PALS Zeta Potential Analyser v.5, Brookhaven Instruments; Holtsville, NY, USA) operating at a scattering angle of 90° at room temperature. For each sample, 6 runs of 10 cycles each were performed. Before the measurements, non-lyophilized formulations were diluted in a ratio of 1:400.

2.7.3. Nanoparticle Tracking Analysis

Nanoparticle tracking analysis (NTA) is an innovative system developed for sizing particles from about 30 to 1000 nm, first commercialized in 2006 [118]. It is an analytical technique that combines laser light scattering microscopy with a charge-coupled device camera, for the visualization and recording of NPs in solution. The NTA software allows the visualization and tracking of individual NPs moving under Brownian motion and relates the movement to a particle size according to the following formula derived from the Stokes-Einstein Eq. (Equation 1).

NTA is a powerful tool for the measurement of size distribution of monodisperse and polydisperse samples. Due to the capability of visualization and tracking of individual particle it is possible to detect a broad range of population ratios whereby large particles don't compromise the accuracy of size grading [118].

Detailed NP size distribution was determined using NTA (NTA, NanoSight NS300, Malvern Instruments, Worcestershire, UK) equipped with a 488 nm laser and a high sensitivity scientific CMOS camera. Samples were diluted at a ratio of 1:100,000, injected using a 1 mL sterile syringe in the viewing chamber and measured under constant flow with an infusion rate of 50 at around 24°C. Size measurements were obtained based on a 20s video captured with a camera level of 10 and a detection threshold of 5. For each sample, 5 size measurements were conducted. Data were analyzed using the NTA 3.4. software.

2.7.4. Encapsulation Efficiency and Loading Capacity

The determination of MX encapsulation efficiency (EE) and loading capacity (LC) was determined by UV-vis spectrophotometry, by measuring the amount of drug that was not encapsulated.

Nanoformulations were diluted in PBS pH 8.2 in a ratio of 1:65 in a final volume of 2 mL. Formulations were centrifuged (Allegra X-15R Centrifuge, Beckman Coulter, Fullerton, California) in centrifugal filter units (Amicon® Ultra Centrifugal Filters Ultracell-50 kDa, MERK Milipore, Ltd; Cork, Ireland) at 3900 RPM for 30 min or until complete separation between SLN and the aqueous phase containing the free MX.

The amount of non-encapsulated MX present in the supernatant was quantified by UV-vis spectroscopy (Jasco V-660 Spectrophotometer, Software: Spectra Manager v.2, Jasco Corportation, USA) at 610 nm.

Prior to these measurements, a calibration curve of MX in PBS pH 8.2 with increasing known concentrations was acquired to determine the linear relationship between MX absorbance and concentration.

MX EE was then determined by calculating the difference between the initial amount of MX added to the SLN formulation and the amount of MX present in the supernatant, as shown by the following equation:

(Equation 3)

$$\mathrm{EE} = \frac{\text{Total amount of MX} - \text{Amount of MX in the supernatant}}{\text{Total amount of MX}}$$

The LC represents the amount of drug loaded per unit weight of the NP, indicating the percentage of mass of the NP corresponding to encapsulated drug. LC of MX was calculated per mass of lipid as follows:

(Equation 4)

$$\mathrm{LC} = \frac{\text{Total amount of MX} - \text{Amount of MX in the supernatant}}{\text{Total amount of lipid}}$$

2.7.5. Stability study

To evaluate the stability of the formulations over time, regular measurements of size, PDI, zeta potential, EE and LC were performed over a period of 4 weeks using the DLS and UV-vis spectroscopy characterization techniques previously described. Formulations were stored at 4°C over this period of time. The stability study was conducted in triplicate for each formulation to achieve statistical significance.

2.7.6. Mitoxantrone release assay

MX *in vitro* release from the functionalized loaded SLN (SLN DPPE-HA 20-60 kDa and SLN DPPE-HA 1000-1800 kDa) was investigated using a dialysis technique under sink conditions, as performed previously by Granja et al. [89]. The study was conducted at physiological buffer (pH 7.4) (PBS) and at pH 5.0 (acetate buffer), simulating the endosomal/lysosomal environment [119].

In this method, physical separation of the dosage forms is achieved by usage of a dialysis membrane (DM) which allows for ease of sampling at periodic intervals [120]. As with the other methods, several adaptations of the DM have been reported in literature with key differences in set-up, container size, and MWCO, being the dialysis bag (regular dialysis) the most commonly cited [120]. This study was performed using a Slide-A-Lyzer MINI Dialysis Devices, MWCO 10 kDa, 0.15 mL (Thermo Scientific™, MA, USA), relying on previously conducted release studies [121].

This dialysis model is carried out using a 15 mL centrifuge tube containing the release media (buffers) and a small container at the top carrying the nanoformulation. The small recipient contains the DMat its bottom enabling contact between the nanoformulation and the release media. Diffusion of the drug released from the NPs occurs through the DM into the outer compartment. Samples (1mL) are taken from the outer medium for analysis. A scheme summarizing the procedure is shown in Figure 6.

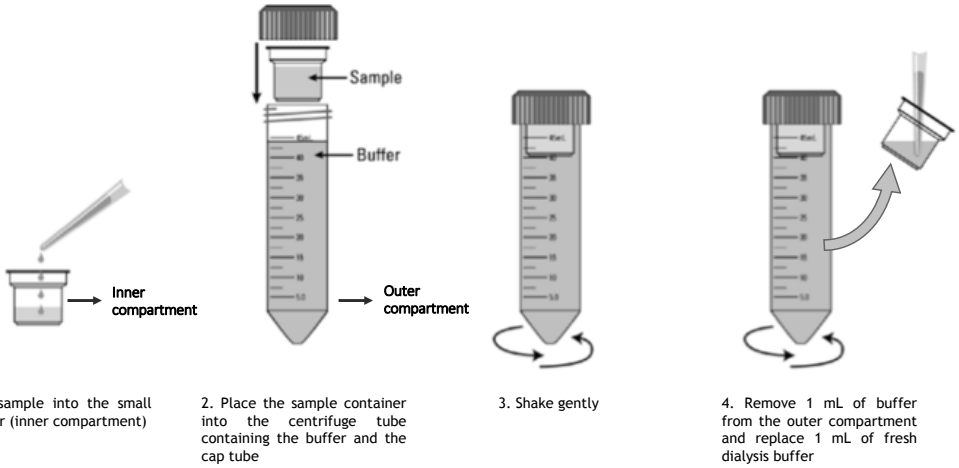


Figure 6 Release assay procedure scheme (Adapted from https://assets.thermofisher.com/TFS-Assets/LSG/manuals/MAN0011740_SlideALyzer_MINI_Dialy_Device_UG.pdf)

The experiment took 24 hours and aliquots from the outer compartment were collected over time. The time points used were 30 minutes following test initiation, 1h, 2h, 3h, 4h, 5h, 6h, 7h, 8h and 24h after. The nanoformulations were tested in triplicate for both PBS and sodium acetate solutions to achieve statistical significance. Free-drug sample was used as a positive control. The molecular weight cut-off of dialysis membranes was of 10 kDa, enough for drug diffusion to occur.

Briefly, this assay was carried out adding 500 µL of each drug-loaded SLN formulations in the upper container and filling the lower compartment of the tubes with the 14 mL of the correspondent buffer media. In order to mimic the release profile of SLN that circulate on the blood for a considerable period of time until reaching the tumor tissue, the centrifuge tubes were subsequently placed at 37˚C in an incubator shaker (ES-60, Lan Technics, USA) under gentle agitation (100 RPM). Then, at each time point 1 mL aliquots were collected for posterior reading absorbance and replaced by an equal amount of fresh fluid, so that the DM remains in contact with the buffer media. At last, MX released was quantified by UV-vis spectroscopy (Jasco V-660 Spectrophotometer, Software: Spectra Manager v.2, Jasco Corportation, USA) at 610 nm. Prior to this assay, calibration curves of MX in PBS pH 7.4 and acetate buffer pH 5.0 were obtained.

2.8. Cellular studies

2.8.1. Hemolysis assay

A hemolysis assay was performed to evaluate the hemolytic effect of the SLN by analyzing the release of hemoglobin, as an indicator of red blood cell (RBC) lysis following drug/NP exposure. Hemolysis represents the most commonly employed initial in vitro toxicity assessment [122].

For this assay, human blood samples from three distinct donors were obtained according to the principles of the declaration of Helsinki and were kindly donated by Serviço de Hematologia from Centro Hospitalar Universitário do Porto - Hospital de Santo António. (Porto, Portugal). Blood samples were collected in tubes containing EDTA as an anticoagulant just before use. Blood samples were centrifuged at 955 × g for 5 min at 4ºC and the resulting plasma fraction (supernatant) was removed from the sample. The pellets with the red blood cells (RBC) were then washed three times with an equal volume of physiological sterile saline solution (0.85%). After the last washing step, the resulting samples were diluted in saline solution to yield an RBC concentration of 4% (v/v).

The nanoformulations to be tested were prepared by serial dilutions in saline solution, with final concentrations ranging from 24 to 3 mg/mL

The positive and negative controls selected for the experiment were Triton-X-100 at a concentration of 1% (v/v) and saline solution 0.85%, respectively. The detergent Triton-X-100 is a commonly used hemolytic agent. Triton agents cause swelling followed by the hemolysis of erythrocytes and the rate of hemolysis increases with the increase in detergent concentration [123-126].

The assay was performed in a 96-well microplate (Kartell, Noviglio,Italy) loading each sample in triplicate. The final concentrations were obtained by adding 100 µL of each solution and controls to the wells, followed by 100 µL of RBCs to each well. The plate was sealed and incubated for one hour at 37˚C. After incubation, 25 µL of supernatant was carefully removed and transferred to 175 µL of saline solution to a 96-well plate to measure the absorbance of the hemoglobins at 415 nm using a microplate reader (Biotek Instruments, Winooski, VT, USA).

For the calculation of the percentage of hemolysis, control wells with 100 µL of each nanoformulation concentration and 100 µL of saline buffer (with no red blood cells) were prepared for background subtraction.

The percentage of hemolysis was calculated as follows:

(Equation 5)

$$Hemolysis\ \% = \frac{Abs\ (sample) - Abs\ (negative\ control)}{Abs\ (positive\ control) - Abs\ (negative\ control)} \times 100$$

2.8.2. Cell culture

Michigan Cancer Foundation-7 (MCF-7) cell line was acquired from ATCC (Middlesex, UK). MCF-7 were cultured at 37˚C in a 5% CO2 atmosphere (Unitherm CO2 Incubator 3503 Uniequip; Planegg, Germany) in Dulbecco's Modified Eagle Medium (DMEM) supplemented with 10% Fetal Bovine Serum (FBS) 1% Penicillin- Streptomycin (Pen-Strep). For every 2 to 3 days cells were washed twice with DPBS and the medium replaced by fresh supplemented DMEM. Cells were subcultured at 80 to 90% confluence by chemical detachment with 0.25% trypsin-EDTA followed by centrifugation at 300g for 5 min (Multifuge X1R, Thermo Fisher Scientific, USA) and re-suspension in fresh medium. Cell counting was performed in a Neubauer chamber (Improved Neubauer Bright-line, Boeco; Germany)

after addition of 90% (v/v) Trypan Blue solution (0.4% (w/v) in PBS) to exclude non-viable cells. Cells were seeded at a density of 750000 cells per 75 cm2 flasks (Tissue Culture flasks, Orange Scientific, Belgium) in 10 mL of supplemented DMEM.

2.8.3. MCF-7 cell viability assay

MCF-7 cell viability following incubation with the synthesized nanoformulations was measured by performing a resazurin assay.

The Resazurin assay is a fluorescent assay that detects cellular metabolic activity and is commonly used to monitor cells viability for up to 24-48 hours. The blue non-fluorescent resazurin reagent is reduced to highly fluorescent resorufin by dehydrogenase enzymes in metabolically active cells. That way, the amount of resorufin produced and its fluorescence is proportional to the number of metabolically active cells in the sample. The resorufin formed is quantified by measuring the relative fluorescence units (RFU) using a fluorometer [127, 128].

To perform this assay, MCF-7 cells were seeded onto 96-well tissue culture plates (Falcon®, Becton Dickson; England)) at a density of 1x104cells per well in 100 µL of supplemented DMEM and incubated for 24h at 37˚C, 5% CO2. Meanwhile the different formulations (SLN, SLN DPPE-HA 20-60 kDa, SLN DPPE-HA 1000-1800 kDa unloaded and MX loaded) and free-MX were diluted in DMEM to reach specific increasing concentrations: 0.01, 0.1, 1, 2, 11 and 21 (µg/mL of drug). After the incubation period, cells were treated with 100 µL each concentration of the 6 formulations and free MX and incubated for 4 h at 37˚C, 5% CO2. Positive control consisted of cells treated with only DMEM. A control media containing only DMEM was also included to correct for background fluorescence.

After 24 h, media was removed and replaced with 110 µL resazurin (10%v/v in DMEM) followed by incubation in the dark for 4 h at 37˚C, 5% CO2.

After the incubation period, the fluorescence of resorufin in the supernatant was measured using a fluorometer (Biotek Instruments, Winooski, VT, USA) (λex = 560 nm; λem = 590 nm). The dose-response curves and the values of IC_{50} of free drug and drug-loaded nanoformulations were obtained using GraphPad Prism Software (v.6.0, GraphPad Software, CA, USA).

Cell viability was calculated using the following equation:

(Equation 6)

$$Cell\ viability\ (\%) = \frac{Fluorescence\ of\ sample - Fluorescence\ of\ control\ media}{Fluorescence\ of\ positive\ control - Fluorescence\ of\ control\ media} \times 100$$

2.8.4. Confocal Laser Imaging

SLN internalization by MCF-7 cells was assessed by confocal laser imaging.

Confocal microscopy is a powerful tool that can create sharp images of a specimen with less haze and better contrast that that of a conventional microscope [129]. It captures a thin cross-section

of the specimen, excluding most of the light from the specimen that is not from the microscope's focal plane. The image in a confocal microscope is achieved by scanning one or more focused beams of light across the specimen. This point of illumination is brought to focus on the specimen by the objective lens. The sequences of points of light from the specimen are detected by a photomultiplier tube through a pinhole or slit, and the output from the PMT is built into an image and displayed by the computer. Although unstained specimens can be viewed using light reflected back from it, most of the times specimens are labeled with one or more fluorescent probes. The choice of fluorophores is the most important aspects of fluorescence, confocal microscopy because the fluorophores should tag the correct part of the specimen, be sensitive for the given excitation wavelength and the specimen should not affect the fluorophore, as its chemical environment can affect the position of the peaks of the excitation and emission spectra [129].

Weakly basic amines, such as DAMP and LysoTracker probes, can selectively accumulate in cellular compartments with low internal pH and are frequently used to label lysosomes. LysoTracker probes are popular fluorescent probes due to their high selectivity and effective lysosome labeling and are used at nanomolar concentrations [130, 131]. Widely used DNA-specific dyes are the 4′,6-diamidino-2-phenylindole (DAPI) and Hoechst, which emit blue fluorescence under ultraviolet illumination when bound to DNA [132, 133].

To perform this assay, MCF-7 cells were seeded onto µ-slide 8-well imaging plates (Ibitreat, Ibidi GmbH, Munich, Germany) at a density of $1x10^4$ cells per well in 300 µL of supplemented DMEM and incubated for 24 h at 37˚C, 5% CO2. After 24h, cells were treated with 100 µL of the 3 drug-loaded formulations and free MX at a concentration of 0.11 µg/mL (in DMEM) and incubated for 4 h and 24 h at 37˚C, 5% CO2. After the incubation periods, medium was discarded and cells were washed three times with PBS. After that, cells were stained with Lysotracker (60 nM in DMEM) and incubated for 30 min at 37˚C, 5% CO2. Cells were then washed three times with PBS and fixed with formalin solution for 30 min at room temperature [131]. After washing three times with PBS, cells' nucleus were stained with Hoechst (8 µM in PBS) for 10 min at room temperature protected from light followed by washing three times with PBS [134].

Images were recorded on a Leica Stellaris 8 confocal microscope (LeicaMicrosystems, Wetzlar, Germany) equipped with the Leica Application Suite X package (LAS X) using a λex/λem of 350/461 nm (Hoechst 33342®), λex/λem of 504/511 nm (LysoTracker™ Green) and λex/λem of 610/630 nm (MX) with a resolution of 1024×1024 using a 63X/1.4 oil immersion objective.

2.8.5. Cellular uptake quantification

Cellular uptake of uncoated and HA-coated LNs was quantified by flow cytometry.

The flow cytometer is a valuable instrument for investigations of cellular and molecular biochemistry and is used in various applications based on the detection of the membrane, cytoplasmic and nuclear antigens. The main benefit is the high-speed analysis of each particle, e.g. tens of thousands of cells can be analyzed in a second [135]. The underlying principle of flow cytometry

relies on light scattering and fluorescence emission, which occurs as light from an excitation source strikes particles moving in a fluid stream (Figure 7). Size, granularity and fluorescent features of the cells, derived from either antibodies or dyes, are parameters used to analyze and differentiate cells [136]. Thus, this technique allows the measurement of the optical and fluorescent characteristics of a single cell with the potential to identify carriers within cells and quantify the amount of cellular uptake.

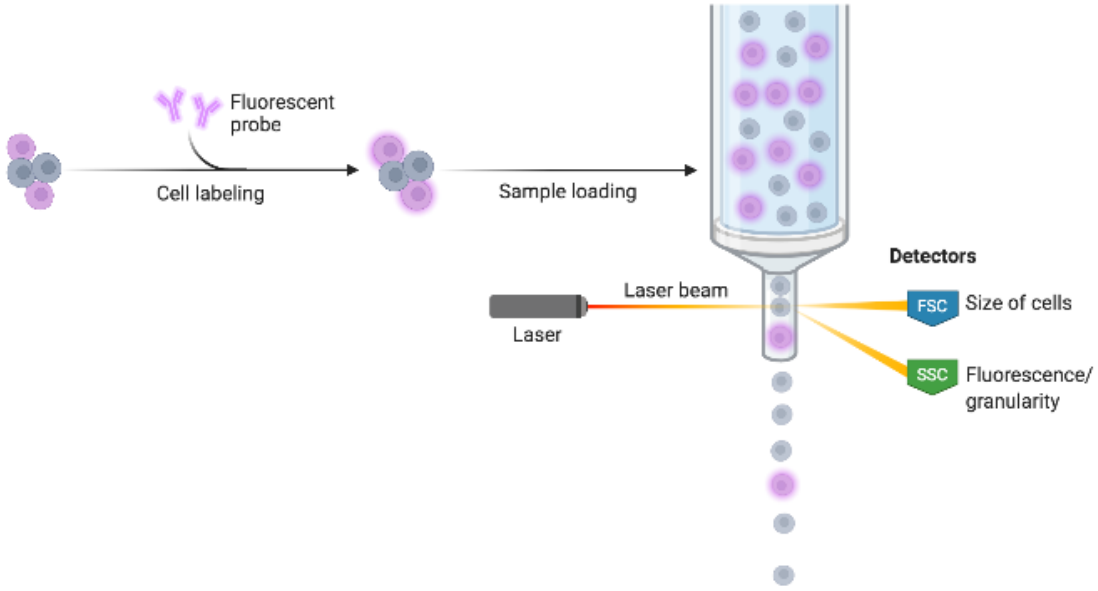


Figure 7 The underlying working principle of a flow cytometer

In this work, the uptake of coumarin-labeled lipid NPs was quantified based on the fluorescence intensity emitted by the fluorescent Coumarin 6 dye (C6), as previously described [137]. Coumarion 6 has been used as a hydrophobic fluorescent dye in NPs-based drug delivery studies, such as oral drug delivery systems for cancer [138, 139]. SLN were produced as reported in section 2.2., with addition of C6 (0.025%) in the lipid phase.

For quantification SLN uptake by MCF-7, the cells were seeded in a 24-well plate at a concentration of 2 × 105 cells per well and incubated for 24h at 37˚C, 5% CO2, before adding the NPs. Coumarin-labeled SLN were previously synthesized by hot ultrasonication as previously described (section 2.2.). C6 was added to the lipid phase in a ratio of 0.025 % w/w of the total formulation mass during the synthesis process. After 24h, cells were incubated with the C6-labeled SLN with and without HA at a concentration of 250 µg/mL in DMEM at two time points, 4h and 24h. Before flow cytometer analysis in a BD Accuri C6 (BD Biosciences, Erembodegem, Belgium), the cells were washed twice with PBS, recovered with trypsin-EDTA 0.25% (w/v), and resuspended in 150 µL of PBS. Dead cells were excluded with propidium iodide staining by adding 1.5 µL from a 1 mg mL−1 (in water) working solution. Trypan blue at 1 mg mL−1 was added to quench the C6 signal from the non-internalized SLN that were only adsorbed on the cell surface. At least 10,000 events were recorded for each sample.

2.9. Statistical analysis

Statistical analysis was performed using Graphpad Prism6 Software (GraphPad Software Inc., San Diego, CA, USA). Data were analyzed using one-way analysis of variance (ANOVA) with Dunnett's post-hoc test or two-way ANOVA using Tukey's test with a *p*-value <0.05 considered statistically significant. Data are expressed as mean ± SD.

Chapter 3 Results and Discussion

3.1. ^{1}H NMR characterization

HA of two different MW (20-60 and 1000-1800 kDa) was chosen to functionalize SLNs with the aim of improving the targeting ability towards CD44+ cancer cells [84]. To this end, conjugates of the phospholipid DPPE with low MW (20-60 LMW) and high MW (1000-1800 HMW) HA were synthesized with the aim of evaluating the influence of the HA molecular weight on breast cancer cell internalization.

Proton NMR spectroscopy was used to verify whether the covalent bond between DPPE and HA had been established upon synthesis of the two conjugates, prior to its coupling to the SLN. NMR spectroscopy has been considered to evaluate the conjugation of HA polymers to DPPE [96]. For this aim, firstly the ^{1}H NMR spectra of each component, HA and DPPE (Figure 8 A), have been recorded for the identification of the most characteristic resonance signals, as depicted in Figure 8 (A) and (B).

In the ^{1}H NMR spectrum of HA 20-60 (Figure 8 B) and HA 1000-1800 (Figure 8 C), it was possible to register three sets of signals: a, b and c (Figure 8 B, bottom and Figure 8 C, bottom, respectively), at 4.6-4.5, 3.8-3.4 and 2.0 ppm as previously reported by Gouveia et al. 2018. The spectra of the lipid revealed the characteristic signals at 1.6-1.2, 0.9 and 2.3-2.1 ppm, respectively assigned as d, e and f (Figure 8 B, middle). The data is in agreement with that previously described [96].

The spectra of the conjugate DPPE-HA 20-60 showed the signals correspondent to the DPPE component at 1.6-1.2, 0.9 and 2.2-2.1 ppm as well as those from HA, particularly the singlet at 2.0 and the low field peaks appearing between 3.8 and 3.4 ppm (Figure 8 B, up). The present of the two set of signals confirmed the conjugation of both components.

The analysis of the conjugate DPPE-HA 1000-1800 spectrum also confirmed the functionalization since both set of peaks from the polymer and the lipid are present. (Figure 8 C, up).

Globally, the NMR studies confirmed that the conjugation of HA and DPPE has been occurred and the suitability of the selected synthesis method.

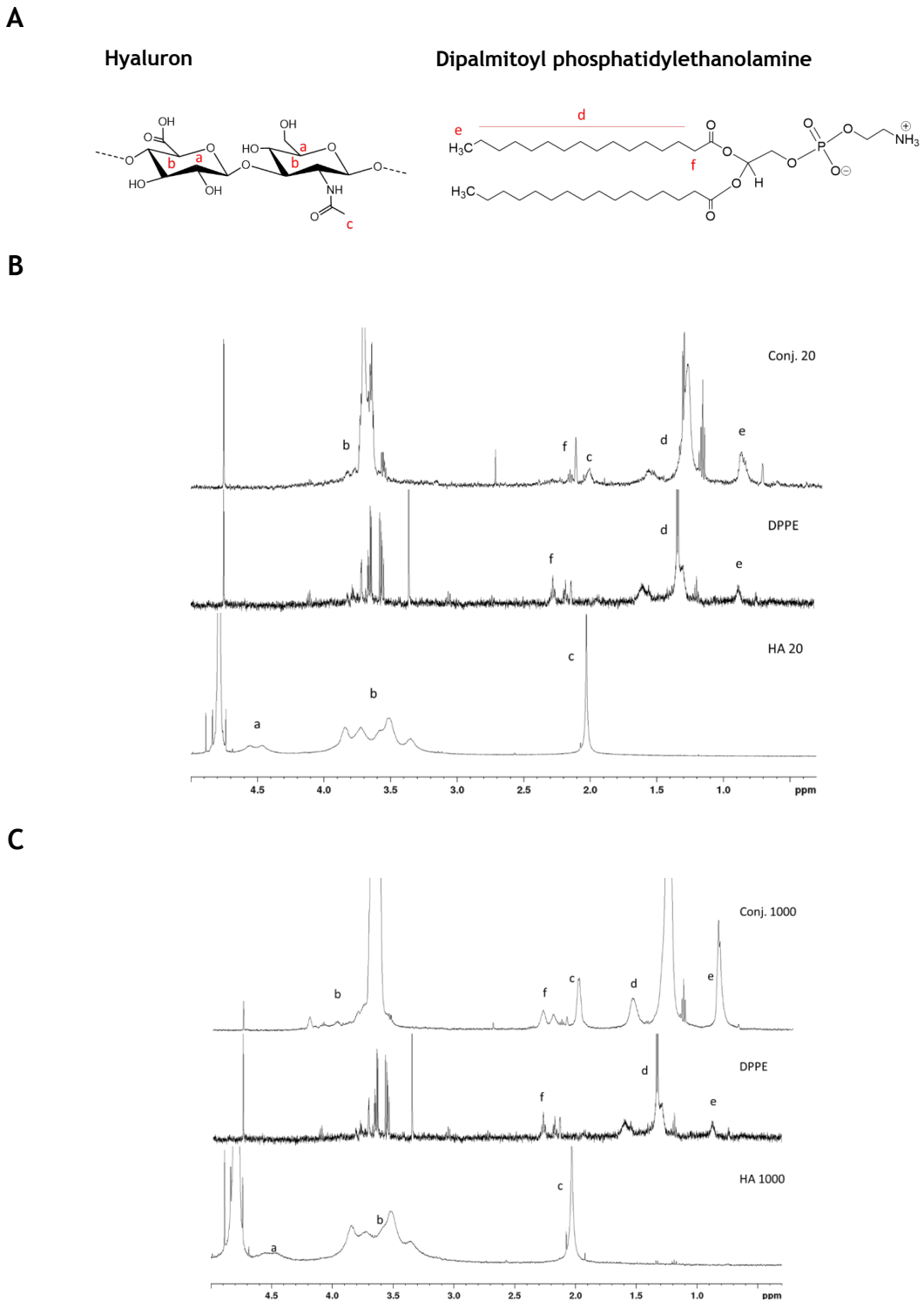


Figure 8 NMR analysis of DPPE-HA conjugate. (A) Formulae of HA (left) and DPPE (right), (B) NMR spectra of conjugate 20 (up) and their precursors DPPE (middle) and HA20 (bottom) and (C) NMR spectra of conjugate 1000 (up) and their precursors DPPE (middle) and HA 1000 (bottom)

3.2. Nanoparticle functionalization with Hyaluronic acid: electrostatic interaction versus conjugate

SLN functionalized with HA 20-60 and HA 1000-1800 were synthesized by the hot ultrasonication technique, a cost-effective preparation method with the advantage of avoiding the use of organic solvents that lead to potential toxic contamination as well as pose a potential hazard to the atmosphere [140, 141].

The functionalization of SLN with HA was developed using two different approaches: electrostatic interaction between the negatively charged polysaccharide and cationic CTAB or by addition of the previously synthesized DPPE-HA conjugate in the lipid matrix. The HA coated formulations obtained by the two methods were compared to select the most feasible one.

Thus, four different formulations were produced and further analyzed concerning their physicochemical properties, long-term stability and hemolytic activity: the SLN CTAB HA 20-60, SLN CTAB 1000-1800, SLN DPPE-HA 20-60 and SLN DPPE-HA 1000-1800.

All the formulations appeared milky and homogeneous with absence of precipitates.

3.2.1 Physicochemical characterization

The produced nanoformulations were characterized in terms of size, PDI and zeta potential by DLS as shown in Table 2.

The NPs produced using both functionalization approaches (SLN-CTAB and SLN DPPE-HA) presented sizes between 190 and 220 nm and therefore are suitable for intravenous administration and should benefit passive tumor accumulation through EPR effect [142-144]. It is also noticeable that the use of both methods, did not significantly affect the size of the NPs.

Regarding SLN PDI, this remained at values oscillating at 0.2 or below, pointing to the presence of a homogeneous population of NPs, with acceptable monodispersity [145].

Zeta potential of SLN-CTAB formulations is highly positive, which reflects the cationic surfactant in their structure. The results of comparative analysis of zeta potentials before and after HA coating showed that the positive surface charge (53±3 mV for HA 20-60 and 60±8 mV for HA 1000-1800) of SLN had changed to less positive charge (28±7 mV and 14±4) after HA coating (data not shown), because of the negatively charged carboxylic acid groups in their structure. This change in surface charge of SLN-CTAB HA particles shows the bound of HA molecules to their surface, however, the zeta potential had not changed to negative values as previously observed by Lee *et al*. [101].

The SLN DPPE-HA particles, on the other hand, exhibit neutral zeta potentials in general. This was expected given the salt complexity of the solvent used and the use of a non-ionic surfactant as Tween 80, in contrast with the cationic surfactant CTAB [146, 147]. Although NPs with low zeta potential are less stable in suspension [116], due to more tendency to aggregate, this may be is an advantage *in vivo* as it can prolong the nanocarriers circulation time by protecting them from opsonization and consequent elimination RES [44]. No statistically significant differences were found in terms of zeta potential between the SLN functionalized with the different HA MW.

Table 2 Physicochemical characterization of the HA functionalized SLN formulations by DLS: size, PDI, zeta potential. Values represent mean ± SD (n=3); [a]p < 0.05, relatively to the HA 20-60 formulation (SLN CTAB HA 20-60)

	CTAB HA 20-60	CTAB HA 1000-1800	DPPE-HA 20-60	DPPE-HA 1000-1800
Size (nm)	205 ± 17	210 ± 16	198 ± 6	211 ± 8
PDI	0.21 ± 0.02	0.22 ± 0.02	0.16 ± 0.02	0.19 ± 0.02
Zeta potential (mV)	28 ± 7	14 ± 4 [a]	-6 ± 6	2 ± 14

3.2.2 Stability studies

The physical stability of both SLN-CTAB and SLN DPPE-HA nanoformulations upon storage was evaluated over a period of 4 weeks. SLN were stored at 4°C and periodic measurements of the particle size, PDI and zeta potential were performed.

The stability of size and PDI over the 4 weeks is shown in Figure 9. On the left, SLN CTAB-HA NPs show to remain stable over the time, regarding both their size and polydispersity. In turn, after 4 weeks, SLN DPPE-HA show a small increase in size and PDI when compared to the day 0, corresponding to the day NPs were produced. These results suggest that, after 1 month of storage, the particles functionalized with the conjugate might suffer a rearrangement in their structure leading to changes in their physicochemical properties. Nevertheless, particle size is still adequate for intravenous administration and the values of PDI are below 0.3, which is an acceptable value and indicator of a homogeneous population for lipid-based NPs [145].

Regarding the zeta potential, it remains positive for SLN CTAB NPs over time and neutral for SLN DPPE-HA, with no significant differences throughout the storage time of the particles, as shown in Figure 10.

Overall, in terms of physicochemical properties, the nanoformulations synthesized appear to be stable for at least 1 month. According to the literature, functionalization of NPs by covalent conjugation is considered a better-established method and ensures more stable bonds [101]. Analysis over an extended time frame would be important to assess the consistency on particles stability and accuracy of these results.

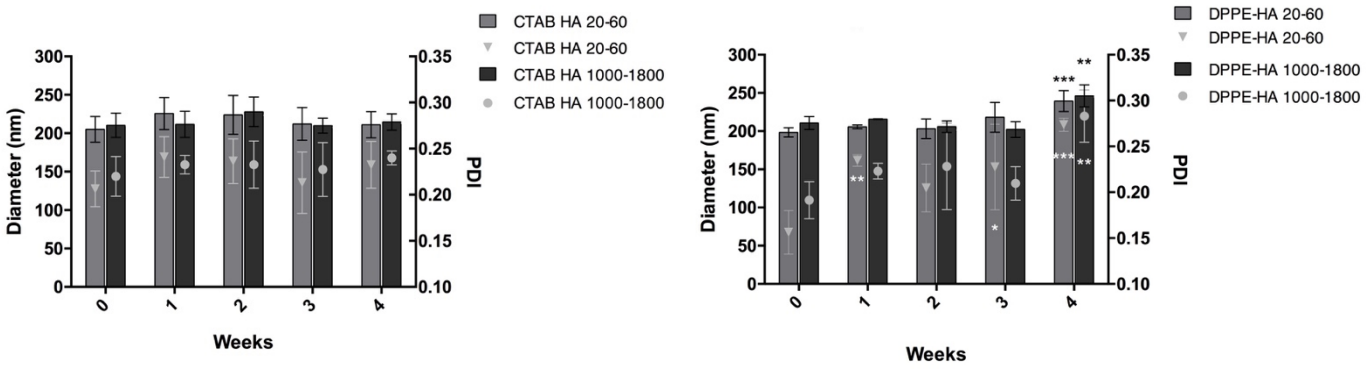


Figure 9 Effect of storage time on size and PDI of the SLN formulations. Bars represent size (left Y axis) and symbols the PDI (right Y axis). Values represent the mean ± SD (n=3); *p<0.05, relatively to the correspondent NPs at week 0

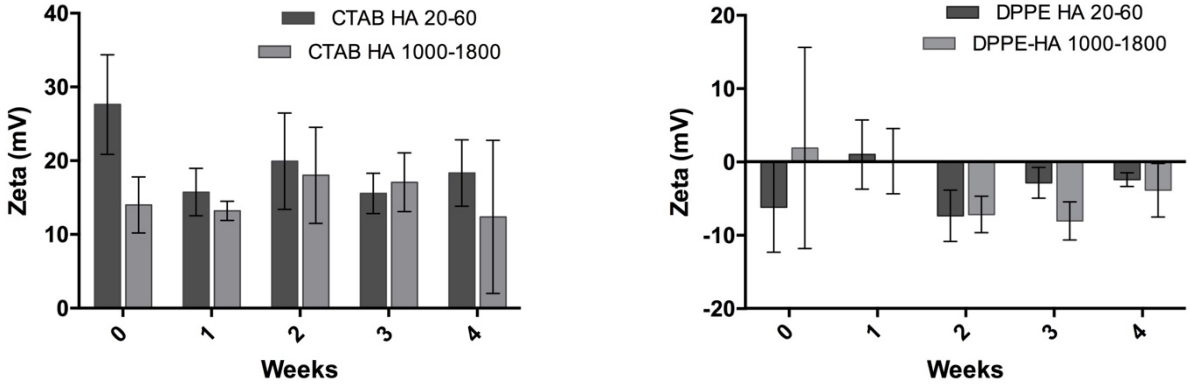


Figure 10 Effect of time of storage on zeta potential of SLN nanoformulations functionalized by electrostatic interaction (CTAB HA) and with DPPE-HA conjugate (DPPE-HA). Values represent the mean ± SD (n=3)

3.2.3 Hemolysis *in vitro* assay

The hemolytic effect of SLN-CTAB HA and SLN DPPE-HA formulations was evaluated to assess, at first, their toxicity to RBC. According to ISO 10993-4 (Standard, 2017), if the SLN causes hemolysis greater than 5%, then the nanoformulation is toxic and no longer safe and suitable to be administered intravenously [148].

The Figure 11 shows the pictures taken to the 96-wells plate at the end of the hemolysis assay, after blood samples incubation with the controls and the different concentrations of NPs formulations. By analyzing the blood samples incubated with the nanoformulations shown in Figure 11 (A) and (C), it is possible to conclude that the SLN-CTAB formulations show hemolytic effect on blood samples for all concentrations tested, by the turbidity appearance of the wells (Figure 11 (A), row a-d, columns of CTAB; Figure 11 (C), wells with CTAB). On the contrary, all concentration SLN DPPE-HA formulations resulted in RBC deposition at the bottom of the wells (Figure 11 (A), rows a-d, columns DPPE-HA; Figure 11 (C), wells DPPE-HA)

The % of hemolysis caused by SLN in concentrations ranging from 3 to 24 mg/mL of lipid after incubation for 1h is shown in Figure 12. The two SLN-CTAB preparations show high values of hemolysis that exceed 50%, for all concentration tested, whereas SLN DPPE-HA NPs exhibit no hemolytic activity. The toxicity observed must be strongly determined by the positive charge of the particles with CTAB in its constitution, which results in interaction with the biological membranes, leading to their disruption [149]. The SLN DPPE-HA with neutral zeta potentials did not show any hemolytic effect over RBC. In addition, there is no significant difference in hemolytic effect comparing CTAB SLN with different MW HA.

These findings support that the developed SLN DPPE-HA are non-toxic and safe for intravenous administration, and the exclusion of NPs formulated with CTAB for drug delivery purposes.

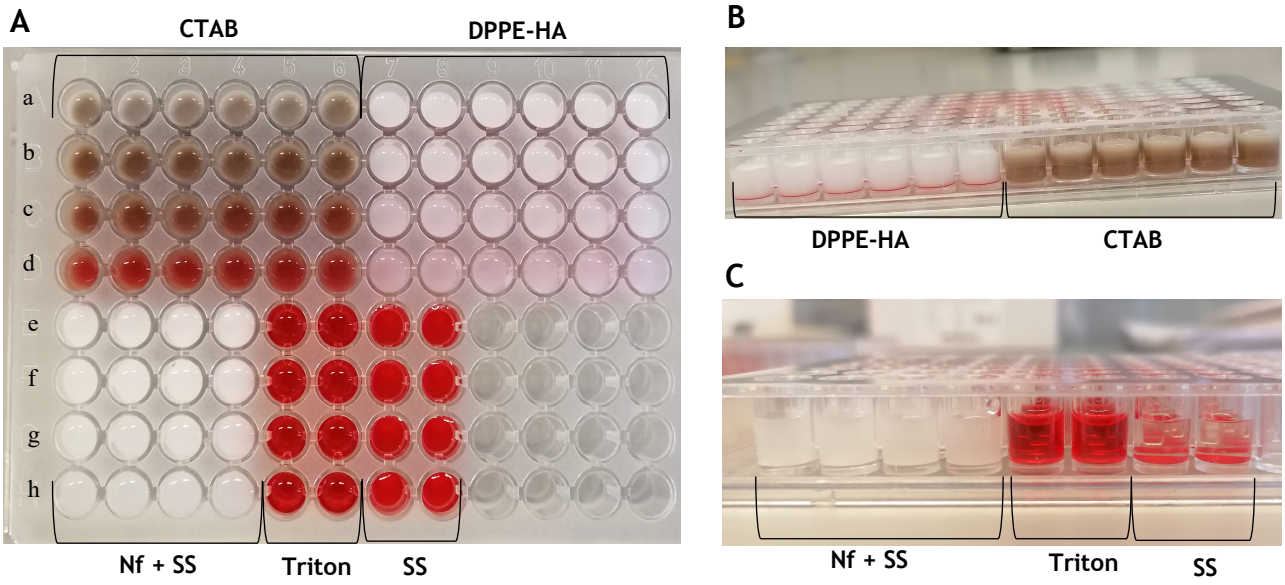


Figure 11 96-wells plate picture after hemolysis assay. (A) shows the blood samples that were incubated with decreasing concentrations (a-d) of SLN-CTAB HA (CTAB) and SLN DPPE-HA (DPPE-HA) and, below these (e-h), nanoformulation (Nf) crescent concentrations with only saline buffer (SS), with no red blood cells, used for background subtraction and the blood samples incubated with Triton-X-100 positive control and the negative control consisting of saline solution. (B) shows the blood cell samples after incubation with the nanoparticles SLN DPPE-HA (left) and the blood samples incubated with CTAB nanoformulation (right) for one concentration of nanoparticles. (C) shows that the Triton caused RBC disruption leading to a red diluted solution, contrasting the deposition of the RBC at the bottom of the wells

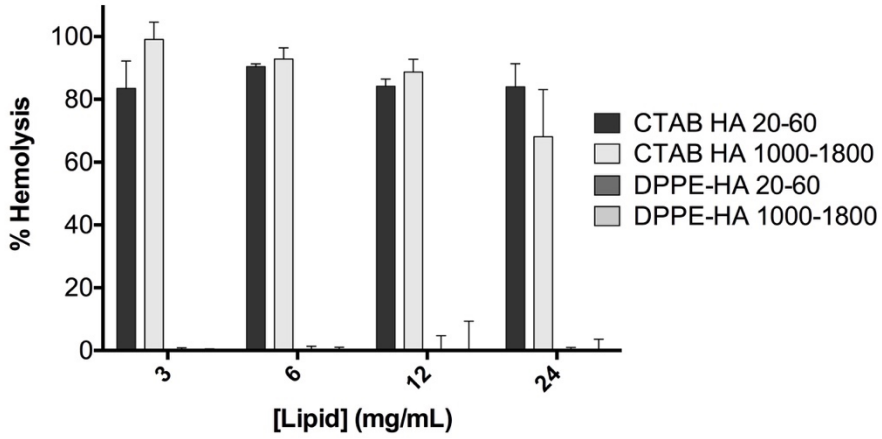


Figure 12 *In vitro* hemolysis assay results for diluted human blood exposed to different concentrations (3, 6 12, 24 mg/mL) of functionalized SLN-CTAB and SLN DPPE-HA. Values represent mean ± SD (n=3)

3.2.4 Hyaluronic acid quantification

HA was quantified in SLN CTAB HA 1000-1800 nanoformulation to verify the binding between HA and the SLN. The CTAB turbidimetric method was selected to quantify the amount of HA that effectively remained associated with the NPs. This method was demonstrated to be more accurate, sensitive and specific than the conventional approach to quantify HA, the carbazole method. On the other hand, CTM allows direct HA quantification in samples [107].

Prior to CTM assay, a calibration curve for HA 1000-1800 at PBS pH 8.2 was performed with a concentration range of HA from 0 to 2 mg/mL (Figure 13).

Thereafter, the absorbance of the samples turbidity induced by HA/CTAB precipitate was measured and the concentration of HA calculated and then compared to those used upon particle functionalization. The absorbance values of the samples were close to the control, which means that no HA could be detected, for all the different concentration HA solutions tested. The nanoformulations were incubated with different HA concentration solutions, experimenting several incubation times. In any case, no significant amounts of HA could be detected. This might be related to a lack of sensitivity for the detection of HA concentrations at the mg/ml level [107].

This method was also used to quantify the HA loss at the time of conjugate synthesis, before and after the first washing step, demonstrating that only a limited amount of HA was lost during the purification steps.

Many studies fail to quantify the amount of HA that was effectively bound to the NPs, a key factor to consider when HA is used as a ligand in targeting strategies. Thus, it would be of great interest to explore assays for quantifying HA with higher sensitivity.

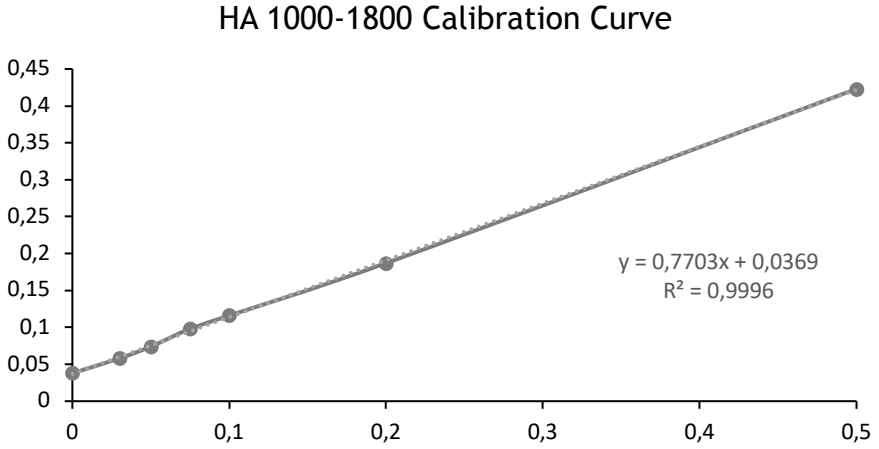


Figure 13 Calibration curve of HA 1000-1800 in PBS pH 8.2. Linear regression was drawn and the correlation coefficient (R2) calculated. Linearity of the standard curve and a satisfactory R2 value was observed at the range of concentrations from 0 to 0.5 mg/mL. For highest HA concentrations the standard curve no longer showed a good linearity. The lack of linearity observed beyond 0.5 mg/mL can be due to a poor mixing efficiency caused by increase of sample viscosity at high HA concentration, as observed previously by Oueslati et. al. [107].

3.3 Production of mitoxantrone-loaded solid lipid nanoparticles

After the recognition of the non-toxicity and promising features of the SLN functionalized with the conjugate, SLN DPPE-HA loaded with the drug MX were produced by the same method and using the same amounts of constituents, but with the prior addition of MX to the aqueous phase.

The obtained formulation presented a homogeneous bluish color, contrasting the milky appearance of the uncoated formulations.

The properties of the formulations prepared with and without MX were compared throughout this study to assess the influence of MX on their constitution and their suitability for drug loading and subsequent uptake and delivery to the target site.

The method used is very promising, as it avoids the use of organic solvents, thus ensuring its safety. On the other hand, it is cost effective and allows for a subsequent scale-up [52, 53, 58].

3.3.1 Physicochemical characterization

To evaluate if drug incorporation into SLN influenced their physicochemical characteristics, the produced SLN DPPE-HA MX loaded nanoformulations were characterized in terms of size, PDI and zeta potential by DLS and these findings are reported in the Table 3, together with the data previously obtained for the physicochemical features of SLN DPPE-HA particles alone (from section 2.2.1.).

The loading of MX into SLN DPPE-HA NPs did not have significant influence on their hydrodynamic diameter. Also, no significant differences occurred between the mean sizes measured by DLS for MX DPPE-HA 20-60 and MX DPPE-HA 1000-1800. As for the PDI values, these again point to a homogeneous population of NPs. Furthermore, no statistically significant differences were found in terms of zeta potential between MX-loaded and functionalized SLN comparing to the correspondent placebos, which indicates that the loading do not interfere with particles stability.

As a complement, the SLN DPPE-HA loaded and unloaded were analyzed by the NTA technique, which enables sample visualization and provides information on the mean size values, mode of the particle dispersions and particle concentrations. These results are presented in Table 4, alongside the values obtained by DLS.

It is observable a difference in the average size of the NPs measured using DLS or NTA. SLN DPPE-HA mean diameters of NPs measured by DLS are between 190 and 220 nm, whereas NTA show a mean particle size of around 144 nm for all nanoformulations.

As a single particle analysis method with high resolution, NTA has the advantage over DLS of being able to detect both large and small particles providing a more accurate particle distribution. On the contrary, since in a polydisperse system the large particles scatter more light than smaller ones, the dynamic light scattering technique may underestimate the proportion of small particles in the system [150]. This explains the difference in sizes obtained using DLS and NTA, as shown in Table 4.

Histogram of size distribution (size vs. particles concentration) of SLN DPPE-HA 20-60 and SLN DPPE-HA 1000-1800 from NTA measurements with the corresponding NTA video frame can be found in Figure 14.

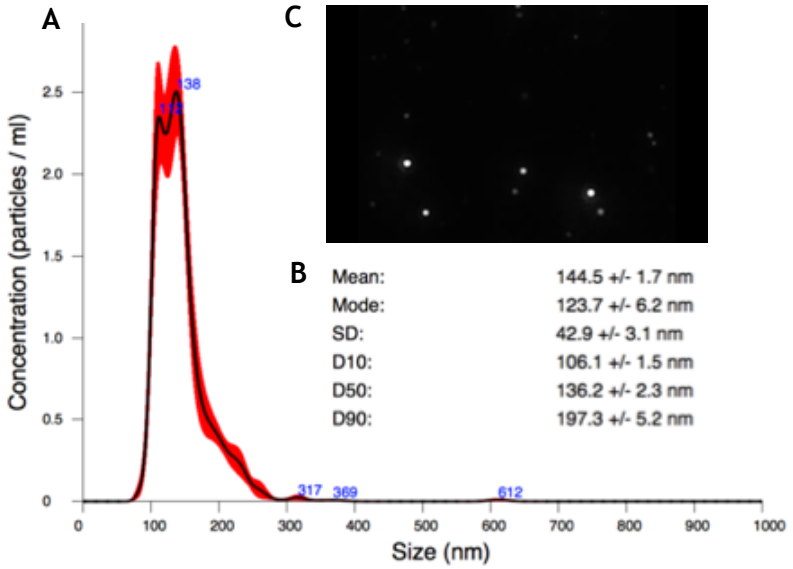
Table 3 Physicochemical characterization of the SLN formulations functionalized with the conjugate, unloaded (DPPE-HA 20-60 and DPPE-HA 1000-1800) and loaded with MX (MX DPPE-HA 20-60 and DPPE-HA 1000-1800): size, PDI, zeta potential, EE and LC. Values represent mean ± SD (n=3)

	DPPE-HA 20-60	DPPE-HA 1000-1800	MX DPPE-HA 20-60	MX DPPE-HA 1000-1800
Size (nm)	198 ± 6	211 ± 8	198 ± 5	220 ± 12
PDI	0.16 ± 0.02	0.19 ± 0.02	0.16 ± 0.02	0.21 ± 0.04
Zeta potential (mV)	-6 ± 6	2 ± 14	-3 ± 13	-3 ± 6
EE (%)	N/A	N/A	100 ± 1	88 ± 10
LC (%)	N/A	N/A	2.14 ± 0.02	1.90 ± 0.22

Table 4 Mean Size and Size Distribution of HA 20-60 and HA 1000-1800 functionalized SLN (DPPE-HA 20-60 and DPPE-HA 1000-1800, respectively) from DLS and NTS Measurements. Mean size (Mean); Polydispersity index (PDI); Standard deviation (SD) calculated by the NTA software; Concentration in hundred million (E8) particles/ml as measured by NTA. Values represent mean ± SD (n=3).

	DLS		NTA		
	Mean (nm)	**PDI**	**Mean (nm)**	**SD (nm)**	**Particles Concentration (E8/mL)**
DPPE-HA 20-60	198 ± 6	0.16 ± 0.02	145 ± 2	43 ± 3	1.74
DPPE-HA 1000-1800	211 ± 8	0.19 ± 0.02	143 ± 2	45 ± 3	1.88
MX DPPE-HA 20-60	198 ± 5	0.16 ± 0.02	141± 2	42 ± 5	2.09
MX DPPE-HA 1000-1800	220 ± 12	0.21 ± 0.04	142 ± 1	44 ± 3	1.96

SLN DPPE-HA 20-26



SLN DPPE-HA 1000-1800

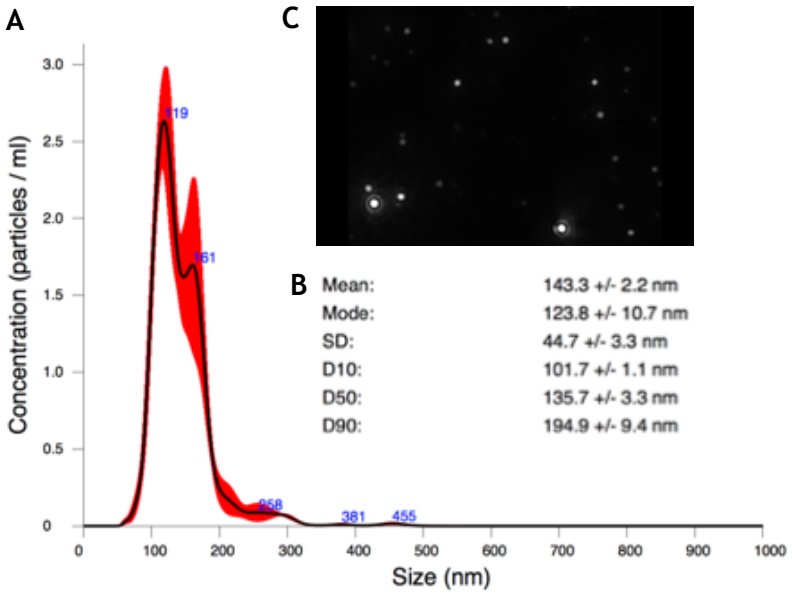


Figure 14 NTA analysis of SLN DPPE-HA 20-60. Size distribution profile data. (A) Histogram of size distribution (size vs. particles concentration), with the size of the key peaks annotated. (B) Mean, mode and size distribution (SD) ± SEM (standard error of the mean) data (C) Visualization of the NPs flow during NTA measurements.

3.3.2 Encapsulation efficiency and loading capacity determination

The EE and LC of MX-SLN was determined by UV-vis spectrophotometry.

As shown in Table 5, high values of EE and LC (>88%) were obtained for both HA MW loaded SLN, with no statistically significant differences between the particles functionalized with the HA 20-60 and HA 1000-1800, which leads to conclude that the molecular weight of the ligand has no interference on the ability of NPs to internalize the drug.

Table 5 EE and LC measurements of the MX-loaded nanoformulations. Values represent mean ± SD (n=3)

	MX DPPE-HA 20-60	**MX DPPE-HA 1000-1800**
EE (%)	100 ± 1	88 ± 10
LC (%)	2.14 ± 0.02	1.90 ± 0.22

3.3.3 Stability studies

The storage stability of MX loaded SLN was evaluated concurrently with the stability of SLN alone over 4 weeks, as previously mentioned.

The periodic assessment of the NPs physiochemical properties is presented in the Figure 15. As shown in Figure 15 A, in the overall, particle sizes of loaded SLN DPPE-HA remained stable during the 4 weeks of study. In terms of PDI, it is observed a variation in the course of time, however, PDI values remain acceptable (< 0.3) and indicator of a homogeneous population among MX loaded NPs (Figure 15 B) [145]. The zeta potential remains neutral over the course of the assay, as seen for the unloaded SLN DPPE-HA (Figure 15 C).

In addition to zeta and PDI measurements for 4 weeks, the percentage of EE of SLN was also assessed during one month in order to verify whether the NPs lose MX during their storage period. As shown in Figure 15 D, MX DPPE-HA 20-60 exhibit statistically significant decrease in terms of MX EE compared to the day 0 of the formulation whereas MX DPPE-HA 1000-1800 show a less accentuated decrease in EE. Nevertheless, after 1 month of storage, both nanoformulations show a high value of EE of more than 75%.

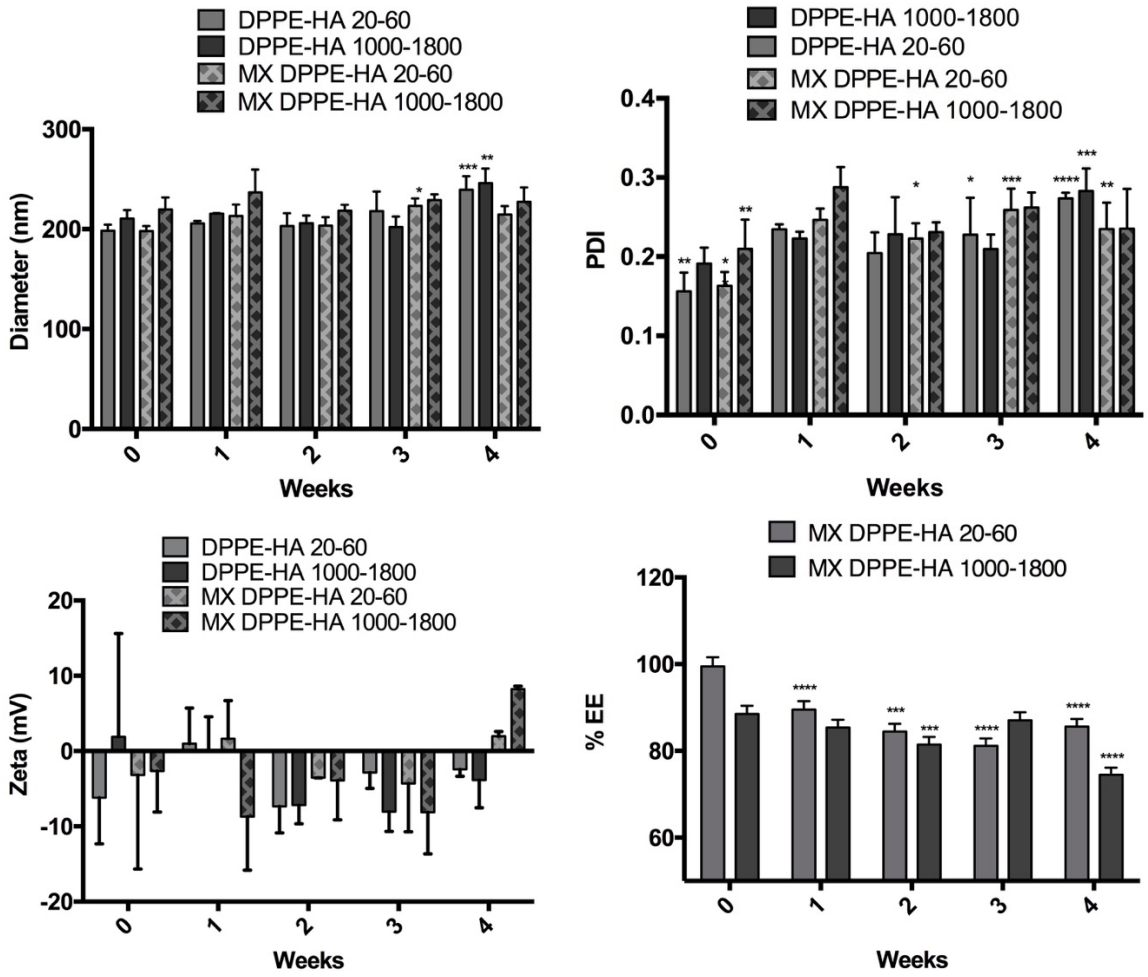


Figure 15 Effect of time storage on size (A), PDI (B), zeta potential (C) and EE (D) of SLN DPPE-HA nanoformulations unloaded (DPPE-HA) and MX-loaded (MX DPPE-HA). Values represent the mean ± SD (n=3); *p<0.05, **p<0.01, ***p<0.001, ****<0.0001. All statistically significant differences are related to the values of the correspondent nanoparticles at week 0

3.3.4 Release assay

The MX release from the functionalized MX-loaded SLN was performed based in a dialysis technique at pH 7.4 and pH 5, in order to simulate the physiological environment and the endosomal compartment, respectively [151].

This method allowed the comparison of the cumulative percentage release of MX for both pH conditions and between LMW and HMW HA functionalized SLN over 24 hours, as shown in Figure 16.

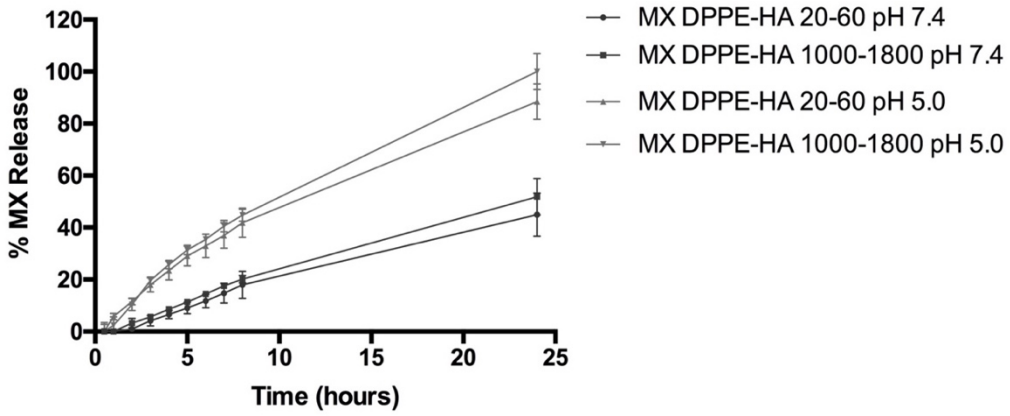


Figure 16 In vitro MX release profile from drug-loaded SLN functionalized either with HA 20-60 and HA 1000-1800 in simulated physiologic (pH=7.4) and endosomal (pH=5) fluids. Values represent mean ± SD (n=3)

At pH 7.4, only 20% of MX was released from the NPs after 8h, and roughly 50% of the drug remained encapsulated by the end of the 24h. The percentage of MX release at pH 5 shows a much faster drug liberation, with more than double the release after 8h and total drug release from the SLN DPPE-HA 1000-1800 at the end of the assay. The results point to a controlled release by the SLN in physiological environment, such as bloodstream and other body tissues media and a much faster release upon acidic endosomal environment.

Regarding the DPPE-HA different molecular weights used, a similar release profile is observed among the two types of SLN, suggesting that the functionalization has no impact on the mechanism of drug release from the particles.

The results of this study encourage intravenous delivery of NPs that will presumably sustain MX encapsulation while in the bloodstream and then promote pH acid triggered release after internalization of the particles via endocytosis as predicted after CD44-HA interaction.

3.4 Cellular studies

3.4.1 Hemolytic effect of Mitoxantrone-loaded SLN

The RBC toxicity of SLN loaded with MX was also assessed *in vitro* at the same conditions previously described for SLN CTAB and SLN DPPE-HA formulations. As for SLN alone, the hemolytic activity was null for all concentrations tested (Figure 17). These findings support that the developed SLN DPPE-HA formulations are non-toxic according to ISO 10993-4 (Standard, 2017) and, therefore are not hazardous as drug carrier administered intravenously.

The pictures taken to the result of the hemolysis assay for the particles containing MX are in Figure 18 and are consistent with the results observed for the uploaded SLN DPPE-HA NPs described above (Section 2.2.3.).

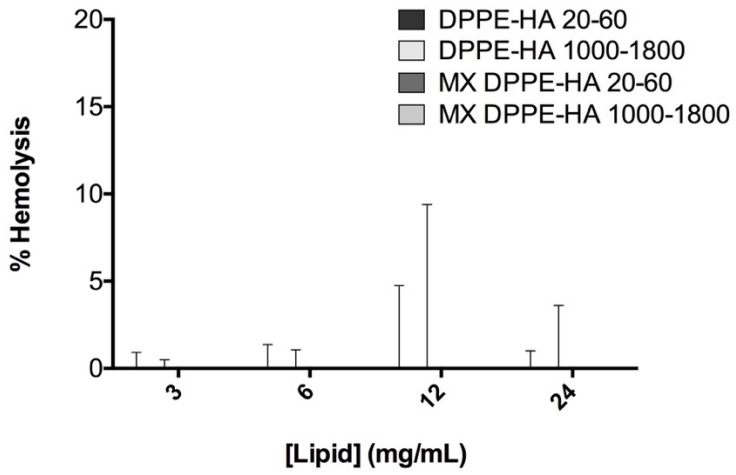


Figure 17 *In vitro* hemolysis assay results for diluted human blood exposed to different concentrations (3, 6 12, 24 mg/mL) of MX-loaded SLN DPPE-HA formulations. Values represent mean ± SD (n=3)

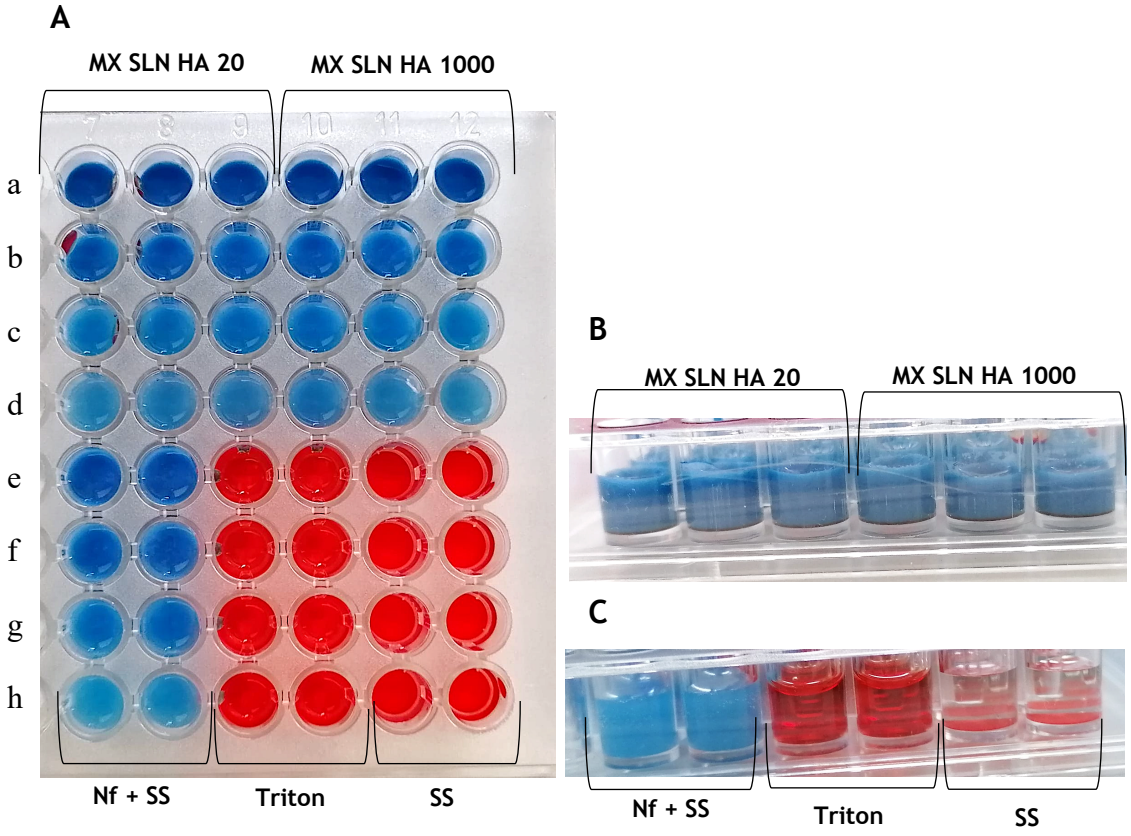


Figure 18 96-wells plate picture after hemolysis assay. (A) shows the blood samples that were incubated with decreasing concentrations (a-d) of MX-loaded SLN functionalized with DPPE-HA 20-60 kDa and 1000-1800 kDa and, below these (e-h), nanoformulation (Nf) crescent concentrations with only saline buffer (SS), with no red blood cells, used for background subtraction and the blood samples incubated with Triton-X-100 positive control and the negative control consisting of saline solution. (B) shows the blood cell samples after incubation with the nanoparticles MX-loaded SLN DPPE-HA 20 (left) and with MX-loaded SLN DPPE-HA 1000 (right), for one concentration of nanoparticles. (C) shows that the Triton caused RBC disruption leading to a red diluted solution, contrasting the deposition of the RBC at the bottom of the wells

3.4.2. Solid Lipid Nanoparticles cellular toxicity

In this work, the cytotoxicity induced by SLN DPPE-HA-MX was evaluated in MCF-7 breast cancer cell line using the Resazurin assay.

The MCF-7 cell line was chosen as being CD44+, for the study of the HA-conjugated particles interaction with its receptor in breast cancer cells and their cytocompatibility.

After incubation of the cells with NPs for 24h, the % of cell viability was calculated as being directly proportional to the amount of resorufin fluorescence produced by metabolically active cells. As shown in figure 19 A, SLN unloaded formulations are non-toxic (<70%) up to a very high concentration of lipid (500 µg/mL) according ISO 10993-5 [152]. No statistically significant differences were observed in terms of cell viability reduction caused by functionalization of SLN. This suggest that both the lipid vehicle and the HA conjugates have a high biocompatibility.

Assessment of the viability of MCF-7 cells incubated for 24h with the MX-loaded NPs is presented in Figure 20. Data shows that NPs induced a reduction in cell viability comparable to that of the free drug, proving their efficacy. This can be observed for concentrations as low as 1 µg/mL of drug (corresponding to 50 µg/mL of lipid). The results of cell viability were then used to plot dose-response curves (Figure 21) to determine the values of IC_{50}. The values obtained were 1.3 µg/mL for SLN, 1.7 µg/mL for SLN HA 20-60, 0.96 µg/mL for SLN HA 1000-1800 and 1.4 µg/mL for free MX. These results further support that the NPs could induced similar anti-cancer effects than the free drug. In fact, these results were found to be optimal and concordant with studies performed with MC7-7 under the same conditions [153].

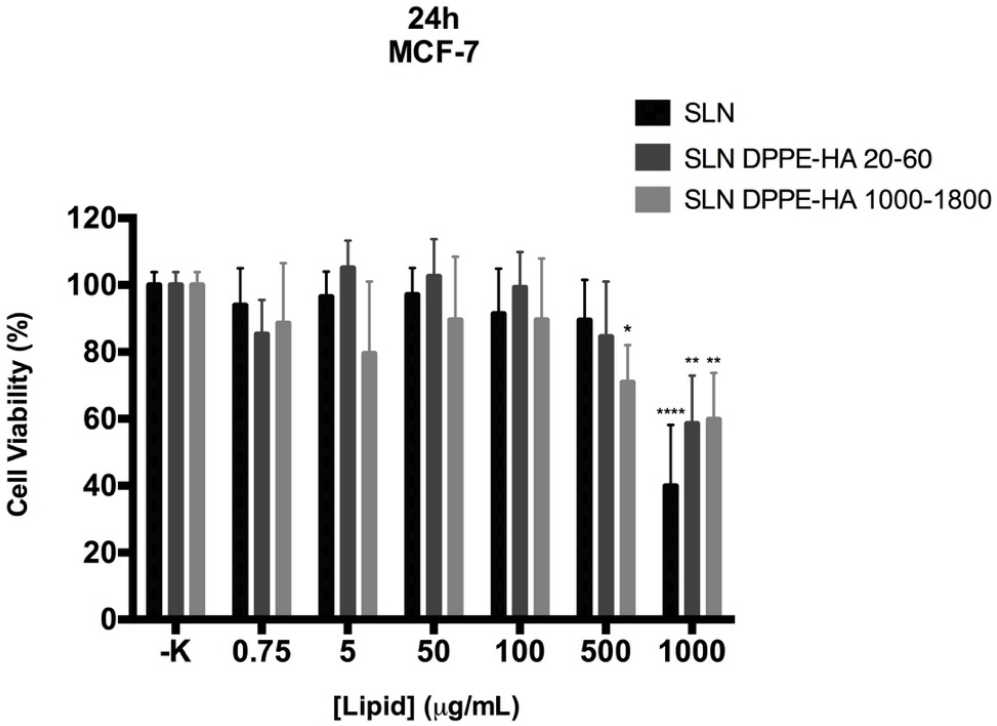


Figure 19 MCF-7 cell viability assessed by Resazurin assay after 24 hours of exposure to the different nanoformulations at increasing concentrations of SLN. Values represent the mean ± SD (n>3); *p<0.05, **p<0.01, ****p<0.0001. Results were compared with DMEM medium, which represents the maximum of cell viability

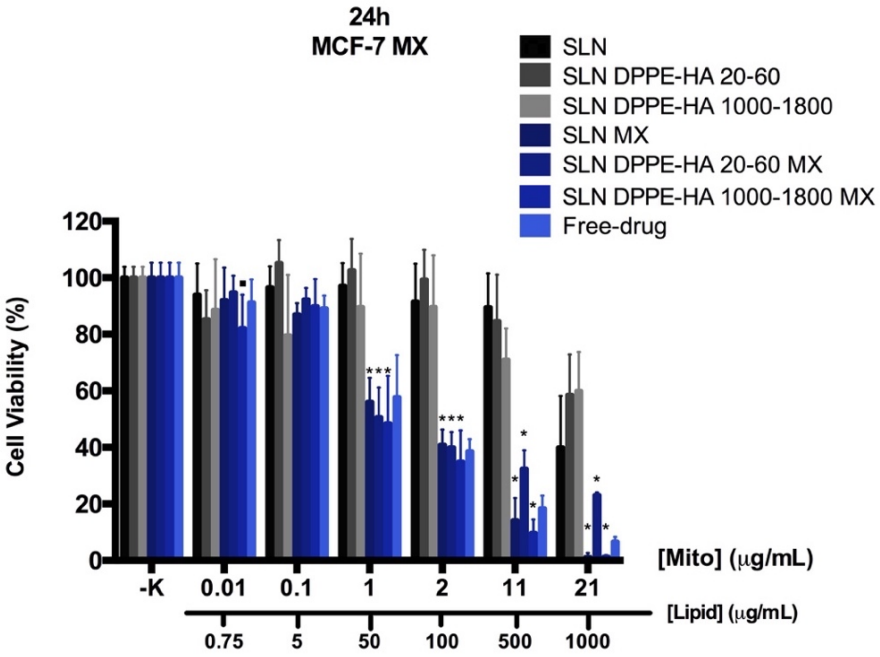


Figure 20 MCF-7 cell viability assessed by Resazurin assay after 24 hours of exposure to the different nanoformulations at increasing concentrations of MX (or the equivalent solid amount of lipid in unloaded SLN). Values represent the mean ± SD (n=3). Results were compared with DMEM medium, which represents the maximum of cell viability (K-). () denotes statistically significant differences of p<0.05 and (*) denotes statistically significant differences of p<0.0001

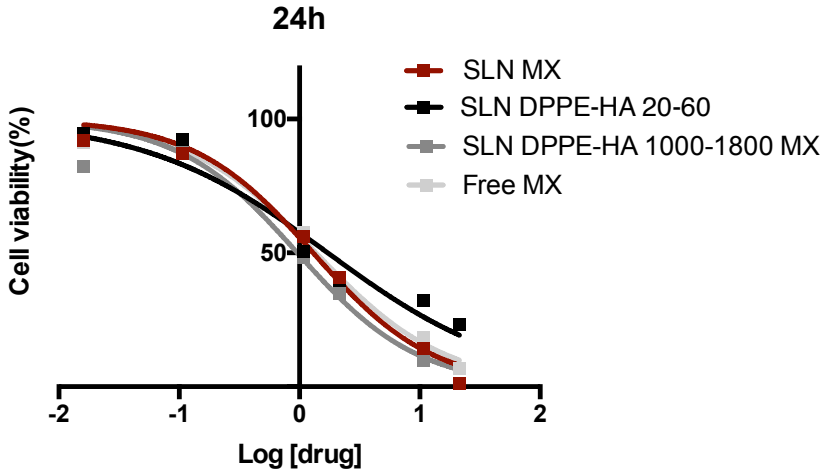


Figure 21 Dose-response curves of MCF-7 cells incubation with free mitoxantrone and the different nanoformulations

3.4.3. Cellular uptake

NPs can enter cells by several routes including active transport via ligand-receptor [154]. The goal of this novel NPs is to increase their accumulation, and thus the drug, within the target cancer cells by using HA as a ligand for the CD44 receptor overexpressed on breast cancer cells.

In order to study the cellular uptake of the functionalized SLN, MCF-7 cells expressing the HA receptor were used.

First, confocal microscopy was used to assess and visualize the internalization of NPs carrying the intrinsically fluorescent MX medicine into MCF-7 after 4h and 24h of incubation. As shown in Figure 22, at 4h of incubation it is possible to observe the MCF-7 cells uptake of MX (red) for all NPs, not seen in the control picture (Figure 22, Control, C). The NPs internalizations seem to be accumulated mostly in the lysosomes at the level of the cytoplasm. Furthermore, intracellular fluorescence appears to be more prominent in cells that have internalized the DPPE-HA 1000-1800 functionalized particles. After 24h, the fluorescence intensity is higher, which can be shown by color saturation (red channel), and is co-localized in the nucleus of cells, suggesting that the drug reached this compartment after this period of time. Although the emergence of intracellular fluorescence cannot be considered a quantitative, but rather a qualitative measure of MX uptake by breast cancer cells, the observations comparing the uptake between SLN and HA functionalized SLN by the MCF-7 cells, provides evidence for the preferential uptake of both HA 20-60 and HA 1000-1800 functionalized SLN after both incubation periods. In addition, when comparing the two HA MW-functionalized SLN, HA 1000-1800 seems to induce a higher MX internalization in MCF-7 cells.

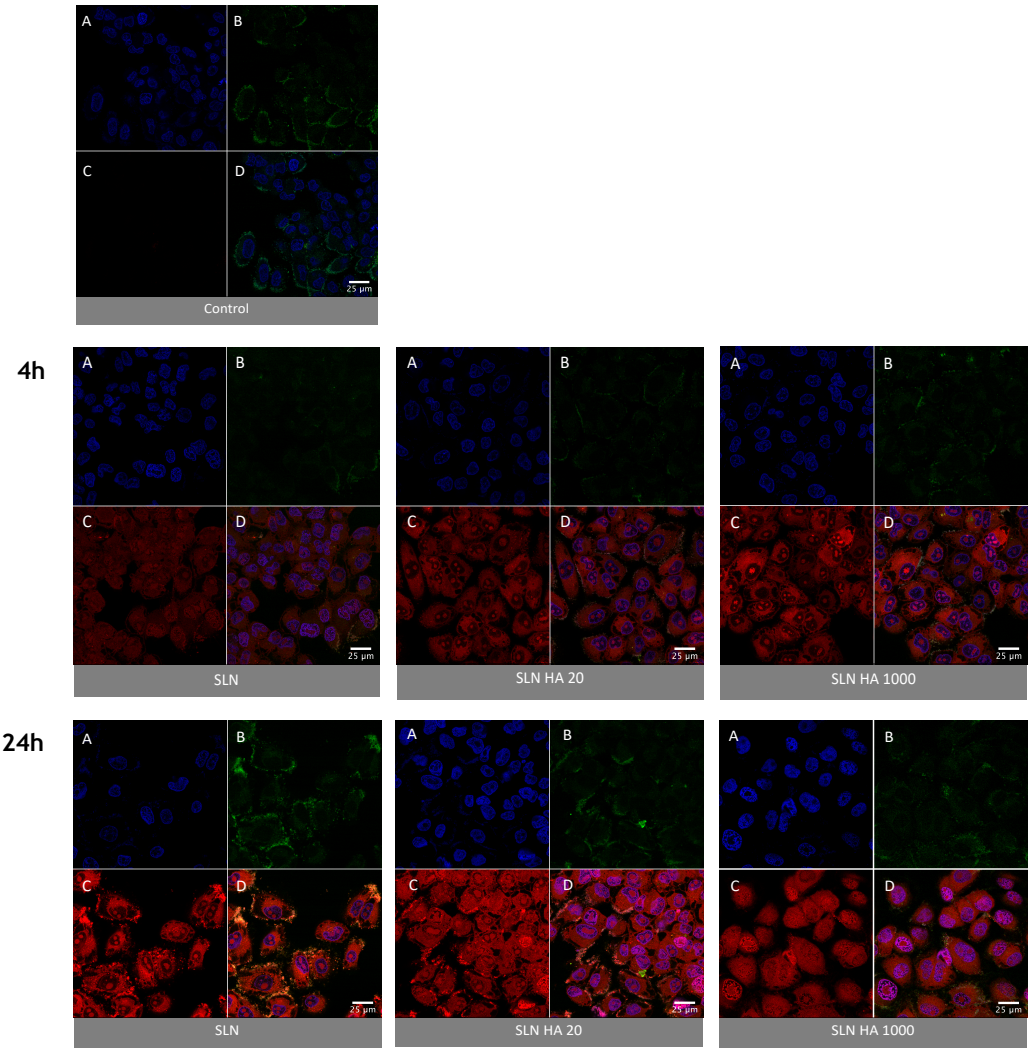


Figure 22 Confocal microscopy images of MCF-7 exposed to different MX loaded nanoparticles (SLN, SLN HA 20-60, SLN HA 1000-1800) for 4h and 24h. Blue channel: Hoechst 33342 (nucleus). Green channel: LysoTracker™ Green DND-26. Red channel: MX

In addition to imaging record of the MCF-7 uptake of MX, a quantitative analysis was performed by flow cytometry using C6-loaded SLN with and without HA. With that purpose, SLN were marked with fluorophore C6. The mean fluorescence measured within the cells in different time-points after incubation with the NPs is shown in Figure 23. It is possible to observe an increase in fluorescence over time, suggesting a time-dependent uptake, which increased considerably from the first hour up to 4 hours of incubation. After 4h, the increment in fluorescence was less accentuated, indicating that there has been a saturation of the particles internalization. Moreover, a significantly higher internalization is observed by SLN DPPE-HA 1000-1800 SLN compared to SLN alone and HA 20 functionalized particles. These findings corroborate the results obtained with confocal microscopy, where a higher internalization of MX was visually detected after incubation of DPPE-HA 1000-1800 SLN and with the cell viability assays, that demonstrated that 1000-1800 HA-SLN induced a higher cancer cell death compared to the other SLN and free MX, as quantitatively assessed by the value of IC_{50}. This outcome is also in agreement with other works reported in the literature, demonstrating that high-molecular-weight HA (≥ 30 kDa) has a stronger binding affinity to CD44 receptors, which

makes HMW HA-functionalized NPs more effective against cancerous cells expressing CD44 [78, 155]. Overall, these results support that HA polysaccharide can be used to to enhance the internalization of SLN in CD44+ breast cancer cells and that a better outcome can be achieved by using a HA of elevated MW.

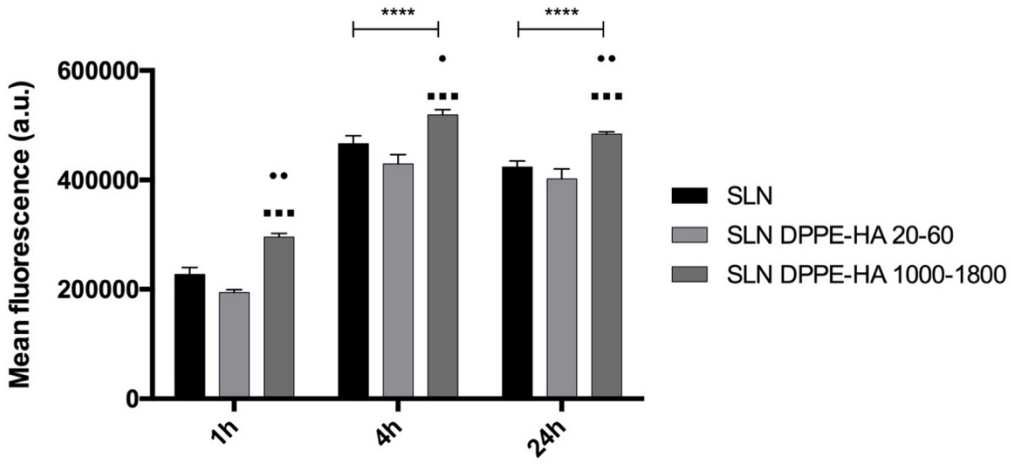


Figure 23 Cellular uptake for C6-loaded SLN in MCF-7 cells, after 1h, 4h and 24h of incubation. Data expressed as mean ± standard deviation (n =2). (****) denotes statistically significant differences of $p<0.0001$ relatively to the correspondent value at 1h, (•) and (••) denotes significant differences relatively to SLN of $p<0.05$ and $p<0.001$, respectively, and () denotes statistically significant differences of $p<0.001$ in regard to SLN DPPE-HA 20-60

Chapter 4 Conclusion and Future Prospects

In this work, HA functionalized lipid-based nanoformulations loaded with MX are proposed as a drug carrier solution to improve the delivery of mitoxantrone to breast cancer cells, aiming to improve the efficacy of the drug and limit its adverse side-effects. The strategy proposed in this work proved to be successful, leading to and improvement of the accumulation of the MX-loaded NPs into breast cancer cells.

SLN were produced using an organic-solvent free, low-cost production method assured of easy scale-up. The synthesis of a HA conjugate was successfully performed and the HA-functionalized NPs proved to be suitable for intravenous administration, showing no toxicity to human RBCs. Two HA of different molecular weights (HA 20-60 kDa and HA 1000-1800 kDa) were explored to understand their role in MX-SLN internalization by breast cancer cells and their impact on the proposed goal.

The characteristics of the SLN prepared proved to be very promising for the goal of intravenous administration of MX and subsequent delivery and action at the intra-tumoral level. Overall, SLN presented proper size for delivery into the bloodstream and tumor passive targeting by exploiting the EPR effect. The MX was efficiently encapsulated within the lipidic matrix of the NPs, showing an EE% greater than 88% that remained high for at least 1 month. The SLN *in vitro* release studies suggest that at the end of 24 hours after injection into the bloodstream, around 50% of MX will remain encapsulated due to its controlled release at physiological pH and then a much higher MX release will occur after reaching the acidic intracellular endosomal compartment, where it can be released and exert its action at the DNA level. In addition, hemolysis assay conducted using human RBCs in unloaded and MX loaded SLN revealed that this nanoformulations are non-hemolytic even at very high concentrations.

Furthermore, the biocompatibility of SLN alone and coated with HA was assessed in the human breast cancer cell line MCF-7 showing very high tolerability even for high concentrations of lipid. The cell viability of MCF-7 assessed after 24h exposure to the NPs carrying the anticancer drug revealed their therapeutic efficacy for concentrations as low as 5 µg/mL of drug (50 µg/mL of lipid). The values of IC_{50} showed that NPs could induced similar anti-cancer effects than the free drug, with SLN HA 1000-1800 exceeding the anti-cancer effectiveness of free-MX.

Finally, SLN uptake assays conducted in MCF-7 showed a time-dependent internalization and a preferential uptake of HA 1000-1800 functionalized SLN, a fact that was demonstrated using both confocal microscopy and flow cytometry.

Till this date, there has not yet been a consensus as to which molecular weights have the greatest ability to provide an active targeting for drug delivery through a nanotherapeutic approach, so our study served to add scientific evidence on this subject.

This work was built on a green nanotechnology that holds promising features for improved drug delivery for breast cancer. However, further analysis of NPs stability for greater period of time should be performed to support the results obtained.

Furthermore, for more representative analysis, *in vitro* studies should be conducted in negative controls, i.e. in cell lines with no expression of the HA receptor, such as JURKAT cell line [156]. Likewise, cells with higher expression of CD44 as the human breast cancer cell line MBA-MB 231 or HaCat cells from the skin should be used for comparative studies with SLN and MCF-7 interaction outcomes [78, 157, 158]. Moreover, in the future, additional reading time-points could be interesting for the cellular uptake assays as well as live imaging using confocal microscopy, for tracking of NPs delivery to cells in real-time. [159, 160]

Lastly, quantification of the amount of HA effectively bound to the NPs would be of great importance to verify the accuracy of the results obtained and to support conclusions drawn from the comparisons made between the non-functionalized and functionalized particles with HA 20-60 or with HA 1000-1800. Thus, more sensitive HA quantification tests could be explored for this purpose.

References

1. DeVita VT, L.T., Lawrence TS, Rosenberg SA, *Devita, Hellman, and Rosenberg's Cancer: Principles and Practice of Oncology*. 11th ed. 2019, Philadelphia.

2. Sung, H., et al., *Global Cancer Statistics 2020: GLOBOCAN Estimates of Incidence and Mortality Worldwide for 36 Cancers in 185 Countries*. CA Cancer J Clin, 2021. **71**(3): p. 209-249.

3. WHO (2021). *Breast cancer*. 12 september 2021]; Available from: https://www.who.int/news-room/fact-sheets/detail/breast-cancer.

4. Luengo-Fernandez, R., et al., *Economic burden of cancer across the European Union: a population-based cost analysis*. Lancet Oncol, 2013. **14**(12): p. 1165-74.

5. Mariotto, A.B., et al., *Projections of the cost of cancer care in the United States: 2010-2020*. J Natl Cancer Inst, 2011. **103**(2): p. 117-28.

6. Wu, D., et al., *Nanomedicine applications in the treatment of breast cancer: current state of the art*. Int J Nanomedicine, 2017. **12**: p. 5879-5892.

7. Waks, A.G. and E.P. Winer, *Breast Cancer Treatment: A Review*. Jama, 2019. **321**(3): p. 288-300.

8. Kumar, V., A.K. Abbas, N. Fausto, J.C. Aster, *Robbins and Cotran pathologic basis of disease*. 7th ed. ed. 2014, United States: Elsevier Health Sciences.

9. Sinn, H.P. and H. Kreipe, *A Brief Overview of the WHO Classification of Breast Tumors, 4th Edition, Focusing on Issues and Updates from the 3rd Edition*. Breast Care (Basel), 2013. **8**(2): p. 149-54.

10. Goldhirsch, A., et al., *Thresholds for therapies: highlights of the St Gallen International Expert Consensus on the primary therapy of early breast cancer 2009*. Ann Oncol, 2009. **20**(8): p. 1319-29.

11. National Guideline, A., *National Institute for Health and Care Excellence: Clinical Guidelines*, in *Early and locally advanced breast cancer: diagnosis and management*. 2018, National Institute for Health and Care Excellence (UK). Copyright © NICE 2018.: London.

12. Early Breast Cancer Trialists' Collaborative, G., et al., *Relevance of breast cancer hormone receptors and other factors to the efficacy of adjuvant tamoxifen: patient-level meta-analysis of randomised trials*. Lancet, 2011. **378**(9793): p. 771-84.

13. Morrow, P.K., F. Zambrana, and F.J. Esteva, *Recent advances in systemic therapy: Advances in systemic therapy for HER2-positive metastatic breast cancer*. Breast Cancer Res, 2009. **11**(4): p. 207.

14. Zhao, W., et al., *Effectiveness of second-line anti-HER2 treatment in HER2-positive metastatic breast cancer patients previously treated with trastuzumab: A real-world study*. Chin J Cancer Res, 2020. **32**(3): p. 361-369.

15. Andreopoulou, E. and J.A. Sparano, *Chemotherapy in Patients with Anthracycline- and Taxane-Pretreated Metastatic Breast Cancer: An Overview*. Curr Breast Cancer Rep, 2013. **5**(1): p. 42-50.

16. Blanco, E. and M. Ferrari, *Emerging nanotherapeutic strategies in breast cancer*. Breast, 2014. **23**(1): p. 10-8.

17. Bachur, N.R., *Encyclopedia of Cancer. Anthracyclines*. Second Edition ed. 2002.

18. Abu Samaan, T.M., et al., *Paclitaxel's Mechanistic and Clinical Effects on Breast Cancer*. Biomolecules, 2019. **9**(12).

19. Zhao, C.Y., et al., *Nanotechnology for Cancer Therapy Based on Chemotherapy*. Molecules, 2018. **23**(4).

20. Tipton, J.M., *Handbook of Cancer Chemotherapy (8th edition)*. 8th ed, ed. R.T.S.a.S.N. Khleif. 2011.

21. Shapiro, C.L. and A. Recht, *Side effects of adjuvant treatment of breast cancer*. N Engl J Med, 2001. **344**(26): p. 1997-2008.

22. Tao, J.J., K. Visvanathan, and A.C. Wolff, *Long term side effects of adjuvant chemotherapy in patients with early breast cancer*. Breast, 2015. **24 Suppl 2**: p. S149-53.

23. White, R.J. and F.E. Durr, *Development of mitoxantrone*. Invest New Drugs, 1985. **3**(2): p. 85-93.

24. NCI Dictionaries. *Dictionary of Cancer Terms.*; Available from: https://www.cancer.gov/publications/dictionaries/cancer-terms/def/anthracenedione.

25. Durr, F.E., *Biologic and biochemical effects of mitoxantrone*. Semin Oncol, 1984. **11**(3 Suppl 1): p. 3-10.

26. Pritish Varadwaj, K.M., Anju Sharma, Rajnish Kumar, *Mitoxantrone: An agent with promises for anticancer therapies*. Electronic Journal of Biology, 2010. **6**: p. 36-42.

27. Marosi, C., *Neuro-Oncology Part II*. Vol. 105. 2012.

28. *Mitoxantrone*. 12 september 2021]; Available from: https://adisinsight.springer.com/drugs/800009052.

29. Shenkenberg, T.D. and D.D. Von Hoff, *Mitoxantrone: a new anticancer drug with significant clinical activity*. Ann Intern Med, 1986. **105**(1): p. 67-81.

30. Bell, D.H., *Characterization of the fluorescence of the antitumor agent, mitoxantrone*. Biochim Biophys Acta, 1988. **949**(1): p. 132-7.

31. Feofanov, A., et al., *Localization and molecular interactions of mitoxantrone within living K562 cells as probed by confocal spectral imaging analysis*. Biophys J, 1997. **73**(6): p. 3317-27.

32. Smith, P.J., et al., *Subcellular distribution of the anticancer drug mitoxantrone in human and drug-resistant murine cells analyzed by flow cytometry and confocal microscopy and its relationship to the induction of DNA damage*. Cancer Res, 1992. **52**(14): p. 4000-8.

33. Enache, M. and E. Volanschi, *Spectral studies on the molecular interaction of anticancer drug mitoxantrone with CTAB micelles*. J Pharm Sci, 2011. **100**(2): p. 558-65.

34. Ehninger, G., et al., *Pharmacokinetics and metabolism of mitoxantrone. A review*. Clin Pharmacokinet, 1990. **18**(5): p. 365-80.

35. Arlin, Z., et al., *Randomized multicenter trial of cytosine arabinoside with mitoxantrone or daunorubicin in previously untreated adult patients with acute nonlymphocytic leukemia (ANLL). Lederle Cooperative Group*. Leukemia, 1990. **4**(3): p. 177-83.

36. Faulds, D., et al., *Mitoxantrone. A review of its pharmacodynamic and pharmacokinetic properties, and therapeutic potential in the chemotherapy of cancer*. Drugs, 1991. **41**(3): p. 400-49.

37. Sargazi, A., et al., *Hyaluronic acid/polyethylene glycol nanoparticles for controlled delivery of mitoxantrone*. Artif Cells Nanomed Biotechnol, 2018. **46**(3): p. 500-509.

38. Fujimoto, S. and M. Ogawa, *Antitumor activity of mitoxantrone against murine experimental tumors: comparative analysis against various antitumor antibiotics*. Cancer Chemother Pharmacol, 1982. **8**(2): p. 157-62.

39. Johnson, R.K., et al., *Experimental antitumor activity of aminoanthraquinones*. Cancer Treat Rep, 1979. **63**(3): p. 425-39.

40. Rajashekar Kammari, N.G.D., Sudip K.Das, *Nanoparticulate Systems for Therapeutic and Diagnostic Applications*, in *Emerging Nanotechnologies for Diagnostics, Drug Delivery and Medical Devices*, K.C.a.A.M. Ashim K. Mitra, Editor. 2017. p. 105-144.

41. Chang Hyun Kim, S.G.L., Myung Joo Kang, Sangkil Lee & Young Wook Choi, *Surface modification of lipid-based nanocarriers for cancer cell-specific drug targeting*. Journal of Pharmaceutical Investigation, 2017.

42. Prasad, M., et al., *Nanotherapeutics: An insight into healthcare and multi-dimensional applications in medical sector of the modern world*. Biomed Pharmacother, 2018. **97**: p. 1521-1537.

43. Farhat, F.S., et al., *A phase II study of lipoplatin (liposomal cisplatin)/vinorelbine combination in HER-2/neu-negative metastatic breast cancer*. Clin Breast Cancer, 2011. **11**(6): p. 384-9.

44. Zielińska, A., et al., *Cancer Nanopharmaceuticals: Physicochemical Characterization and In Vitro/In Vivo Applications*. Cancers (Basel), 2021. **13**(8).

45. Qian, X.L., et al., *Caveolin-1: a multifaceted driver of breast cancer progression and its application in clinical treatment*. Onco Targets Ther, 2019. **12**: p. 1539-1552.

46. Li, B., et al., *Nanoparticle albumin-bound paclitaxel versus solvent-based paclitaxel in breast cancer: A protocol for systemic review and meta-analysis*. Medicine (Baltimore), 2021. **100**(7): p. e24514.

47. Gardner, E.R., et al., *Randomized crossover pharmacokinetic study of solvent-based paclitaxel and nab-paclitaxel.* Clin Cancer Res, 2008. **14**(13): p. 4200-5.

48. Chen, Y., et al., *Nab-paclitaxel-based regimens with docetaxel-based regimens as neoadjuvant treatment for early breast cancer.* Invest New Drugs, 2021. **39**(2): p. 524-529.

49. Gradishar, W.J., et al., *Phase III trial of nanoparticle albumin-bound paclitaxel compared with polyethylated castor oil-based paclitaxel in women with breast cancer.* J Clin Oncol, 2005. **23**(31): p. 7794-803.

50. Ghasemiyeh, P. and S. Mohammadi-Samani, *Solid lipid nanoparticles and nanostructured lipid carriers as novel drug delivery systems: applications, advantages and disadvantages.* Res Pharm Sci, 2018. **13**(4): p. 288-303.

51. Ameya Deshpande, M.M., Saloni B. Daftardar, Meghavi Patel, Sai H.S. Boddu, Jerry Nesamony, *Chapter 12. Solid Lipid Nanoparticles in Drug Delivery: Opportunities and Challenges*, in *Emerging Nanotechnologies for Diagnostics, Drug Delivery and Medical Devices*, A.M.K.C.A. Mandal, Editor. 2017, Elsevier. p. 291-330.

52. Shah, R.M., et al., *Transport of stearic acid-based solid lipid nanoparticles (SLNs) into human epithelial cells.* Colloids Surf B Biointerfaces, 2016. **140**: p. 204-212.

53. Poovi Ganesan, D.N., *Lipid nanoparticles: Different preparation techniques, characterization, hurdles, and strategies for the production of solid lipid nanoparticles and nanostructured lipid carriers for oral drug delivery.* Sustainable Chemistry and Pharmacy, 2017. **6**: p. 37-56.

54. Pardeike, J., A. Hommoss, and R.H. Müller, *Lipid nanoparticles (SLN, NLC) in cosmetic and pharmaceutical dermal products.* Int J Pharm, 2009. **366**(1-2): p. 170-84.

55. Borges, A., et al., *Solid Lipid Nanoparticles as Carriers of Natural Phenolic Compounds.* Antioxidants (Basel), 2020. **9**(10).

56. Puri, A., et al., *Lipid-based nanoparticles as pharmaceutical drug carriers: from concepts to clinic.* Crit Rev Ther Drug Carrier Syst, 2009. **26**(6): p. 523-80.

57. Hadinoto, K., A. Sundaresan, and W.S. Cheow, *Lipid-polymer hybrid nanoparticles as a new generation therapeutic delivery platform: a review.* Eur J Pharm Biopharm, 2013. **85**(3 Pt A): p. 427-43.

58. Shah, R., Eldridge, D., Palombo, E., Harding, I., *Lipid Nanoparticles: Production, Characterization and Stability*. 1st ed. 2015.

59. Müller, R.H., K. Mäder, and S. Gohla, *Solid lipid nanoparticles (SLN) for controlled drug delivery - a review of the state of the art*. Eur J Pharm Biopharm, 2000. **50**(1): p. 161-77.

60. Rohit Bhandari, I.P.K., *A Method to Prepare Solid Lipid Nanoparticles with Improved Entrapment Efficiency of Hydrophilic Drugs*. Current Nanoscience 2013. **9**: p. 211-220.

61. Shah, M., et al., *Solid lipid nanoparticles of a water soluble drug, ciprofloxacin hydrochloride*. Indian J Pharm Sci, 2012. **74**(5): p. 434-42.

62. Liu, D., et al., *Formulation and characterization of hydrophilic drug diclofenac sodium-loaded solid lipid nanoparticles based on phospholipid complexes technology*. J Liposome Res, 2014. **24**(1): p. 17-26.

63. Cho, H.J., et al., *Surface-modified solid lipid nanoparticles for oral delivery of docetaxel: enhanced intestinal absorption and lymphatic uptake*. Int J Nanomedicine, 2014. **9**: p. 495-504.

64. Sarmento, B., et al., *Oral insulin delivery by means of solid lipid nanoparticles*. Int J Nanomedicine, 2007. **2**(4): p. 743-9.

65. Zara, G.P., et al., *Intravenous administration to rabbits of non-stealth and stealth doxorubicin-loaded solid lipid nanoparticles at increasing concentrations of stealth agent: pharmacokinetics and distribution of doxorubicin in brain and other tissues*. J Drug Target, 2002. **10**(4): p. 327-35.

66. Manjunath, K. and V. Venkateswarlu, *Pharmacokinetics, tissue distribution and bioavailability of nitrendipine solid lipid nanoparticles after intravenous and intraduodenal administration*. J Drug Target, 2006. **14**(9): p. 632-45.

67. Yang, S.C., et al., *Body distribution in mice of intravenously injected camptothecin solid lipid nanoparticles and targeting effect on brain*. J Control Release, 1999. **59**(3): p. 299-307.

68. Lee, M.K., S.J. Lim, and C.K. Kim, *Preparation, characterization and in vitro cytotoxicity of paclitaxel-loaded sterically stabilized solid lipid nanoparticles*. Biomaterials, 2007. **28**(12): p. 2137-46.

69. Fontana, G., et al., *Solid lipid nanoparticles containing tamoxifen characterization and in vitro antitumoral activity*. Drug Deliv, 2005. **12**(6): p. 385-92.

70. Samson A. Adeyemi, P.K., Yahya E. Choonara, and Viness Pillay, *Stealth Properties of Nanoparticles Against Cancer: Surface Modification of NPs for Passive Targeting to Human Cancer Tissue in Zebrafish Embryos*, in *Surface Modification of Nanoparticles for Targeted Drug Delivery*, Y.V. Pathak, Editor. 2019. p. 99-124.

71. He, X., et al., *pH-sensitive drug-delivery systems for tumor targeting*. Ther Deliv, 2013. **4**(12): p. 1499-510.

72. Xu, H., et al., *CD44 as a tumor biomarker and therapeutic target*. Exp Hematol Oncol, 2020. **9**(1): p. 36.

73. Jordan, A.R., et al., *The Role of CD44 in Disease Pathophysiology and Targeted Treatment*. Front Immunol, 2015. **6**: p. 182.

74. Laurent, T.C. and J.R. Fraser, *Hyaluronan*. Faseb j, 1992. **6**(7): p. 2397-404.

75. Stern, R., *Hyaluronan in cancer biology*. Semin Cancer Biol, 2008. **18**(4): p. 237.

76. Gupta, R.C., et al., *Hyaluronic Acid: Molecular Mechanisms and Therapeutic Trajectory*. Front Vet Sci, 2019. **6**: p. 192.

77. Stern, R., *Hyaluronidases in cancer biology*. Semin Cancer Biol, 2008. **18**(4): p. 275-80.

78. Spadea, A., et al., *Evaluating the Efficiency of Hyaluronic Acid for Tumor Targeting via CD44*. Mol Pharm, 2019. **16**(6): p. 2481-2493.

79. Tavianatou, A.G., et al., *Molecular size-dependent specificity of hyaluronan on functional properties, morphology and matrix composition of mammary cancer cells*. Matrix Biol Plus, 2019. **3**: p. 100008.

80. Jiang, L., et al., *Molecular weight impact on the mechanical forces between hyaluronan and its receptor*. Carbohydr Polym, 2018. **197**: p. 326-336.

81. Zhong, L., et al., *Exploring the relationship of hyaluronic acid molecular weight and active targeting efficiency for designing hyaluronic acid-modified nanoparticles*. Asian J Pharm Sci, 2019. **14**(5): p. 521-530.

82. Price, Z.K., N.A. Lokman, and C. Ricciardelli, *Differing Roles of Hyaluronan Molecular Weight on Cancer Cell Behavior and Chemotherapy Resistance*. Cancers (Basel), 2018. **10**(12).

83. Naor, D., *Editorial: Interaction Between Hyaluronic Acid and Its Receptors (CD44, RHAMM) Regulates the Activity of Inflammation and Cancer*. Front Immunol, 2016. **7**: p. 39.

84. Sakurai, Y. and H. Harashima, *Hyaluronan-modified nanoparticles for tumor-targeting*. Expert Opin Drug Deliv, 2019. **16**(9): p. 915-936.

85. Wang, X., et al., *Hyaluronic acid modification of RNase A and its intracellular delivery using lipid-like nanoparticles*. J Control Release, 2017. **263**: p. 39-45.

86. Qhattal, H.S. and X. Liu, *Characterization of CD44-mediated cancer cell uptake and intracellular distribution of hyaluronan-grafted liposomes*. Mol Pharm, 2011. **8**(4): p. 1233-46.

87. Xu, H., et al., *The role of CD44 in epithelial-mesenchymal transition and cancer development*. Onco Targets Ther, 2015. **8**: p. 3783-92.

88. Landesman-Milo, D., et al., *Hyaluronan grafted lipid-based nanoparticles as RNAi carriers for cancer cells*. Cancer Lett, 2013. **334**(2): p. 221-7.

89. Granja, A., et al., *Mitoxantrone-loaded lipid nanoparticles for breast cancer therapy - Quality-by-design approach and efficacy assessment in 2D and 3D in vitro cancer models*. Int J Pharm, 2021. **607**: p. 121044.

90. *PubChem Compound Summary for CID 10889, Cetyl palmitate*. . 2021 September 13, 2021].

91. Garidel, P., C. Hoffmann, and A. Blume, *A thermodynamic analysis of the binding interaction between polysorbate 20 and 80 with human serum albumins and immunoglobulins: a contribution to understand colloidal protein stabilisation*. Biophys Chem, 2009. **143**(1-2): p. 70-8.

92. *TWEEN® 80*. 13 september 2021]; Available from: https://www.sigmaaldrich.com/PT/en/product/sial/p1754.

93. Song, H., et al., *Development of Polysorbate 80/Phospholipid mixed micellar formation for docetaxel and assessment of its in vivo distribution in animal models.* Nanoscale Res Lett, 2011. **6**(1): p. 354.

94. Cheng, M.A., et al., *Androgen receptor (AR) degradation enhancer ASC-J9(®) in an FDA-approved formulated solution suppresses castration resistant prostate cancer cell growth.* Cancer Lett, 2018. **417**: p. 182-191.

95. Cosco, D., et al., *Polysaccharide-coated liposomes by post-insertion of a hyaluronan-lipid conjugate.* Colloids Surf B Biointerfaces, 2017. **158**: p. 119-126.

96. Gouveia, V.M., et al., *Hyaluronic acid-conjugated pH-sensitive liposomes for targeted delivery of prednisolone on rheumatoid arthritis therapy.* Nanomedicine (Lond), 2018. **13**(9): p. 1037-1049.

97. JEOL (2021). *NMR basic knowledge*. 13 september 2021]; Available from: https://www.jeol.co.jp/en/products/nmr/basics.html.

98. Kaur, I.P., et al., *Potential of solid lipid nanoparticles in brain targeting.* J Control Release, 2008. **127**(2): p. 97-109.

99. Hwang T.L., S.A.J., *Water Suppression That Works. Excitation Sculpting Using Arbitrary Wave-Forms and Pulsed-Field Gradients.* Journal of Magnetic Resonance, Series A, 1995. **112**(2): p. 275-279.

100. Sastry, M., *Electrostatic assembly of nanoparticles*, in *Nanoparticles. Nanostructure Science and Technology* 2004, Springer, Boston, MA. p. 225-250.

101. Sang-Eun Lee, C.D., Jung BinAhn, Dong-HyunKim, Jung Kyu Lee, Ji-Yun Lee, Jin-Seok Choi, Jeong-Sook Park, *Hyaluronic acid-coated solid lipid nanoparticles to overcome drug-resistance in tumor cells.* Journal of Drug Delivery Science and Technology, 2019. **50**.

102. Tran, T.H., et al., *Hyaluronic acid-coated solid lipid nanoparticles for targeted delivery of vorinostat to CD44 overexpressing cancer cells.* Carbohydr Polym, 2014. **114**: p. 407-415.

103. Shen, H., et al., *Coating Solid Lipid Nanoparticles with Hyaluronic Acid Enhances Antitumor Activity against Melanoma Stem-like Cells.* Theranostics, 2015. **5**(7): p. 755-71.

104. Yong-Hao Chen, Q.W., *Establishment of CTAB Turbidimetric method to determine hyaluronic acid content in fermentation broth*. Carbohydrate Polymers, 2009. **78**(1): p. 178-181.

105. Bitter, T. and H.M. Muir, *A modified uronic acid carbazole reaction*. Anal Biochem, 1962. **4**: p. 330-4.

106. Marina Cesaretti, E.L., Francesca Maccari, Nicola Volpi, *A 96-well assay for uronic acid carbazole reaction*. Carbohydrate Polymers, 2003. **54**(1): p. 59-61.

107. Oueslati, N., et al., *CTAB turbidimetric method for assaying hyaluronic acid in complex environments and under cross-linked form*. Carbohydr Polym, 2014. **112**: p. 102-8.

108. Bhatnagar, P., et al., *Hyaluronic acid grafted PLGA copolymer nanoparticles enhance the targeted delivery of Bromelain in Ehrlich's Ascites Carcinoma*. Eur J Pharm Biopharm, 2016. **105**: p. 176-92.

109. Vangara, K.K., J.L. Liu, and S. Palakurthi, *Hyaluronic acid-decorated PLGA-PEG nanoparticles for targeted delivery of SN-38 to ovarian cancer*. Anticancer Res, 2013. **33**(6): p. 2425-34.

110. Xiao, B., et al., *Orally Targeted Delivery of Tripeptide KPV via Hyaluronic Acid-Functionalized Nanoparticles Efficiently Alleviates Ulcerative Colitis*. Mol Ther, 2017. **25**(7): p. 1628-1640.

111. Satinder K.Brar, M.V., *Measurement of nanoparticles by light-scattering techniques*. TrAC Trends in Analytical Chemistry, 2011. **30**(1): p. 4-17.

112. Lin, P.C., et al., *Techniques for physicochemical characterization of nanomaterials*. Biotechnol Adv, 2014. **32**(4): p. 711-26.

113. Kumar, N.a.S.K., *Essentials in Nanoscience and Nanotechnology*. 2016: John Wiley & Son.

114. *Zeta Potential Measurements*. 13 september 2021]; Available from: https://www.microtrac.com/products/zeta-potential/.

115. Mehmet Gumustas, C.T.S.-T., Aysen Gumustas, Sibel A. Ozkan, Bengi Uslu, *Effect of Polymer-Based Nanoparticles on the Assay of Antimicrobial Drug Delivery Systems*,

in *Multifunctional Systems for Combined Delivery, Biosensing and Diagnostics*, A.M. Grumezescu, Editor. 2017. p. 67-108.

116. Shabnam Samimi, N.M., Reza Baradaran Eftekhari, Farid Dorkoosh, *Lipid-Based Nanoparticles for Drug Delivery Systems*, in *Characterization and Biology of Nanomaterials for Drug Delivery*. 2019, Elsevier. p. 47-76.

117. Chang, T.M.S., *Selected topics in nanomedicine*. Vol. 3. 2013: World Scientific.

118. Filipe, V., A. Hawe, and W. Jiskoot, *Critical evaluation of Nanoparticle Tracking Analysis (NTA) by NanoSight for the measurement of nanoparticles and protein aggregates.* Pharm Res, 2010. **27**(5): p. 796-810.

119. Boedtkjer, E. and S.F. Pedersen, *The Acidic Tumor Microenvironment as a Driver of Cancer*. Annu Rev Physiol, 2020. **82**: p. 103-126.

120. D'Souza, S., *A Review of In Vitro Drug Release Test Methods for Nano-Sized Dosage Forms.* Advances in Pharmaceutics, 2014.

121. Moraes, S., et al., *Targeted nanostructured lipid carriers for doxorubicin oral delivery.* Int J Pharm, 2021. **592**: p. 120029.

122. Greco, I., et al., *Correlation between hemolytic activity, cytotoxicity and systemic in vivo toxicity of synthetic antimicrobial peptides.* Sci Rep, 2020. **10**(1): p. 13206.

123. Bielawski, J., *Two types of haemolytic activity of detergents.* Biochim Biophys Acta, 1990. **1035**(2): p. 214-7.

124. Trägner, D. and A. Csordas, *Biphasic interaction of Triton detergents with the erythrocyte membrane*. Biochem J, 1987. **244**(3): p. 605-9.

125. Deibler, G.E., et al., *Use of triton X-100 as a hemolytic agent in the spectrophotometric measurement of blood O2 saturation.* J Appl Physiol, 1959. **14**(1): p. 133-6.

126. *In vitro Hemolysis Assay*. 13 september 2021]; Available from: https://www.cyprotex.com/toxicology/mechanistic-toxicity/hemolysis.

127. Nakayama, G.R., et al., *Assessment of the Alamar Blue assay for cellular growth and viability in vitro.* J Immunol Methods, 1997. **204**(2): p. 205-8.

128. O'Brien, J., et al., *Investigation of the Alamar Blue (resazurin) fluorescent dye for the assessment of mammalian cell cytotoxicity.* Eur J Biochem, 2000. **267**(17): p. 5421-6.

129. Dey, V.R.a.N., *The Basics of Confocal Microscopy*, in *Laser Scanning, Theory and Applications*. 2010.

130. Shi, H., et al., *Nanoparticle-based biocompatible and long-life marker for lysosome labeling and tracking.* Anal Chem, 2010. **82**(6): p. 2213-20.

131. *LysoTracker® and LysoSensorTM Probes*. 13 september 2021]; Available from: https://www.thermofisher.com/document-connect/document-connect.html?url=https%3A%2F%2Fassets.thermofisher.com%2FTFS-Assets%2FLSG%2Fmanuals%2Fmp07525.pdf&title=THlzb1RyYWNrZXIgYW5kIEx5c29TZW5zb3IgUHJvYmVz.

132. Martin, R.M., H. Leonhardt, and M.C. Cardoso, *DNA labeling in living cells.* Cytometry A, 2005. **67**(1): p. 45-52.

133. Qu, X., et al., *Imaging of cancer cells by multiphoton microscopy using gold nanoparticles and fluorescent dyes.* J Biomed Opt, 2008. **13**(3): p. 031217.

134. Hoechst 33342 Protocol for Imaging. 13 september 2021]; Available from: https://www.thermofisher.com/pt/en/home/references/protocols/cell-and-tissue-analysis/protocols/hoechst-33342-imaging-protocol.html.

135. E.Ducat, B.E., O.Peulen, G.Piel, *Cellular uptake of liposomes monitored by confocal microscopy and flow cytometry.* Journal of Drug Delivery Science and Technology, 2011. **21**(6): p. 469-477.

136. Adan, A., et al., *Flow cytometry: basic principles and applications.* Crit Rev Biotechnol, 2017. **37**(2): p. 163-176.

137. Maria Inês Silva, A.I.B., Sofia A. Costa Lima, Paulo Costa, Tiago Torres, Salette Reis, *Freeze-Dried Softisan® 649-Based Lipid Nanoparticles for Enhanced Skin Delivery of Cyclosporine A.* Nanomaterials, 2020.

138. Win, K.Y. and S.S. Feng, *Effects of particle size and surface coating on cellular uptake of polymeric nanoparticles for oral delivery of anticancer drugs.* Biomaterials, 2005. **26**(15): p. 2713-22.

139. Yin, T., et al., *Co-delivery of hydrophobic paclitaxel and hydrophilic AURKA specific siRNA by redox-sensitive micelles for effective treatment of breast cancer*. Biomaterials, 2015. **61**: p. 10-25.

140. Puglia, C., et al., *Lipid nanoparticles for prolonged topical delivery: an in vitro and in vivo investigation*. Int J Pharm, 2008. **357**(1-2): p. 295-304.

141. Kanwar, R., et al., *Green Nanotechnology-Driven Drug Delivery Assemblies*. ACS Omega, 2019. **4**(5): p. 8804-8815.

142. Attia, M.F., et al., *An overview of active and passive targeting strategies to improve the nanocarriers efficiency to tumour sites*. J Pharm Pharmacol, 2019. **71**(8): p. 1185-1198.

143. Huang, D., et al., *Nanodrug Delivery Systems Modulate Tumor Vessels to Increase the Enhanced Permeability and Retention Effect*. J Pers Med, 2021. **11**(2).

144. Singh, R. and J.W. Lillard, Jr., *Nanoparticle-based targeted drug delivery*. Exp Mol Pathol, 2009. **86**(3): p. 215-23.

145. Danaei, M., et al., *Impact of Particle Size and Polydispersity Index on the Clinical Applications of Lipidic Nanocarrier Systems*. Pharmaceutics, 2018. **10**(2).

146. Fatisson, J., et al., *Physicochemical characterization of engineered nanoparticles under physiological conditions: effect of culture media components and particle surface coating*. Colloids Surf B Biointerfaces, 2012. **91**: p. 198-204.

147. Li, Y., et al., *Effects of a non-ionic surfactant (Tween-80) on the mineralization, metabolism and uptake of phenanthrene in wheat-solution-lava microcosm*. Chemosphere, 2001. **45**(1): p. 67-75.

148. Standard, I., *ISO 10993-4: Biological Evaluation of Medical Devices Part 4—Selection of Tests for Interactions with Blood*. 2017, International Organization for Standardization: Geneva, Switzerland.

149. Zhang, H., et al., *The role of positively charged sites in the interaction between model cell membranes and γ-Fe(2)O(3) NPs*. Sci Total Environ, 2019. **673**: p. 414-423.

150. Hou, J., et al., *Nanoparticle tracking analysis versus dynamic light scattering: Case study on the effect of Ca(2+) and alginate on the aggregation of cerium oxide nanoparticles.* J Hazard Mater, 2018. **360**: p. 319-328.

151. Kim, S.W., et al., *Hyaluronated nanoparticles with pH- and enzyme-responsive drug release properties.* Colloids Surf B Biointerfaces, 2014. **116**: p. 359-64.

152. Standardization, I.O.f., *ISO 10993-5:2009 Biological Evaluation of Medical Devices. Part 5: Tests for In Vitro Cytotoxicity.* 2009, International Organization for Standardization: Geneva, Switzerland.

153. Wang, J., et al., *Mitoxantrone-loaded chitosan/hyaluronate polyelectrolyte nanoparticles decorated with amphiphilic PEG derivates for long-circulating effect.* Colloids Surf B Biointerfaces, 2018. **171**: p. 468-477.

154. Behzadi, S., et al., *Cellular uptake of nanoparticles: journey inside the cell.* Chem Soc Rev, 2017. **46**(14): p. 4218-4244.

155. Jaracz, S., et al., *Recent advances in tumor-targeting anticancer drug conjugates.* Bioorg Med Chem, 2005. **13**(17): p. 5043-54.

156. Higa, K., et al., *Hyaluronic acid-CD44 interaction mediates the adhesion of lymphocytes by amniotic membrane stroma.* Cornea, 2005. **24**(2): p. 206-12.

157. Herrera-Gayol, A. and S. Jothy, *Effects of hyaluronan on the invasive properties of human breast cancer cells in vitro.* Int J Exp Pathol, 2001. **82**(3): p. 193-200.

158. Cell Atlas. *CD44. RNA EXPRESSION OVERVIEW.* Available from: https://www.proteinatlas.org/ENSG00000026508-CD44/cell.

159. Zhang, Y., et al., *Real-time imaging tracking of a dual-fluorescent drug delivery system based on doxorubicin-loaded globin- polyethylenimine nanoparticles for visible tumor therapy.* Colloids Surf B Biointerfaces, 2018. **170**: p. 163-171.

160. Li, S., et al., *pH-responsive biocompatible fluorescent polymer nanoparticles based on phenylboronic acid for intracellular imaging and drug delivery.* Nanoscale, 2014. **6**(22): p. 13701-9.